MONTAN UNIVERSITÄT
WWW.UNILEOBEN.AC.AT

Dissertation

Mineralogical, petrological and (isotope-) geochemical studies on the Felbertal scheelite deposit, Austria:

Development of an epigenetic model for W mineralization in the context of Variscan magmatism in the Tauern Window

Mag.rer.nat. Michael Kozlik

Montanuniversität Leoben

Department Angewandte Geowissenschaften und Geophysik

Lehrstuhl für Rohstoffmineralogie

Supervisor: Univ.-Prof. Dr.phil. Johann G. Raith

- September 2015 -

Affidavit:

I declare in lieu of oath, that I wrote this thesis and performed the associated research myself, using only literature cited in this volume.

Leoben, 23th September 2015

Michael Kozlik

“This must be the world's best camouflaged underground mine quietly operating, unnoticed, under the floor of a picturesque, tourists-frequented Alpine valley[1]”

[1]Prof. Dr. Peter Laznicka about Felbertal W-deposit; in Giant Metallic Deposits, Springer Verlag, page 583

Abstract

This thesis addresses the formation of the Felbertal scheelite deposit (Austria) and considers the question whether W mineralization is exclusively related to the intrusion of a highly fractionated granite (K1-K3 orthogneiss) during the Variscan orogeny. The primary focus is on the mineralogical, petrological and (isotope-) geochemical characteristics of the K1-K3 orthogneiss and its pre-metamorphic mineral assemblage. Moreover, barren orthogneisses of the central Tauern Window (Zentralgneise) were included to determine the relationship between the intrusion of the K1-K3 granite and the magmatic activity during Variscan orogeny.

Petrographic and field-based studies revealed two distinct types of K1-K3 orthogneiss, a dark-colored biotite-rich and a light-colored microcline/muscovite-rich variety, respectively. Additionally, leucocratic aplite gneisses occur within the deposit. Whole rock geochemical analyses revealed that various compatible elements (e.g. CaO, FeO, TiO_2, P_2O_5, Ba, Sr) as well as element ratios (Zr/Hf, Nb/Ta) systematically decrease from the dark- to the light-colored K1-K3 orthogneiss variety and to the aplite gneiss. These trends indicate that fractional crystallization was the dominant process that has controlled the evolution of the granitic melts during magmatic differentiation. The new results demonstrate that the K1-K3 orthogneiss represents a metamorphosed series of granitic melts characterized by an increasing degree of magmatic differentiation. This is regarded as a prerequisite for granite-related ore-formation.

In-situ LA-ICP-MS U-Pb and Lu-Hf isotope analyses were performed on zircon from the K1-K3 orthogneiss and two samples from the Zentralgneise (Felbertauern augengneiss, Granatspitz gneiss). The U-Pb concordia ages from the K1-K3 orthogneiss and the aplite gneiss confine the emplacement period of the granitic melts between 341 Ma and 336 Ma. The corresponding apparent εHf_t values range from -7.6 to -4.9 indicating a continental crustal source. The isotopic data of zircon from the Felbertauern augengneiss are similar, yielding a U-Pb concordia age of 338.5 ± 1.3 Ma and apparent εHf_t values between -6.8 and -5.3. Zircons from the Granatspitz gneiss are significantly younger and show apparent εHf_t values between -3.1 and +2.5. The mineralogical and (isotope-) geochemical results suggest that the Felbertauern augengneiss and the dark-colored K1-K3 orthogneiss derived from the same/very similar protolith and preclude any relationship of the K1-K3 orthogneiss with the Granatspitz gneiss. Additionally, trace element concentrations of zircon from the K1-K3 orthogneisses were analyzed by LA-ICP-MS. Evaluation of the data

revealed the occurrence of magmatic and hydrothermal zircon. The latter is enriched in W, U, Nb, Ta, and B compared to magmatic zircon and indicates the presence of a metal- and volatile-rich magmatic-hydrothermal fluid/vapor phase. Besides, the Sr isotope compositions of apatite from the K1-K3 orthogneiss and scheelite from various host lithologies within the deposit were analyzed by in-situ LA-ICP-MS. In the primary scheelite generations (Scheelite 1 and 2) the $^{87}Sr/^{86}Sr$ ratios range from 0.7208 to 0.7642 and from 0.7072 to 0.7683, respectively. Zoned apatite from the K1-K3 orthogneiss revealed $^{87}Sr/^{86}Sr$ of 0.7204-0.7451 for the cores and 0.7454-0.7794 for the rims.

The Lu-Hf isotope data infer that entrainment of pre-existing scheelite into the melt via assimilation of ore-bearing metabasic host rocks during the emplacement of the K1-K3 granite cannot explain the W mineralization associated with the granite. Consequently, a primary magmatic W enrichment of the granitic K1-K3 melt is favored, whereby W and other incompatible trace elements (Nb, Ta, U) were concentrated in the residual melts via fractional crystallization. During the transition from the magmatic to the hydrothermal stage, these elements were transferred from the melt into exsolved hydrothermal fluids, which infiltrated the Early Paleozoic country rocks at Felbertal where they caused incongruent release of ^{87}Sr from Rb-rich minerals (e.g. mica) during fluid-rock interaction and crystallization of scheelite and Nb-Ta minerals in a stockwork of quartz-scheelite veins and mineralized shear zones. $^{87}Sr/^{86}Sr$ ratios of magmatic apatite cores from the K1-K3 orthogneiss are too radiogenic to be magmatic but are comparable to those of Scheelite 1. The Sr isotopic composition of apatite cores was therefore equally modified during the hydrothermal mineralization processes, therefore supporting the single-stage genetic model in which W mineralization is associated with the intrusion of the K1-K3 granite.

Zusammenfassung

Diese Dissertation thematisiert die Entstehung der Scheelit-Lagerstätte Felbertal (Österreich) und geht der Frage nach, inwiefern ein genetischer Zusammenhang zwischen der W Vererzung und der Intrusion eines stark fraktionierten Granits (K1-K3 Orthogneis) während der Variszischen Orogenese besteht. Der Fokus liegt dabei auf den mineralogischen, petrologischen und (isotopen-) geochemischen Besonderheiten des K1-K3 Orthogneises und dessen prä-metamorphen Mineralparagenese. Zudem wurden nicht vererzte Orthogneise des zentralen Tauern Fensters (Zentralgneise) berücksichtigt, um den Zusammenhang zwischen der Intrusion des K1-K3 Granits und der magmatischen Aktivität während der Variszischen Orogenese zu eruieren.

Basierend auf petrographischen und feld-geologischen Beobachtungen konnten ein dunkler, Biotit-reicher und ein heller Muskovit/Mikroklin-reicher K1-K3 Orthogneis Typ unterschieden werden. Zusätzlich treten leukokrate Aplitgneise innerhalb der Lagerstätte auf. Gesamtgesteinschemische Analysen ergaben, dass die Konzentrationen kompatibler Elemente (e.g. CaO, FeO, TiO_2, P_2O_5, Ba, Sr) und Elementverhältnisse (Zr/Hf, Nb/Ta) von dunklem zu hellen K1-K3 Orthogneis und Aplitgneis abnehmen. Dieser Trend zeigt, dass fraktionierte Kristallisation der dominierende Prozess während der Kristallisation der granitischen Schmelzen war. Dies belegt, dass der K1-K3 Orthogneis eine metamorph überprägte Abfolge granitischer Schmelzen darstellt, die durch einen ansteigenden Grad an magmatischer Differentiation charakterisiert sind. Dies wird im Allgemeinen als Grundvoraussetzung für granit-gebundene Lagerstätten gedeutet.

Die Untersuchung des U-Pb und Lu-Hf Isotopensystems an Zirkonen des K1-K3 Orthogneises und von zwei Zentralgneisen (Felbertauern Augengneis und Granatspitzgneis) wurde mittels in-situ LA-ICP-MS durchgeführt. Die U-Pb Konkordiaalter ergaben einen Zeitrahmen von 341 bis 336 Ma für die Intrusion des K1-K3 Granit und der Aplite. Entsprechende εHf_t Werte streuen zwischen -7.6 und -4.9 und weisen auf eine krustale Quelle hin. Die Isotopendaten der Zirkone des Felbertauern Augengneises sind ähnlich und ergaben ein U-Pb Konkordiaalter von 338.5 ± 1.3 Ma und εHf_t Werte zwischen -6.8 und -5.3. Zirkone des Granatspitzgneises sind jünger und weisen εHf_t Werte zwischen -3.1 und +2.5 auf. Die mineralogischen und (isotopen-) geochemischen Resultate bestätigen eine gemeinsame/ähnliche Quelle für dunklen K1-K3 Orthogneis und Felbertauern Augengneis und schließen einen Zusammenhang zwischen K1-K3 Orthogneis und Granatspitzgneis aus. Zusätzlich wurden Spurenelemente in Zirkonen des

K1-K3 Orthogneises mittels LA-ICP-MS analysiert. Die Auswertung der Daten offenbarte magmatische und hydrothermale Zirkone. Letztere sind verglichen mit magmatischen Zirkonen angereichert an W, U, Nb, Ta, und B, was auf das Vorhandensein einer erzführenden magmatischen-hydrothermalen Fluid/Dampf-Phase hinweist. Zusätzlich wurde die Sr Isotopen Zusammensetzung von Apatit aus dem K1-K3 Orthogneis und Scheelit aus unterschiedlichen Lithologien innerhalb der Lagerstätte mittels in-situ LA-ICP-MS untersucht. Die $^{87}Sr/^{86}Sr$ Verhältnisse der primären Scheelit-Generationen (Scheelit 1 und 2) liegen zwischen 0.7208-0.7642, respektive 0.7072-0.7683. Zonierte Apatite des K1-K3 Orthogneises zeigen $^{87}Sr/^{86}Sr$ Verhältnisse von 0.7204-0.7451 für die Kerne und 0.7454-0.7794 für die Ränder.

Die Daten aus der Untersuchung des Lu-Hf Isotopensystems in Zirkon belegen, dass die Aufnahme einer bereits existierenden Scheelitvererzung in die granitische Schmelze durch Assimilation von vererzten metabasischen Rahmengesteinen während der Platznahme des K1-K3 Granits nicht stattgefunden hat. Stattdessen war eine primäre Wolframanreicherung der K1-K3 Schmelze bereits vorhanden, wobei inkompatible Elemente wie W, Nb, Ta und U durch fraktionierte Kristallisation in den granitischen Restschmelzen konzentriert wurden. Am Übergang vom magmatischen zum hydrothermalen Stadium sind diese Elemente in die Fluide übergegangen, welche anschließend durch das Früh-Paläozoische Rahmengestein zirkulierten. Dies hatte die inkongruente Freisetzung von ^{87}Sr aus Rb-reichen Mineralen (e.g. Glimmer) und Kristallisation von Scheelit und Nb-Ta Mineralen in einem Stockwerk aus Quarz-Scheelit Gängen und vererzten Scherzonen zur Folge. Die $^{87}Sr/^{86}Sr$ Verhältnisse von Apatikernen des K1-K3 Orthogneises sind zu radiogen um als magmatisch zu gelten. Daher ist davon auszugehen, dass die Sr Isotopie der magmatischen Apatitkerne während der hydrothermalen Vererzung modifiziert wurde. Diese Erkenntnisse unterstützen das Genesemodell in dem die Scheelitvererzung in der Lagerstätte Felbertal mit der Intrusion des K1-K3 Granits assoziiert ist.

Danksagungen

Nach knapp über 3 Jahren der Forscherei ist nun endlich der Tag gekommen, an dem ich meine Dissertation mit dem Niederschreiben dieses Kapitels abgeschlossen habe. Nun ist es an der Zeit mich bei all den Personen zu bedanken, die zum Gelingen dieser Arbeit beigetragen haben.

Zu größtem Danke verpflichtet bin ich Univ.-Prof. Dr. phil. Johann G. Raith der stets ein offenes Ohr für all meine Fragen hatte, von dessen wegweisenden Ratschläge ich so sehr profitierte und der mich auf unbeschreiblich unkomplizierte Weise in meiner wissenschaftlichen Ausbildung stets unterstützte. „*Johann, herzlichen Dank für alles was du für mich in den letzten 3 Jahren getan hast.“*

Ein besonderes Dankeschön soll hiermit an Judith Bergthaler ausgesprochen werden. Ohne ihre beharrliche Geduld und Genauigkeit wäre mein Leben viel schwerer gewesen!

Weitere Institutskollegen denen ich großen Dank schulde sind Dr. Federica Zaccharini und Helmut Mühlhans für deren außerordentliche Betreuung an der Mikrosonde. Ao.Univ.-Prof. Dr. phil.Oscar Thalhammer sei gedankt für Probenmaterial und Ao.Univ.-Prof. Dr. Ronald Bakker für sein aufheiterndes Naturell. Bei meinen langjährigen Bürokollegen Peter, Geri und Elisabeth bedanke ich mich für ihre Aufnahme in den Kreis der Doktoranden. Seither war ich einer von ihnen…

Von Seiten der WBH möchte ich mich besonders bei Marie-Luise Pecher für ihren unermüdlichen Einsatz, ihre Neugier und für zweieinhalb Jahre professioneller Zusammenarbeit bedanken. Zudem bin ich Steffen Schmidt, Alexander Mosser und Karsten Aupers zu Dank verpflichtet.

An dieser Stelle soll unbedingt erwähnt werden, dass diese Dissertation ohne die hervorragende Arbeit von Dr. Axel Gerdes (Goethe Universität Frankfurt) nicht gelungen wäre. Gleichzeitig schulde ich Linda Marko für ihre wunderbare Betreuung und ihre unerreichbare Präparationsarbeit einen Strauß bunter Blumen. Auch Jeanne Taylor sei gedankt für moralische Unterstützung, einen wundervollen Tag in Innsbruck und vier unvergessliche Tage in Stellenbosch.

Ein ganz besonderes Dankeschön richtet sich an Ao.Univ.Prof. Dr. Fritz Finger (Universität Salzburg) für dass er stets seine kostbare Zeit und sein schier unendliches Wissen über Granitpetrologie mit mir teilte.

Des Weiteren danke ich Stefan Neumeister und Ass.Prof. Dr. phil. Reinhard Gratzer für die Zurverfügungstellung der Achatschwungscheibenmühle. Natalie Auer möchte ich

danken, dass ich Backenbrecher und diverser Siebe zur Probenaufbereitung benutzen durfte. Auch Ass.Prof. Dipl.-Ing. Dr.mont. Nina Gegenhuber möchte ich herzlich danken, da sie mir spontan und unkompliziert das tragbare Gammaspektrometer zur Verfügung gestellt und mir weitere Proben unter Laborbedingungen gemessen hat.

Ein großer Dank geht natürlich auch an meine zwei besten Freunde in Leoben, mit denen ich viele heitere und unvergessliche Stunden und Tage erleben durften und die natürlich nicht unerwähnt bleiben dürfen: Heinz Binder und Phil (nein, nicht „The Power“ Taylor) Sedlazeck.

Allerdings wäre ich nie so weit gekommen ohne die in jeglicher Hinsicht immerwährende Unterstützung durch Mama, Papa, Christoph, Sonja und auch der kleinen Isabell. Meine Dankbarkeit euch gegenüber kennt kein Grenzen!

Table of contents

Units and abbreviations

apfu	atoms per formula unit
ppm	parts per million
ppb	parts per billion
V	volt
kV	kilovolt
MeV	megaelectron volt
nA	nanoampere
A	ampere
Hz	hertz
J	joule
s	second
nm	nanometer
µm	micrometer
mm	millimeter
cm	centimeter
l min^{-1}	litre per minute
g	grams
t	tons
vol	volume
dark-col.	dark-colored
light.-col.	light-colored
cf.	*conferre* (compare)
e.g.	*exempli gratia* (for example)
i.e.	*id est* (that is)
eq.	equation
REE	rare earth elements
LREE	light rare earth elements
MREE	middle rare earth elements
HREE	heavy rare earth elements
HFSE	high field strength elements
MUL	Montanuniversität Leoben
WBH	Wolfram Bergbau und Hütten AG
JWG	Johann Wolfgang von Goethe University Frankfurt
n	number/quantity
nd	not detected
bdl	below detection limit
audl	above upper detection limit
LOI	loss on ignition
BSE	back scattered electron
CL	cathodoluminescence
UV	ultra violet
WDS	wavelength-dispersive system
XRF	X-ray fluorescence spectroscopy
EPMA	electron probe microanalyzer
SEM	scanning electron microscope
LA-SF-ICP-MS	laser ablation – sector field – inductively coupled plasma – mass spectrometry
LA-MC-ICP-MS	laser ablation – multicollector – inductively coupled plasma – mass spectrometry

Qz	Quartz
Kfs	Potassium feldspar
Pl	Plagioclase
Ab	Albite
An	Anorthite
Or	Orthoclase
Bt	Biotite
Chl	Chlorite
Ms	Muscovite
Ann	Annite
Eas	Eastonite
Phl	Phlogopite
Sid	Siderophyllite
Cpx	Clinopyroxene
Opx	Orthopyroxene
Aln	Allanite
Czo	Clinozoisite
Ep	Epidote
Zo	Zoisite
Ap	Apatite
Brl	Beryl
Cc	Calcite
Grt	Garnet
Pcl	Pyrochlore
Po	Pyrrhotite
Thr	Thorite
Ttn	Titanite
Zrn	Zircon
Ilm	Ilmenite

1 Introduction

The Felbertal scheelite deposit, located 8 km south of Mittersill in the province Salzburg (Austria), is a major tungsten producer in the world. In 2014 the mine produced 1072 t WO_3, making Felbertal to a globally important supplier of tungsten (bmwfw 2014; U.S. Geological Survey 2015). After its discovery in 1967 by R. Höll and a group of students from the University of Munich it was classified as the type locality for strata-bound syngenetic exhalative-sedimentary W-deposits related to Early Paleozoic mafic submarine volcanism and it was the object of numerous scientific studies since then (Eichhorn et al. 1995, 1997, 1999; Finger et al. 1985; Höll 1969, 1971, 1975, 1979; Höll and Schenk 1988; Höll and Eichhorn 2000; Höll et al. 1987; Jahoda 1984; Raith and Stein 2006; Raith and Schmidt 2010; Raith et al. 2011; Schenk 1990; Schenk and Höll 1989; Schmidt 1988, 2012; Thalhammer et al. 1989; Topa et al. 2002; von Quadt 1985).

From this multitude of publications and thesis diverse opinions evolved addressing the genetic evolution of the W mineralization at Felbertal. Different analytical and theoretical approaches were considered to solve the puzzling scientific problem that the Felbertal scheelite deposit represents. The polymetamorphic overprint during the Variscan and Alpine orogeny further complicates the geological situation; i.e., it resulted in the dissemination of scheelite throughout various lithologies and modifying the chemical characteristics of primary W mineralization. Additionally, the pervasive and ubiquitous occurrence of scheelite and the subsequent tectonic overprint that affected the scheelite deposit obliterates any decisive association of the tungsten ores with a certain lithology or geological process.

Nowadays, the W-deposit is mostly interpreted as a metamorphosed stock-work to vein-type scheelite deposit (Schmidt 2012) and its association with metagranitic rocks is widely accepted (Eichhorn et al. 1999; Raith and Stein 2006); although one question still awaits a final answer: when and under which geological conditions did scheelite form? It is still debated whether mineralization is two-phase and dichronic (Cambrian and Early Carboniferous; Eichhorn et al. 1999) or exclusively of Variscan age. In most models the K1-K3 orthogneiss, a W mineralized Variscan meta-granite in the deposit, is assigned a key role for deciphering the genesis of this deposit. It is either regarded as the ore-forming granite that caused the whole W mineralization (Briegleb, 1987, 1991; Pestal 1983; Raith and Stein 2006) or as a later intrusion mobilizing pre-existing scheelite mineralization (e.g. via assimilation; Höll and Eichhorn 2000).

This PhD thesis is the result of a project funded by the Austrian Research Promotion Agency (FFG Bridge project 834149/30661) and Wolfram Bergbau und Hütten AG. The underlying hypothesis of the study claimed that there is a spatial, temporal and genetic relationship between the intrusion of the Early Carboniferous K1-K3 granite and the development of the W-deposit at Felbertal. The research focused on the whole-rock geochemical, mineralogical and isotope-geochemical characteristics of metagranitoids from the Felbertal scheelite deposit and of adjacent barren orthogneisses from the central Tauern Window (Zentralgneise). Therefore, a multi-analytical approach was considered, including whole-rock ICP-MS analyses and gamma-ray spectrometric analysis of different rocks, as well as in-situ mineral- and isotope chemical analyses of various minerals by electron microprobe and LA-ICP-MS.

The objectives were to characterize the source and magmatic evolution of the granitic melts forming the K1-K3 orthogneiss and to elaborate the similarities and differences between the K1-K3 orthogneiss and the Zentralgneise with respect to source, age and petrogenetic evolution of the metagranitoids. This should contribute to answer the question, if the relatively small magmatic K1-K3 intrusion is related to a larger granitic system and if so, what relations can be established with any of the studied Zentralgneise. The core issue was to decipher the genetic relation of the Early Carboniferous K1-K3 orthogneiss and the scheelite mineralization at Felbertal. If the link between the K1-K3 orthogneiss and the mineralization at Felbertal is valid, appropriate proximity indicators should be developed for exploration of K1-K3 orthogneiss equivalents in the Tauern Window.

The results are discussed in the context of granite-related ore formation and metamorphic processes and provide new insights into the genetic position of the W mineralized K1-K3 orthogneiss in the context of magmatism during the Variscan orogeny in the Tauern Window. The new data contribute to our understanding of the petrogenetic evolution of this unusual W-deposit and constrain the origin of hydrothermal fluids precipitating scheelite in the Felbertal area.

2 Geological setting and tungsten mineralization

2.1 Regional geological overview

Within the Eastern Alps, three tectonic windows occur that give insight into the deepest tectonic units of the Alpine orogen. These windows are the result of N-S shortening of the Eastern Alps, Late Alpine extensional tectonics and post Alpine exhumation. The Tauern Window represents the largest of these windows, uncovering European basement crystalline rocks and their locally retained (para)autochthonous Late Paleozoic-Mesozoic sedimentary cover. It extends over a length of 160 km in W-E direction and is confined by the Brenner Fault in the west and the Katschberg Fault in the east (cf. Pestal et al. 2009). These two normal faults represent large shear zones which formed due to the N-S compression of the Tauern Window and the lateral extrusion of the Eastern Alps during the Miocene (cf. Schmid et al. 2013 and references therein). Two strike-slip fault zones, namely the Salzach-Ennstal-Mariazell-Puchberg Fault and the Mölltal Fault, represent the northern and southeastern termination of the Tauern Window, respectively.

According to Schmid et al. (2013) the major tectonic units of the Tauern Window are the Subpenninic nappes of the Venediger Duplex (e.g. Zillertal-Riffl Nappe, Tux-Granatspitz Nappe), the Subpenninic nappes in the hanging wall of the Venediger Duplex (e.g. Eclogite Zone, Glimmerschieferlamelle) and the Penninic ophiolite-bearing units (e.g. Glockner Nappe system). The following geological description mainly focuses on the central parts of the Tauern Window.

Generally, the Venediger Duplex comprises a folded stack of nappes deformed to a duplex structure with tectonic boundaries at its foot- and hanging wall (Frisch 1977; Lammerer and Weger 1998). The Subpenninic units were derived from the distal European continental margin and correspond to the (pre-) Variscan basement and their post-Variscan cover sequences (“Untere Schieferhülle”). The late Precambrian to Ordovician crystalline basement was intruded during the Variscan orogeny by Early Carboniferous to Early Permian granitoids. Regional metamorphism and deformation transformed these granitoids into various orthogneisses (Zentralgneise). The part of the pre-Mesozoic metamorphic basement with intrusive contacts to the Zentralgneise is conforming to the established term “Altes Dach”, whereas pre-Carboniferous basement in general has been referred to as “Altkristallin” (Frasl 1958; Pestal et al. 2009; Schmid et al. 2013). Within the nappe stack of the Venediger Duplex, the Tux-Granatspitz Nappe overlies the Ahorn Nappe of the western Tauern Window; the Zillertal-Riffl Nappe

occupies the highest structural position in the Venediger Duplex (Fig. 2.1). The latter represents a large pre-Variscan basement complex in the central Tauern Window known also as Old Gneiss Series (“Serie der Alten Gneise”; Frasl and Frank 1966). The period of time when the Zillertal-Riffl Nappe had overthrusted the Tux-Granatspitz Nappe is still in the focus of discussion. In contrast to Frisch (1980), who argued for a Variscan tectonic event, Schmid et al. (2013) suspected an association with the Late Alpine orogeny.

The post-Variscan (?) cover sequences mainly comprise meta-sedimentary units, for which radiometric data either are missing (Murtörl Formation) or a Variscan age has been suggested (Basal Schist). For the latter, radiometric U-Pb dating of zircons constrained the maximum time of sedimentation between 362 ± 6 Ma and 368 ± 17 Ma (Kebede et al. 2005), by what these authors interpreted the metasediments to represent a flysch sequence deposited during the Variscan orogeny. Conversely, Schmid et al. (2013) argued that zircons from the Basal Schist (“Biotitporphyroblastenschiefer”) yielded older U-Pb ages (362 ± 6 Ma) than those from the concordantly (?) underlying Basal Amphibolite (“Basisamphibolit”; 351-343 Ma; Kebede et al. 2005). Consequently, zircons from the Basal Schist might be detrital in origin and the Basal Schist could well be post-Variscan (Fig. 2.1).

The Subpenninic nappes overlying the Venediger Duplex comprise Mesozoic meta-sediments (e.g. Wustkogel Formation) and high-grade metamorphic felsic and carbonatic rocks with intercalations of metabasites (Eclogite Zone, Fig. 2.1). The latter represents a volcano-sedimentary sequence that was part of the distal European continental margin (Miller et al. 1980; Schmid et al. 2004). The structural highest parts of the Subpenninic nappes are composed of quartz-rich micaschists (Glimmerschieferlamelle) associated with Triassic and Cretaceous metasediments that form the boundary between the Eclogite Zone and the tectonically overlying Glockner Nappe system (Spear and Franz 1986).

The Penninic ophiolite-bearing units, including the voluminous Glockner Nappe system (Fig. 2.1), are interpreted to be derived from the Valais Ocean (Schmid et al. 2004; 2013). The Glockner Nappe system comprises a nappe pile with siliciclastic and calcareous meta-sediments and intercalated amphibolites and serpentinites. Remnants of the Piemont-Ligurian Ocean are present in the Reckner ophiolitic complex and in the Matrei Zone which were accreted to the Austroalpine nappe stack during the subduction of the Piemont-Ligurian Ocean in the Turonian (Schmid et al. 2013).

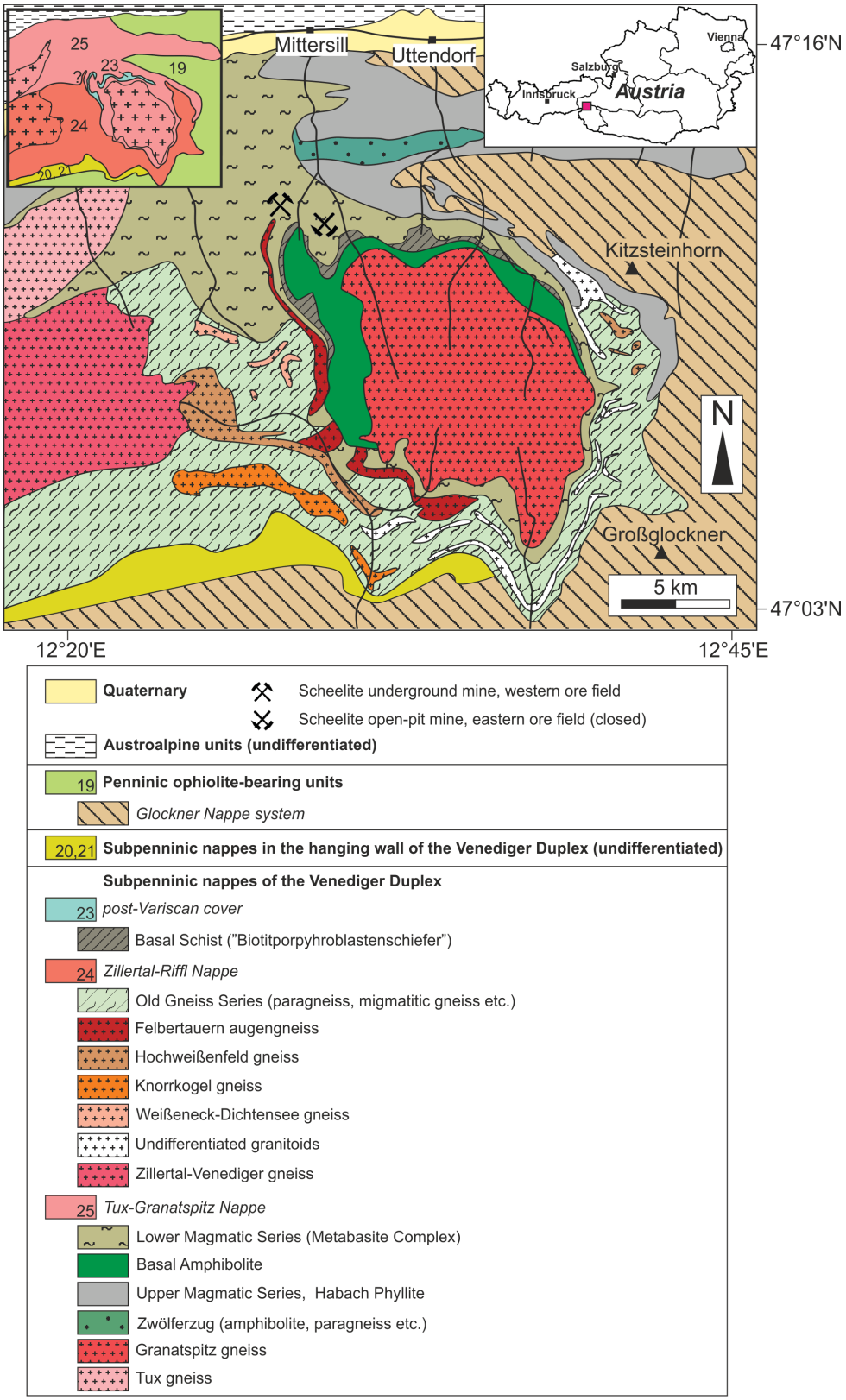

Fig. 2.1 Generalized geological map of the central Tauern Window showing the location of the Felbertal scheelite deposit (modified from Finger et al. 1993; Frisch 1980; Kurz et al. 2008; Pestal et al. 2009; Schmid et al. 2013). The numbering of the tectonic nappes in the upper left sketch and in the legend is consistent with figure 1 of Schmid et al. (2013).

The Felbertal scheelite deposit is located within the central parts of the Tauern Window where Zentralgneise and Early to Late Paleozoic basement rocks, assigned to the Habach Complex sensu Frasl (1958) dominate the geology. In general, the Habach Complex represents a polymetamorphic succession of basic to ultrabasic plutonic and volcano-sedimentary rocks with intercalations of felsic lithologies that constitute the pre-Variscan basement of the central Tauern Window (Höck 1993). The Habach Complex is part of the Tux-Granatspitz Nappe (Schmid et al. 2013). However, according to Frank et al. (1987) the Habach Complex belongs to the Zillertal-Riffl Nappe ("Hülle des Zillertaler Kerns, Riffldecke").

A purely spatial subdivision of the Habach Complex from bottom to top includes the Lower Magmatic Series (LMS), the Upper Magmatic Series (UMS) and the Habach Phyllite (Eichhorn et al. 2000, 2001; Höck 1993; Kebede et al. 2005; Söllner et al. 1991; Vavra and Hansen 1991; von Quadt 1992). According to the classification of Pestal et al. (2009), however, only the UMS and the Habach Phyllite constitute the Habach Complex ("Habach-Gruppe"), despite their different formation ages: An Early Carboniferous to Early Permian formation age is suggested for different metamorphosed calc-alkaline volcanic rocks of the UMS (Eichhorn et al. 2000; Söllner et al. 1991; Vavra and Hansen 1991), whereas Kebede et al. (2005) proposed a Late Cambrian maximum sedimentation age for a volcano-clastic agglomerate in the Habach Phyllite (see below). The LMS corresponds to the Early Paleozoic Metabasite Complex in the central Tauern Window (Pestal et al. 2009).

The Felbertal W-deposit is located in the LMS, which is interpreted as the (sub-) volcanic part of an ophiolite (Höck 1993). The LMS mainly comprises fine- to coarse grained amphibolites, hornblendites, various gneisses, schists, and quartz-rich rocks. Eichhorn et al. (1999) reported a Neo-Proterozoic / Early Cambrian U-Pb SHRIMP age of 547 ± 27 Ma for zircons from the fine-grained amphibolites. Zircons from the coarse-grained amphibolites (meta-gabbros) record an age of 482 ± 5 Ma (Eichhorn et al. 2001) and conventional U-Pb dating of zircons from the hornblendites (meta-cumulates?) yielded a crystallization age of 496 ± 2 Ma (von Quadt 1992). Volcanic arc-related calc-alkaline I-type granitoids were emplaced during the Early Cambrian (Höll and Eichhorn 2000). The Early Cambrian age of these orthogneisses is confirmed by U-Pb SHRIMP dating of zircons from the "EOZ gneiss" (orthogneiss underlying the scheelite-rich ores in the Eastern Ore Zone), yielding a magmatic formation age of 529 ± 17 Ma (Eichhorn et al. 1999).

The UMS constitutes a part of the Variscan basement and represents a succession of various Late Carboniferous to Early Permian calc-alkaline basic to acidic meta-volcanics comprising biotite-rich amphibolites, chlorite-albite schists or muscovite-albite gneisses (Eichhorn 2000; Höck et al. 1993; Söllner et al. 1991; Vavra and Hansen 1991). The protoliths of these rocks are interpreted as tuffs and volcano-clastic sediments formed probably in an island arc or near a continental margin (cf. Pestal et al. 2009).

The uppermost tectonic unit within the Habach Complex is the Habach Phyllite, a sequence of dark phyllites, micaschists, and mafic to felsic meta-volcanics that were deposited in a volcanic arc environment (Eichhorn et al. 1999). Zircons from gabbro clasts in a metamorphosed volcano-clastic agglomerate in the Habach Phyllite yield an upper intercept age of 536 ± 8 Ma, suggesting an Early Cambrian protolith age (Kebede et al. 2005). A nearly concordant age of 506 ± 9 Ma obtained from a rounded detrital zircon generation from the same rock is interpreted as the maximum sedimentation age of the Habach Phyllite (Kebede et al. 2005).

Early Carboniferous to Early Permian granitoids intruded the Cambro-Ordovician basement sequence as a consequence of the accretion of peri-Gondwana terranes and the subsequent collision of Gondwana with Laurasia (Stampfli and Borel 2002). These metagranitoids occur in the central part of the Tauern Window either as large voluminous plutons forming dome-like structures (e.g. Granatspitz gneiss) or as elongated sill-like bodies (e.g. Felbertauern augengneiss; Fig. 2.1). Eichhorn et al. (2000) distinguished four distinct pulses of granitoid melt generation in the central Tauern Window in the Middle Devonian, Early Carboniferous, Late Carboniferous, and Early Permian, respectively. Magmatism is linked to an evolving Variscan collisional belt starting with an active plate margin setting in the Middle Devonian, generating subduction-related, volcanic arc granites (e.g. Zwölferkogel gneiss: 374 ± 10 Ma, Eichhorn et al. 2000). During the Early Carboniferous, collisional I-type granites and anatexites were produced in a transpressional tectonic regime as the result of the amalgamation of Gondwana and Laurasia (e.g. Felbertauern augengneiss: 340 ± 4 Ma, Eichhorn et al. 2000). After a period of exhumation and erosion, a third pulse of granitoid magmatism in the Late Carboniferous generated late-Variscan calc-alkaline I-type melts (e.g. Peitingalm gneiss: 300 ± 5 Ma, Eichhorn et al. 2000). The subsequent change to an extensional tectonic setting caused post-Variscan granitoid formation during the Early Permian, with the intrusion of a large S-type batholith (Granatspitz gneiss: 271 ± 4 Ma, Eichhorn et al.

2000). However, the age of this batholith is debated; Kebede et al. (2005) postulated an emplacement age of 314 ± 1 Ma for this metagranitoid.

The small elongated Zentralgneise bodies of the central Tauern Window (e.g. Felbertauern augengneiss, Knorrkogel gneiss, Hochweißenfeld gneiss; Fig. 2.1) are part of the Zillertal-Riffl Nappe (Fuchs 1958). Accordingly, the lamella of the Felbertauern augengneiss occupies the lowermost parts of the Zillertal-Riffl Nappe. However, an association with the Tux-Granatspitz Nappe was also proposed for this strongly deformed augengneiss (Frasl and Frank 1966).

The central Tauern Window was affected by Alpine regional metamorphism reaching lower amphibolite facies conditions (500-590 °C, 4.5-7.0 kbar) during the Late Eocene/Oligocene in its center (see Grundmann 1989; Höll and Eichhorn 2000 and references therein). The Late Alpine metamorphism has been regarded as the predominant regional metamorphic event in the Tauern Window, although the question of the extent of a pre-Alpine metamorphic overprint in the Felbertal area is still awaiting a final answer. Eichhorn et al. (1995) argued that in the Felbertal W-deposit Variscan metamorphism was higher grade (T_{max} = 590 °C) than the Alpine upper greenschist- to amphibolite-facies metamorphic event (T_{max} = 520 °C). Accordingly, the dominant fabrics at the Felbertal scheelite deposit are regarded as Variscan, although the stacking of the distinct tectonic slices is attributed to Alpine compressional tectonics (Höll and Eichhorn 2000). Other support for a Variscan age of metamorphism comes from Re-Os molybdenite ages from the Felbertal W-deposit, ranging between 358 and 336 Ma (Raith and Stein 2006) and a rather imprecise Sm-Nd age of metamorphic Scheelite 3 yielding 319 ± 34 Ma (Eichhorn et al. 1997). On the contrary, Koller and Richter (1984) reported lower Variscan (?) *P-T* conditions of 420 °C and 2 kbar for the Habach Complex. Recent U-Pb apatite ages confirm the Late Alpine exhumation of the central Tauern Window (~31-29 Ma; Schneider et al. 2015). At Felbertal the Late Alpine metamorphic overprint is recorded by a Sm-Nd isochron age of Scheelite 4 yielding 29 ± 17 Ma (Eichhorn et al. 1997).

2.2 Felbertal scheelite deposit

2.2.1 Geological description

An eastern (open pit) and a western (underground) ore field, which are slightly displaced relative to each other probably as the result of an Alpine dextral, west-dipping, thrust-slip

fault, are distinguished in the Felbertal area (Höll and Eichhorn 2000). Today, active mining is limited to the western ore field. In the eastern ore field mining was concentrated on post-glacially disrupted ore masses (scree) and an in-situ quartz-scheelite ore body (Höll and Eichhorn 2000). The main ore was a laminated scheelite-quartz ore ("Scheelitreicherz") with an average grade of 2 mass% WO_3. These quartz-scheelite masses were spatially associated with the underlying leucocratic EOZ gneiss lens ("Ostfeldgneis") featuring an intense network of quartz veins. This stock-work zone was interpreted as the feeder system for the over-lying high-grade ores (Höll and Eichhorn 2000).

In the western ore field three major tectonic wedges can be distinguished: a barren segment of Basal Schist ("Basisschieferschuppe") separates two scheelite-bearing wedges into a hanging wall and footwall that include hornblende schist units (Schmidt 1988; Raith and Schmidt 2010). The mineralization occurs generally as quartz vein stockwork (or sheeted quartz veins) throughout the different lithologies, and economic grades are found commonly, where the quartz-veining is more intense. Additionally, shear zones with scheelite-quartz mylonites and quartz-masses atop the K1-K3 metagranitoid contained high grade W mineralization. The mineral assemblage of the veins includes quartz, scheelite and minor to accessory muscovite, epidote, clinozoisite, zoisite, calcite, fluorite, phenakite, beryl, titanite, Nb-Ta-minerals, molybdenite, pyrite, pyrrhotite, and chalcopyrite. Moreover, a variety of rare Pb-Bi-sulfosalts occurs within the quartz veins (Topa et al. 2002 and references therein).

The Early Paleozoic sequence was intruded by a highly differentiated leucocratic granitoid during the Carboniferous (U-Pb zircon concordia age of 336 ± 19 Ma, Eichhorn et al. 1995; Rb-Sr age of 316 ± 10 Ma, Pestal 1983). This orthogneiss is mainly exposed underground in the western ore field where it was spatially linked to (now mined) high-grade mineralization (parts of the K1 and K3 ore bodies). A striking feature of the K1-K3 orthogneiss are the high concentrations of the trace elements Nb, Ta, Be, Rb, U, Mo, Bi, F, and W. The orthogneiss can be classified as a felsic metaluminous to weakly peraluminous high K calc-alkaline I-type syeno- monzogranite mainly composed of quartz, albite, potassium feldspar and varying amounts of biotite and phengitic muscovite (Finger et al. 1985; Höll and Eichhorn 2000). Primary magmatic accessory minerals are zircon, apatite and relicts of titanite and allanite; the latter is commonly surrounded by a metamorphic clinozoisite-epidote corona.

Additional leucocratic orthogneisses occur associated with the K2 orebody; however they belong to the Early Paleozoic I-type granites of the western ore field according to Höll and Eichhorn (2000). The K2 orebody was discovered on the upper levels (1110-1175 m) in the underground mine associated with biotite-albite gneisses, quartz-albite-biotite schists and quartz-rich rocks (Schenk and Höll 1989). The economically recoverable scheelite mineralization in the original K2 area was predominantly linked to the quartz masses containing minor plagioclase, mica, carbonate, fluorite and additionally pyrrhotite, chalcopyrite, pyrite, molybdenite, and Pb-Bi sulfosalts (Schenk and Höll 1989; Schenk 1990; Höll and Eichhorn 2000). On the 1124 m and 1110 m levels, a metamorphosed breccia overlying this bowl-shaped quartz masses was exposed. The breccia is composed of scheelite-bearing quartz- and barren gneiss- plus amphibolite-clasts within a fine-grained metamorphic matrix consisting of fluorite-rich biotite-albite gneisses with disseminated scheelite (Höll and Schenk 1988; Höll and Eichhorn 2000). Eichhorn et al. (1999) reported WO_3 grades of up to 1.65 mass% from the metamorphic K2 groundmass. The gneiss clasts can be linked to the Early Paleozoic leucocratic *older* K2 orthogneiss (U-Pb SHRIMP zircon discordant pooled minimum crystallization age of 529 ± 18 Ma; Eichhorn et al. 1999). The sequence older K2 gneiss – K2 quartz mass – K2 breccia has been locally crosscut by dikes of a leucocratic scheelite-bearing meta-granitoid termed *younger* K2 orthogneiss (U-Pb SHRIMP zircon concordia age of 519 ± 14 Ma; Eichhorn et al. 1999).

2.2.2 Scheelite generations

Based on optical, petrographic, geochemical, and geochronological criteria, the following scheelite generations are distinguished at Felbertal (Höll 1975; Schenk 1990; Eichhorn et al. 1997):

Scheelite 1 is very fine-grained (<0.4 mm), colorless though yellowish-white fluorescent in short-waved UV light. A remarkable feature is the fine-scale oscillatory growth zoning revealed in cathodoluminescence (CL) images (Fig. 2.2a). Its Mo-content is ~1.0 mass% on average and it has been the most prominent generation in the eastern ore field of the Felbertal scheelite deposit where it occurred in mylonitic (?) laminated scheelite-quartz ores. Eichhorn et al. (1999) had postulated a Cambrian formation age for this scheelite generation linked to these pre-Variscan orthogneisses (520-530 Ma), but recent in-situ U-Pb dating of Scheelite 1 by LA-SF-ICP-MS yielded a concordia age of 335.5 ± 4.6 Ma (Raith et al. 2011).

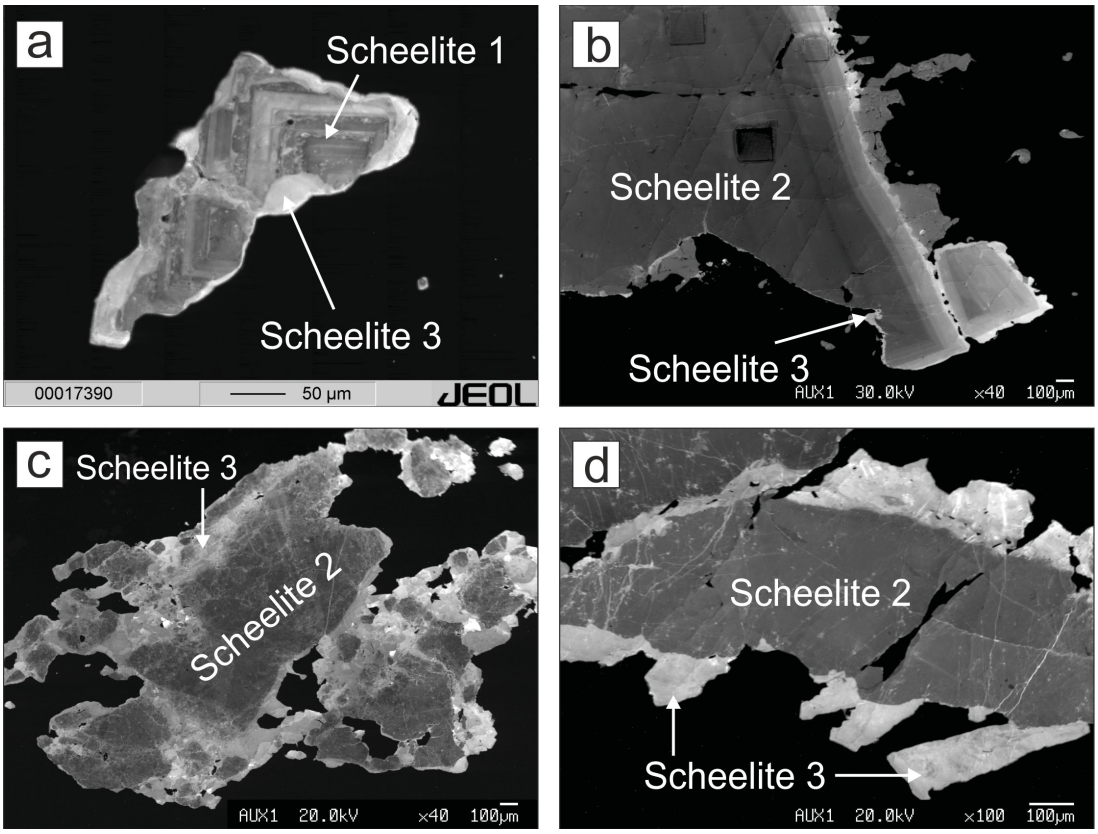

Fig. 2.2 Cathodoluminescence (CL) images of scheelite generations 1-3 at Felbertal. **a)** Scheelite 1 with fine oscillatory zoning is overgrown and partly replaced by CL-brighter metamorphic Scheelite 3; eastern ore field, laminated scheelite-quartz ore (from Raith and Schmidt 2010). **b)** Large (4 mm) Scheelite 2 crystal with growth zoning overgrown by a minute rim of Scheelite 3; western ore field, level 1038 m, quartz-diorite gneiss, sample Gn-1038a. **c-d)** Scheelite 2 replaced / overgrown by Scheelite 3 in a quartz-scheelite vein; western ore field level 1164 m, sample B-K1q-A.

Scheelite 2 is the common generation in the western ore field and is easily identified by its variable but usually large grain size ranging from mm- to cm-scale and its grey color. It displays yellowish fluorescence in UV light and Mo-contents are similar to Scheelite 1 (Eichhorn et al. 1997). Large Scheelite 2 crystals occasionally show a weakly developed growth zoning that is visible only in CL images (Fig. 2.2b). The occurrence of micro-fractures in Scheelite 2 filled with Scheelite 3 is indicative of recrystallization under transitional brittle-ductile deformation; in high-strain zones Scheelite 2 commonly forms porphyroclasts intergrown with recrystallized Scheelite 3 of metamorphic origin. Quartz-scheelite veins featuring the second generation frequently crosscut the K1-K3 orthogneiss, thus an Early Carboniferous maximum crystallization age is assured.

Scheelite 3 formed via recrystallization of Scheelite 1 and 2 (Fig 2.2c) or crystallized as rims around the older scheelite (Fig. 2.2d); it also occurs in micro-fractures within these earlier generations. A bluish fluorescence color in short-waved UV light, very low Mo-

contents (~100 ppm Mo) and bright luminescence in CL (Fig. 2a-d) are characteristic for Scheelite 3. Diffuse zoning can be observed in some grains in CL. Eichhorn et al. (1997) calculated a Sm-Nd isochron age for Scheelite 3 of 319 ± 34 Ma which they interpreted as the time of formation of metamorphic scheelite during Variscan regional metamorphism.

Scheelite 4 displays white to pale-blue fluorescence, is free of Mo and forms up to several cm sized isolated porphyroblasts within Alpine metamorphic quartz veins that occasionally crosscut older Variscan structures including the first generation of quartz-scheelite veins. Occasionally, Scheelite 4 is found disseminated in zones of intense deformation in the host rock itself. A Sm-Nd isochron age of 29 ± 17 Ma corroborates the Alpine age of Scheelite 4 and reflects local remobilization of Variscan scheelite generations during Late Alpine regional metamorphism (Eichhorn et al. 1997).

2.2.3 Contrasting genetic models for tungsten mineralization

The Felbertal scheelite deposit was initially interpreted as the type locality for strata-bound syngenetic exhalative-sedimentary scheelite deposits related to Early Paleozoic mafic submarine volcanism (e.g. Höll 1975, 1977). The lamination of the quartz-rich scheelite ores from the eastern ore field was inferred to be a primary sedimentary texture in cherts of exhalative origin related to volcanic activity. The meta-breccia and associated quartz masses in the western ore field were explained as (sub-) volcanic eruptive explosion-breccias and siliceous exhalites, similar to those found in recent geothermal fields in New Zealand (Höll and Schenk 1988).

Today, a granite-related origin of the Felbertal scheelite deposit (with subsequent metamorphic overprint) is favored, although there is still a debate regarding the exact timing and possible poly-phase nature of W mineralization.

Scheelite of exclusive Variscan age genetically linked to the K1-K3 orthogneiss has been proposed by several authors (Briegleb 1987, 1991; Pestal 1983; Raith and Stein 2006). According to this single-phase granitic model, highly fractionated granitic melts intruded the Early Paleozoic basement during the Variscan orogeny and exsolved W-rich fluids during the magmatic-hydrothermal transition stage. These fluids pervasively penetrated the surrounding metabasic host rocks forming scheelite in veins and stock-works, quartz masses, and shear zones. The subsequent Variscan and Alpine metamorphic overprints only caused local remobilization and dispersion of scheelite at Felbertal. Recently, in-situ U-Pb dating of the scheelite from the laminated scheelite ore in

the eastern ore field (Scheelite 1) by LA-SF-ICP-MS yielded a concordia age of 335.5 ± 4.6 Ma (Raith et al. 2011) similar to the Early Carboniferous K1-K3 orthogneiss.

In contrast, Eichhorn et al. (1999) and Höll and Eichhorn (2000) argued for an epigenetic model with two stages of granite-related scheelite mineralization, the first of Cambrian (~520 Ma) and the second of Lower Carboniferous (~340 Ma) age. The first stage scheelite mineralization (Scheelite 1) was related to the intrusion of Early Paleozoic I-type granites in both ore fields. In the eastern ore field scheelite deposition has been linked to the EOZ orthogneiss ("Ostfeldgneis") dated at 529 ± 17 Ma underlying the quartz-rich scheelite ores (Eichhorn et al. 1999). The fine-grained laminated quartz-rich scheelite ores were re-interpreted as magmatic-hydrothermal cavity-fillings, with scheelite and quartz having been precipitated from W-rich vapors under high fluid pressure conditions (Höll and Eichhorn 2000). In the western ore field the pre-Variscan scheelite mineralization has been linked to the K2 orthogneisses with its associated apical quartz mass and the K2 eruption breccia (Höll and Eichhorn, 2000).

According to this model a second mineralization stage (Scheelite 2) is associated with the intrusion of the K1-K3 orthogneiss. Disseminated scheelite mineralization within the K1-K3 orthogneiss and large scheelite crystals in quartz-scheelite veins crosscutting the orthogneiss and its surrounding host rocks are assigned to this stage. The association of scheelite with the Early Carboniferous K1-K3 orthogneiss is interpreted as the result of assimilation of pre-existing Cambrian scheelite during granite emplacement. Variscan metamorphism resulted in further redistribution of scheelite (Scheelite 3) along the Variscan foliation planes, crosscutting quartz-veins and shear zones. Alpine metamorphism only caused very local remobilization of scheelite in metamorphic quartz veins (Scheelite 4).

3 Methods and analytical techniques

3.1 Major and trace element whole rocks analyses

3.1.1 Sample preparation

The whole rock major and trace element composition of 83 samples from various lithologies of the W-deposit and local Zentralgneise were analyzed. From each sample, 2-10 kg sample material was crushed in a jaw crusher and grinded to a grain fraction <3 mm by a disc mill operated by Wolfram Bergbau und Hütten AG (WBH) at the beneficiation plant near the mine. The used grinding discs were made of high-alloy stainless steel (ferrochrome; 83 mass% Fe, 14 mass% Cr, 1.7 mass% Si; written communication WBH). The use of tungsten carbide components was avoided to prevent artificial W contamination by abrasion during grinding. Afterwards, sample material was separated by a riffle splitter into representative sub-samples of roughly 250 g each. The sub-samples were further grinded for 7 min to achieve a grain size <0.0063 mm approximately by using a vibrating cup mill equipped with an agate grinding set at the Chair of Petroleum Geology, Montanuniversität Leoben (MUL). The fine grained material was manually homogenized and 20 g of each sample were shipped to an external laboratory for chemical analysis.

3.1.2 ICP-AES and ICP-MS analyses

The chemical analyses of whole rock major and trace elements were performed by Bureau Veritas Minerals Laboratories (BVML), formerly Acme Analytical Laboratories Ltd., Vancouver Office (Canada) referring to the analytical package LF202 (BVML 2015). Eleven major oxides and Sc were determined by solution inductively coupled plasma – atomic emission spectrometry (ICP-AES) following a lithium borate fusion and dilute acid digestion. Additionally, 45 trace elements were analyzed by solution inductively coupled plasma – mass spectrometry (ICP-MS). For dissolution of the sample material lithium borate fusion (rare earth and refractory elements) and hot aqua regia digestion (precious and base metals) were used. The analytical package also included determination of loss on ignition (LOI) by sintering at 1000°C and Leco analysis for total carbon and sulphur. Iron was measured as total $FeO+Fe_2O_3$. Data quality was assured by duplicate measurements of reference materials used by the laboratory itself. Additional quality control was obtained through analysis of the certified reference material “NIM-G Granite SARM 1” (Mallett 1984) as unknown. Certified chemical concentrations and analytical

results obtained by BVML are compared in table 3.1. The analytical results conform well to the reported values by Mallet (1984). Moreover, F concentrations of 39 whole rock samples were analyzed referring to the analytical package GC840 (BVML 2015) by using a specific ion electrode.

Element	Mallett (1984)	BVML	1σ uncertainty
SiO_2	75.70	75.78	0.002
Al_2O_3	12.1	11.96	0.070
Fe_2O_3	2.00	1.91	0.045
CaO	0.78	0.77	0.005
Na_2O	3.36	3.24	0.060
K_2O	4.99	4.98	0.005
Ce	195	215	10
Cr	12.0	14.0	1.0
Cu	12.0	10.0	1.0
Eu	0.35	0.32	0.015
Ga	27	26	0.50
La	109	117	4.0
Mn	160	155	2.5
Nb	53	47	3.0
Nd	72	71	0.50
Pb	40	38	1.0
Rb	325	304	10.5
Sm	15.8	14	0.90
Sr	10.0	9.90	0.05
Tb	3.0	2.70	0.15
Th	51	51	0.00
Ti	540	540	0.00
Y	143	126	8.5
Yb	14.2	14	0.10
Zn	50	52	1.0
Zr	300	266	17

Tab. 3.1 Comparison of certified chemical concentrations (Mallett 1984) and analytical results obtained by Bureau Veritas Minerals Laboratories (BVML) for reference material “NIM-G Granite SARM 1”. Concentrations of oxides are reported in mass%, other elements in ppm. Uncertainties are quoted as 1σ.

3.2 Major and trace element mineral analyses

3.2.1 Electron probe microanalyses

Major and trace element compositions of main and accessory phases in 35 polished thin sections from the deposit and adjacent Zentralgneise were analyzed by electron probe microanalyzer (EPMA) using the JEOL JXA 8200 superprobe of UZAG Steiermark, installed at the Chair of Resource Mineralogy (MUL).

Elements were quantitatively analyzed in wavelength-dispersive system (WDS) using the measurement conditions summarized in table 3.2. The electron beam was operated in focused mode with a beam diameter of ~1 µm. However, a defocused beam with a diameter of 5 µm was used for quantitative analyses of F in apatite to minimize variation in the X-ray counting rates during exposure of apatite to the electron beam (cf. Goldoff et al. 2012; Pyle et al. 2002; Stormer et al. 1993). Raw data were corrected for the matrix effect by the ZAF-method. Mineral formulae, with exception of allanite, were calculated using the software NORM v 4.0 (Ulmer 1993). Allanite formulae were calculated on the basis of 6 cations (M+T) and 25 charges (Ercit 2002) using a MS Excel© spreadsheet.

3.2.2 Laser ablation ICP-MS analyses

In-situ laser ablation – sector field – inductively coupled plasma – mass spectrometry (LA-SF-ICP-MS) analyses of major and trace elements of scheelite, apatite and zircon were performed at the Institute of Mineralogy at the Johann Wolfgang von Goethe University Frankfurt (JWG). Detailed information on the sample preparation and the LA-SF-ICP-MS setup is given in chapters 3.3.1 and 3.3.2, respectively.

Laser spot sizes were 50 µm for scheelite and zircon, and 33 µm for apatite at a repetition rate of 5.5 Hz. Analysis time for each spot was overall 60 s, with 30 s for the background (no ablation) and 30 s for the sample. Intensities of following isotopes were recorded (zrn= zircon only; as= apatite and scheelite only): ^{7}Li, ^{11}B, ^{23}Na (as), ^{29}Si, ^{31}P (zrn), ^{44}Ca, ^{45}Sc (as), ^{49}Ti, ^{50}V (as), ^{55}Mn (as), ^{57}Fe, ^{63}Cu (as), ^{66}Zn (as), ^{75}As (as), ^{85}Rb, ^{88}Sr, ^{89}Y, ^{90}Zr (as), ^{93}Nb, ^{97}Mo (as), ^{139}La, ^{140}Ce, ^{141}Pr, ^{146}Nd, ^{147}Sm, ^{151}Eu, ^{157}Gd, ^{158}Gd, ^{159}Tb, ^{161}Dy, ^{165}Ho, ^{167}Er, ^{169}Tm, ^{172}Yb, ^{175}Lu, ^{178}Hf (zrn),^{181}Ta (zrn), ^{183}W (zrn), ^{206}Pb (as), ^{208}Pb (as), ^{209}Bi (as), ^{232}Th, ^{238}U. The GJ-1 zircon, NIST SRM-612 and NIST SRM-614 reference materials were monitored as external standards during the analytical session. Raw data were processed using the software GLITTER™ (Griffin et al. 2008). The average analytical uncertainty (1σ) ranges for all elements between 3 and 11 %; only P concentrations (38 %) show much higher uncertainties. The averaged Si concentration (15.2 mass%) of zircon, determined with EPMA was used as internal standard.

Biotite Acceleration voltage: 15 kV Beam current: 10 nA

Element	Crystal	Line	Counting time peak [s]	Counting time background [s]	Standard	Detection limit [ppm]
F	LDE1	Kα	20	10	F-phlogopite	510
Na	TAP	Kα	20	10	albite	260
K	PETH	Kα	20	10	orthoclase	70
Si	PETH	Kα	20	10	orthoclase	165
Cl	PETJ	Kα	20	10	atacamite	195
Fe	LIFH	Kα	20	10	almandine	310
Ca	PETJ	Kα	20	10	Cr-diopside	240
Ti	LIFH	Kα	20	10	ilmenite	230
Ba	PETJ	Kα	20	10	barite	640
Mn	LIFH	Kα	20	10	rhodonite	280
Mg	TAP	Kα	20	10	olivine	180
Al	TAP	Kα	20	10	orthoclase	145

Zircon Acceleration voltage: 20 kV Beam current: 20 nA

Element	Crystal	Line	Counting time peak [s]	Counting time background [s]	Standard	Detection limit [ppm]
Ca	PETJ	Kα	30	15	apatite	75
Si	PETH	Kα	20	10	zircon	120
Zr	PETH	Lα	20	10	zircon	230
Pb	PETJ	Mα	30	15	galenite	240
Hf	LIFH	Lα	30	15	pure Hf (100%)	240
U	PETH	Mα	30	15	uraninite	120
Th	PETH	Mα	30	15	monazite	140

Scheelite Acceleration voltage: 20 kV Beam current: 10 nA

Element	Crystal	Line	Counting time peak [s]	Counting time background [s]	Standard	Detection limit [ppm]
F	LDE1	Kα	20	10	fluorite	400
Ca	PETH	Kα	20	10	diopside	85
Mo	PETH	Lα	20	10	molybdenite	350
W	LIFH	Lα	20	10	pure W (100%)	660

Apatite Acceleration voltage: 15 kV Beam current: 10 nA

Element	Crystal	Line	Counting time peak [s]	Counting time background [s]	Standard	Detection limit [ppm]
Mg	TAP	Kα	20	10	olivine	170
F	TAP	Kα	20	10	fluorite	2000
Ca	PETJ	Kα	20	10	apatite	220
P	PETH	Kα	20	10	apatite	145
Mn	LIFH	Kα	20	10	rhodonite	365
Na	TAP	Kα	20	10	adularia	230
Cl	PETJ	Kα	20	10	atacamite	155
Sr	PETH	Lα	20	10	celestine	330
Fe	LIFH	Kα	20	10	chromite	350
Sr	PETJ	Kα	20	10	chalcopyrite	570
Si	PETH	Kα	20	10	adularia	175

Table is continued on the next page

Pyrochlore Acceleration voltage: 30 kV Beam current: 40 nA

Element	Crystal	Line	Counting time peak [s]	Counting time background [s]	Standard	Detection limit [ppm]
Si	TAP	Kα	20	10	kaersutite	125
Ti	PETJ	Kα	20	10	rutile	65
Nb	PETH	Lα	50	25	coltan	80
Ta	LIFH	Lα	20	10	coltan	195
Ca	PETJ	Kα	20	10	kaersutite	50
U	PETH	Mα	50	25	uraninite	55
Mn	LIFH	Kα	20	10	coltan	42
Sn	PETJ	Lα	20	10	cassiterite	175
Fe	LIFH	Kα	20	10	coltan	55
Sc	PETJ	Kα	20	10	pure Sc (100%)	50
W	LIFH	Lα	20	10	coltan	280
Zr	PETJ	Lα	20	10	pure Zr (100%)	165
Hf	LIFH	Lα	20	10	pure Hf (100%)	125

Titanite/ Allanite Acceleration voltage: 15 kV Beam current: 10 nA

Element	Crystal	Line	Counting time peak [s]	Counting time background [s]	Standard	Detection limit [ppm]
F	LDE1	Kα	20	10	fluorite	70
Na	TAP	Kα	20	10	kaersutite	180
K	PETJ	Kα	20	10	phlogopite	90
Si	PETH	Kα	20	10	almandine	170
Y	PETH	Lα	20	10	Y-Al-garnet	165
Al	TAP	Kα	20	10	almandine	140
Ca	PETJ	Kα	20	10	wollastonite	400
Nb	PETJ	Lα	20	10	pure Nb (100%)	350
Fe	LIFH	Kα	20	10	almandine	260
W	PETH	Mα	20	10	pure W (100%)	450
Mg	TAP	Mα	20	10	almandine	140
P	PETJ	Mα	20	10	monazite	850
Ta	LIF	Lα	20	10	pure Ta (100%)	690
La	LIFH	Lα	20	10	monazite	370
U	PETH	Mα	20	10	uraninite	140
Th	PETJ	Mα	20	10	Th glass	310
Dy	LIFH	Lβ	20	10	REE glass	480
Ti	LIFH	Kα	20	10	rutile	350
Cl	PETJ	Kα	20	10	atacamite	300
Nd	LIFH	Lα	20	10	REE glass	290
Mn	LIFH	Kα	20	10	rhodonite	210
Pr	LIFH	Lα	20	10	monazite	420
Ce	LIFH	Lα	20	10	monazite	440
Yb	LIFH	Lα	20	10	REE glass	360
Sm	LIFH	Lβ	20	10	REE glass	470
Gd	LIFH	Lβ	20	10	REE glass	440
Tb	LIFH	Lα	20	10	REE glass	310

Tab. 3.2 EPMA measurement conditions and standards used for biotite, zircon, scheelite, apatite, pyrochlore, titanite, and allanite analyses.

3.3 In-situ isotope analyses of minerals by laser ablation ICP-MS

3.3.1 Sample preparation

Sample preparation was done in 2013 and 2014, following the consecutive steps described below. The specific mechanical processing was carried out in the beneficiation plant near the mine (WBH) and in the respective laboratories of the Chair of Resource Mineralogy and the Chair of Mineral Processing at MUL. Further concentration of the sample material was achieved in the laboratories of the Institute of Mineralogy at JWG. However, the processing chain differs slightly for the two years because of technical problems with the electric pulse disaggregator at MUL.

In 2013, sample material (AP-1124, Gn-1065b, Gn-1262, K1-725, K1-1100, K1-1152, SP-25/34, ST-03/30) was crushed in a jaw crusher and afterwards grinded to a grain fraction <3 mm by a disc mill (WBH). Afterwards, minerals were liberated by using the electric pulse disaggregation technology at MUL (Rudashevsky et al. 1995). The disaggregated material was wet classified and the mineral fraction 250-40 µm was further processed at JWG by conventional separation methods using a Wilfley shaking table and Frantz magnetic separator. Density separation of the non-magnetic mineral fraction (>1.6 A) was performed by using methylene iodide (ρ ~3.31 g/cm^3) as a heavy liquid. The respective heavy fraction – containing scheelite, apatite, and zircon – was washed with ammonia and then dried. Minerals were hand-picked in ethanol from the heavy mineral fraction under a binocular and classified into different fractions based on their shape, size, and morphology. The hand-picked grains were mounted in a 25 mm-diameter circular epoxy mount (Araldite® 20/20) and polished down to expose the inner core domains. Internal structures of the minerals were subsequently identified by back scatter electron (BSE)- and cathodoluminescence (CL)- imaging, using the JEOL JSM 6490 scanning electron microscope (SEM) at JWG.

In 2014, sample material (AP-3.82, Gn-1038a, FB-09/30, FB-12/30, FS-1) was crushed by a jaw crusher at MUL to a grain fraction <1 mm and subsequently dry classified. The mineral fraction 250-40 µm was further separated by a Wilfley shaking table at JWG. This time, bromoform (ρ ~2.88 g/cm^3) was used as heavy liquid for density separation. The washed and dried heavy mineral fraction was further processed by Frantz-magnetic separation to obtain the magnetic fraction >1.6 A. The reason for switching the last two steps in 2014 was that the quantity of sample material left after the

shaking table was too big for magnetic separation. Further processing steps (hand-picking, mounting, and SEM documentation) were identical with those in 2013.

3.3.2 U-Pb isotope analyses of zircon

Zircons were analyzed in-situ for U, Th, and Pb isotopes by laser ablation – sector field – inductively coupled plasma – mass spectrometry (LA-SF-ICP-MS) at JWG, using the method as described in Gerdes and Zeh (2006, 2009) and Zeh and Gerdes (2012). Samples were mounted within a two-volume ablation cell (Laurin Technic, Australia) and ablated by a Resolution S-155 193 nm ArF Excimer (Resonetics) laser system connected to a Thermo-Scientific Element 2 sector field ICP-MS. Ablation of the sample occurred in a 0.60 l min^{-1} He stream, which was mixed after ablation with 0.004 l min^{-1} N_2 and Ar (sample carrier gas). The purity of the gases is reported with 99.999 %.

Laser spot sizes were 26 µm for GJ-1 and Plešovice standard zircons and 50 µm for the 91500 reference zircon; a spot size of 26 µm and a pulse rate of 5 Hz were used for unknowns. The signal was tuned to obtain the maximum sensitivity for U and Pb, while avoiding oxide production in the plasma. To prevent measuring impurities on the crystal surface, samples were pre-ablated each time before the actual analysis started.

Raw data were corrected offline for background signal, common Pb, laser-induced elemental fractionation, instrumental mass discrimination, and time-dependent elemental fractionation of Pb/U using an in-house MS Excel© spreadsheet program (Gerdes and Zeh 2006, 2009). The common lead correction was based on the interference- and background-corrected ^{204}Pb signal and the radiogenic ^{208}Pb content (see details in Millonig et al. 2012). Uncertainties induced by laser-induced elemental fractionation and instrumental mass discrimination were minimized by normalizing the $^{206}Pb/^{238}U$ ratio to the standard zircon GJ-1 ($^{206}Pb/^{238}U$ = 0.0982 ± 0.0004, ID-TIMS JWG “true” value). The external reproducibility of the $^{206}Pb/^{238}U$ ratio of GJ-1 during the analytical session (267 unknowns, 16 GJ-1 analyses) is 1.36 % (2σ). The reported uncertainties (2σ) of the $^{206}Pb/^{238}U$ ratio were propagated by quadratic addition of the external reproducibility of the GJ-1 standard zircon and the within-run precision of each analysis (2σ) (Zeh and Gerdes 2012). The uncertainties for the $^{207}Pb/^{206}Pb$ ratio were propagated by using a ^{207}Pb signal dependent uncertainty. Consequently, the $^{207}Pb/^{235}U$ ratios could be derived from the normalized and error propagated $^{207}Pb/^{206}Pb$ and $^{206}Pb/^{238}U$ ratio by assuming a $^{238}U/^{235}U$ natural abundance of 137.88; uncertainties were derived by quadratic addition of the propagated uncertainties of both ratios (Zeh and Gerdes 2012).

The accuracy of this method was controlled through repeated measurement of the Plešovice reference zircon (concordia age = 338.7 ± 2.1 Ma, MSWD of concordance = 1.04, probability of concordance = 0.31, n = 6) and the 91500 reference zircon (concordia age = 1061.7 ± 5.6 Ma, MSWD of concordance = 0.054, probability of concordance = 0.82, n = 8). This is in good agreement with the published values of 337.13 ± 0.37 Ma for the Plešovice reference zircon (Sláma et al. 2008) and 1065 Ma for the 91500 reference zircon (Wiedenbeck et al. 1995). Concordia diagrams were drawn with the software Isoplot 4 (Ludwig 2012).

3.3.3 Lu-Hf isotope analyses of zircon

The same zircons that had been analyzed for U-Pb were additionally analyzed for their Lu-Hf isotopic composition at JWG, following the method described in Gerdes and Zeh (2006, 2009) and Zeh and Gerdes (2012) and using a Thermo-Scientific Neptune multicollector ICP-MS coupled to the same laser as described above. Data were collected in static mode with a laser spot size of 40 µm. To ensure that the spot for analyzing Lu-Hf isotopes is identical to the respective growth zone considered previously for U-Pb dating, the Lu-Hf laser spot was drilled on top of the U-Pb laser spot wherever it was possible. The Ar sample carrier gas was mixed with 0.007 l min^{-1} N_2 to suppress oxide production in the plasma. The isotopes ^{172}Yb, ^{173}Yb and ^{175}Lu were simultaneously detected during each analysis to correct for isobaric interferences of Lu and Yb isotopes on mass 176. By utilizing an in-house value for the $^{176}Lu/^{175}Lu$ ratio of 0.02658 and $^{176}Yb/^{173}Yb$ ratio of 0.79502 it was possible to calculate ^{176}Lu and ^{176}Yb. Hafnium and Yb isotopic ratios were corrected for the instrumental mass bias by calculating the mass bias factors (β) for Hf and Yb, using an exponential law and normalizing to the natural $^{179}Hf/^{177}Hf$ ratio (0.7325; Patchett et al. 1982) and $^{172}Yb/^{173}Yb$ ratio (1.3535; mean of Chu et al. 2002 and Segal et al. 2003). The instrumental induced mass bias of Lu was assumed to be similar to Yb. The accuracy and external reproducibility of the analytical method was tested by replicate measurements of the reference zircons GJ-1 and Plešovice, which yielded a $^{176}Hf/^{177}Hf$ of 0.282009 ± 0.000020 (2σ, n = 12) and 0.282481 ± 0.000020 (2σ, n = 7), respectively. Both ratios obtained in this work excellently coincide with published values for the zircons GJ-1 (0.282003 ± 0.000018; Gerdes and Zeh 2006) and Plešovice (0.282482 ± 0.000013; Sláma et al. 2008).

For calculation of εHf_t values a decay constant of 1.867 x 10^{-11} (average of Scherer et al. 2001 and Söderlund et al. 2004) and the values for the chondritic uniform reservoir (CHUR, $^{176}Lu/^{177}Hf$ = 0.0336, $^{176}Hf/^{177}Hf$ = 0.282785; Bouvier et al. 2008) were used. The

initial $^{177}Hf/^{176}Hf$ ratios and εHf_t for all analyzed zircon domains were calculated with the corresponding $^{206}Pb/^{238}U$ age. A two stage depleted mantle Hf model age (T_{DM}, in Ga) was calculated from the initial $^{177}Hf/^{176}Hf$ of each zircon at the time of crystallization (in terms of the apparent $^{206}Pb/^{238}U$ age) by using $^{176}Hf/^{177}Hf = 0.28325$ and $^{176}Lu/^{177}Hf = 0.0384$ for the bulk earth (Bouvier et al. 2008) and $^{176}Lu/^{177}Hf = 0.0113$ for the average crust (Wedepohl, 1995).

3.3.4 Rb-Sr isotope analyses of apatite and scheelite

Strontium isotope measurements were performed with a Thermo-Finnigan Neptune multi collector ICP-MS at JWG coupled to a Resolution S-155 193 nm ArF Excimer (Resonetics) laser system during two analytical sessions (August 2013 and June 2014). Key instrument parameters and operating conditions are listed in Table 3.3. The laser spot size (50-190 µm) was chosen depending on size and Sr concentration of the particular area of the individual grains. Each analysis included 25 s acquisition of background and 25-35 s of laser ablated material with an integration time of 0.52 s. Outliers were rejected based on a 2σ criterion for all data with ^{88}Sr signal >0.5 V. The instrumental mass bias for Sr isotopes was corrected using an exponential law function and a $^{86}Sr/^{88}Sr$ of 0.1194. For Rb isotopes the mass bias was corrected using the Sr mass bias of the individual integration step multiplied by a daily ascertained βSr/βRb offset factor. This offset factor was determined empirically from analyses of NIST soda-lime glass SRM 610, which was measured (130 µm spot) at the beginning and end of each analytical session. The aim was to correct the enormous isobaric interference (>400 %) of ^{87}Rb on ^{87}Sr in case of the NBS 610. Woodhead and Hergt (2001) reported a solution mode TIMS $^{87}Sr/^{86}Sr$ ratio of 0.70969 for NBS 610. Selection of the offset factor was based on the first two SRM 610 analyses and applied to all subsequent analyses. Typical $^{87}Sr/^{86}Sr$ of SRM 610 was 3.265 before correction and 0.7093 ± 0.0008 (n = 6) afterwards. Correction of interferences of Kr isotopes (impurities in the Ar gas) on mass 84 (e.g. 0.051 V) and 86 (e.g. 0.016 V) was successfully accomplished by background subtraction. Almost all analyses yielded $^{84}Sr/^{86}Sr$ of 0.05648 after correction. Elevated rare earth element contents in apatite make it necessary to correct for isobaric interferences by doubly-charged Er and Yb isotopes (168^{2+}, 170^{2+}, 172^{2+}, 174^{2+}, and 176^{2+}) on mass 84, 85, 86, 87, and 88. This was done by monitoring the half masses 83.5, 84.5 and 86.5 and using the natural Yb and Er isotope ratios, the Sr mass bias of the individual integration step, and an empirical determined βSr/βYb offset factor. The latter was determined using the SRM 610 in the same way as described for the βSr/βRb. Typical corrections for apatite were in the range of 0.01 to

0.0001 on the $^{87}Sr/^{86}Sr$. Durango apatite was analyzed to monitor and verify the accuracy of the corrections (see below).

Prior to laser measurements the Neptune was tuned using 150 ppb SRM 987 solution aspirated with a standard glass spray chamber using a PFA-100 micro-flow nebulizer (Elemental Scientific). All data acquired during the subsequent analytical session were adjusted relative to the NBS 987 of $^{87}Sr/^{86}Sr$ 0.710248. Quoted uncertainties are quadratic additions of the within run precision of each analysis and the reproducibility of the in-house plagioclase standard MIR-a (2σ = 0.006%, n = 15). Accuracy and daily reproducibility of the method was verified by repeated analyses of Durango apatite and MIR-a, which yielded $^{87}Sr/^{86}Sr$ of 0.70634 ± 0.00007 (2σ, n = 36) and 0.70309 ± 0.00004 (n = 29), respectively. This is in perfect agreement with previously published TIMS results (e.g. Horstwood et al. 2008; Rankenburg 2002) and the LA-MC-ICPMS long-term average of MIR-a (0.70309 ± 0.00005; n > 100) and Durango apatite (0.70634 ± 0.00008, n > 50) at JWG.

Neptune MC-ICP-MS	
Plasma gas flow rate	15 l min^{-1}
Auxiliary gas flow rate	0.82 l min^{-1}
Interface cones	Nickel
Collectors	Faraday at $10^{-11}\Omega$
Mass resolution	400 m/z
Typical sensitivity (Total Sr solution)	90 V/µg g^{-1}
Laser ablation system (Resolution, Resonetics)	
CompexPro 102 ArF excimer	193 nm
Ablation cell	S-155
Energy density	4-5 J cm^{-2}
Helium gas flow rate	0.60 l min^{-1}
Argon gas flow rate	0.90 l min^{-1}
Effective volume	~ 1.8 cm^3
Spot size (diameter)	50 - 190 µm
Repetition rate	6 Hz

Tab. 3.3 Key instrument parameters and operating conditions for Sr isotope determination by laser ablation.

3.4 Gamma-ray spectrometry

In winter 2014/15 field gamma-ray spectrometric analyses were performed on selected lithologies within the underground mine. In addition, analyses were repeated on four samples under laboratory conditions at the Chair of Applied Geophysics, MUL.

The measurements were carried out with a hand-held GS-256 gamma-ray spectrometer – manufactured by Geofyzika Brno – equipped with a 3" x 3" thallium-activated sodium iodide [NaI(Tl)] scintillator detector connected to a 256 channel spectrometer unit. Detection time was 300 s for each analysis in which gamma rays emitted from the decay of ^{40}K, ^{232}Th and ^{238}U in the near-surface areas of the rocks were detected simultaneously. Potassium is directly measured at the energy peak of 1.46 MeV and the concentration is given in mass% K. Uranium and Th are indirectly quantified by detecting the ^{214}Bi peak at 1.76 MeV from the ^{238}U decay series and the ^{208}Tl peak at 2.62 MeV from the ^{232}Th decay series, respectively; concentrations are reported in ppm eU (equivalent uranium) and ppm eTh (equivalent thorium). A quick identification of lithologies with a high gamma ray emission and high radiogenic heat production rate can be made basically in the field by comparing the counts detected per measurement interval. However, the detected counts are related to the geometry and mass of the source. If the detector is placed evenly on the rock surface, the effective sample has a thickness of approximately 25 cm, a radius of 1 m and a mass exceeding 100 kg, depending on the respective density (IAEA 2003).

To account for the exact geometry, four samples were measured in the laboratory. Each sample was measured three times and the signal intensities were averaged. To avoid external influences, the samples were shielded by a lead housing during analysis. The averaged counts per measurement interval were background subtracted and converted into a count rate per minute. Sensitivity factors for instrumental calibration were determined by using several in-house standards with known chemical composition and varying sample geometry (Table 3.4) to calculate the concentrations of K, Th and U.

	Standard	
Element	**h**	**c**
K	9.808 cm	0.1744 mass%
Th	1.885 cm	0.2132 ppm
U	0.459 cm	0.1768 ppm

Tab. 3.4 In-house standard parameters used for calculating the sensitivity factors of unknowns. h= sample thickness, c= element concentration.

4 Sample description and petrography

4.1 Felbertal scheelite deposit

4.1.1 Introduction

Sampling of the K1-K3 orthogneiss and the aplite gneiss from the western ore field was conducted in the presence of WBH mine geologist Marie-Luise Pecher during the years 2012 and 2013; additionally, quartz-scheelite veins crosscutting the K1-K3 orthogneiss were considered. Moreover, samples of intermediate quartz-diorite gneiss dikes, amphibolites and Early Paleozoic orthogneisses were taken for comparison. This work was focused on the western ore field. Two samples of laminated scheelite-quartz ores (FT-74, FS-1) from the eastern ore field (abandoned open pit) are from archive material of previous projects. Such high-grade ores are not exposed in-situ anymore. These were considered for Rb/Sr isotopic studies of Scheelite 1.

In the course of this study a research drilling campaign aimed to drill through the K1-K3 orthogneiss body on the levels 1175 m (drill holes UB-343, UB-344) and 675 m (drill hole UB-356); however only UB-343 and UB-344 intersected the K1-K3 orthogneiss and were considered for further sampling. The idea was to obtain relevant information on the petrographic, mineralogical and geochemical homogeneity of the original K1-K3 orthogneiss body and its contacts to the respective host rock along a complete section/profile through this gneiss body in order to detect possible variations (e.g. between core and marginal parts). The results and insights attained from 18 analyzed drill core-samples should contribute to identify possible proximity indicators for further exploration.

Altogether, 62 samples including the samples form the drill cores were collected in the western ore field (Fig. 4.1). Site plans of the respective underground levels with the detailed sampling localities are reported in Appendix A. A brief overview of the petrography of considered lithologies and related samples is given in this chapter with the respective samples italicized at the beginning of each subchapter. The sorting of the samples is in first order alphabetically and in second order numerical and does not represent any geographical relevance.

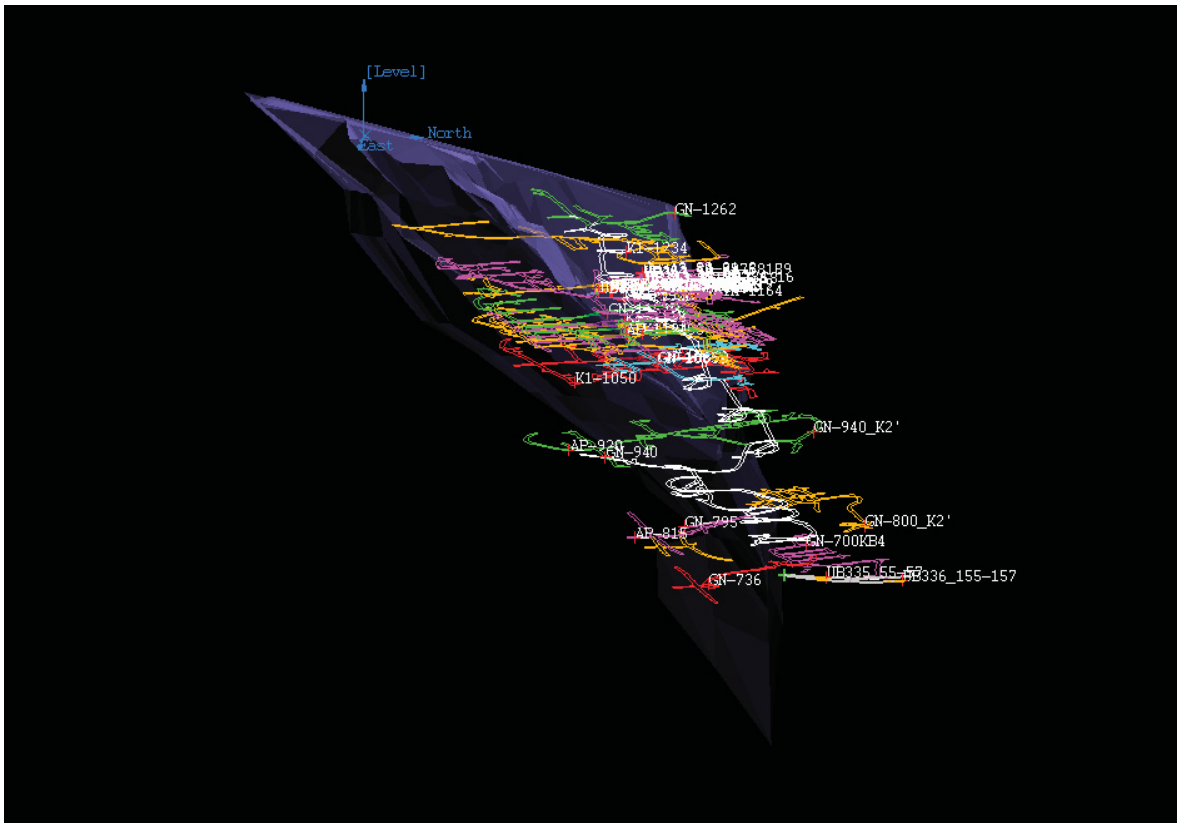

Fig. 4.1 Illustration of all sample localities in the western ore field. The mine workings are shown in different colors. The Basal Schist wedge (purple) separates the western ore field into a hanging wall and footwall. Most samples were taken from the upper levels of the deposit. Viewing direction is towards west.

4.1.2 K1-K3 orthogneiss and aplite gneiss

A-K1h, AP-815, AP-820, AP-1124, B-K1h, B-K1d-a, B-K1d-b, B-K1d-c, C-K1h-a, C-K1h-b, C-K1d-a, C-K1d-b, C-K1d-c, C-K1d-d, C-K1d-e, Gn-700KB4, Gn-1065a, Gn-1065b, Gn-1152a, K1-23.29, K1-26.80, K1-31.59b, K1-43.57, K1-44, K1-45.59, K1-48, K1-59, K1-74.50, K1-76.28, K1-80a, K1-80b, K1-725, K1-1100, K1-1152, K1-1234

The K1-K3 orthogneiss is exposed in the western ore field in the higher levels of the underground mine, either as several 10 m-thick plutonic bodies (e.g. level 1164 m) or as thin (<10 m) lamellae (e.g. level 1050 m; APPENDIX B). Recent mining activity and mapping in the lower levels revealed K1-K3 orthogneiss equivalents in form of m-thick gneiss bodies at the 725 m (sample K1-725) and 700 m levels (sample Gn-700KB4).

The former WBH mine geologist D. Briegleb distinguished between a dark-colored (Fig. 4.2a) and a light-colored (Fig. 4.2b) variety of the K1-K3 orthogneiss for the first time. This discrimination is made in the field by the higher modal abundance of biotite in the dark-colored K1-K3 orthogneiss as compared to the light-colored variety (Jahoda 1984).

Additionally, Briegleb described leucocratic aplite gneisses (Fig. 4.2c), which he interpreted as the late-stage residual melts from which the K1-K3 orthogneiss had formed (written communication). Later, Finger et al. (1985) and von Quadt (1985) discussed the occurrence of the dark-colored and light-colored variety and assigned the dark-colored K1-K3 orthogneiss to the stronger deformed margins of the main K1-K3 orthogneiss body. Schenk (1990) argued for a more inhomogeneous distribution and intercalation of both varieties and ascribed the distinct orthogneiss types to primary lithological differences. In contrast, D. Briegleb and B. Lehmann (written communication) interpreted the two K1-K3 orthogneiss varieties as distinctive intrusive stages of the same magmatic protolith but showing a variable degree of differentiation. The intrusive nature of the K1-K3 orthogneiss is proven by the occurrence of apophyses branching into the host rocks (Fig. 4.2d); though sharp contacts between both varieties usually prevail (Fig. 4.2e). The sheet-like geometry of the K1-K3 orthogneisses may imply syn- to post-emplacement disintegration of the plutonic body during subsequent tectonic overprints (Schenk 1990).

The K1-K3 orthogneiss is crosscut by various vein structures that are also observed in the surrounding host rocks (chapter 4.1.7). The most obvious veins are mm- to several dm-thick quartz-scheelite veins (Fig. 4.2e) that crosscut the K1-K3 orthogneiss and the metabasic members of the LMS. Additionally, quartz-masses on top of the K1-K3 orthogneiss contained low- to high grade scheelite mineralization. Disseminated scheelite is also common in the K1-K3 orthogneiss.

Petrographically, the K1-K3 orthogneiss is a fine- to medium-grained high-silica albite-microcline orthogneiss with differing amounts of biotite and muscovite. Primary magmatic textures in form of porphyritic feldspars (<5 mm) are rarely preserved. Generally, the foliation is indicated by the alignment of micas with quartz and feldspars forming the granoblastic matrix. In most scientific publications (e.g. Eichhorn et al. 1999), the K1-K3 orthogneiss is commonly described as muscovite-microcline orthogneiss, which refers best to the light-colored K1-K3 orthogneiss variety. The elevated muscovite and low biotite contents give the light-colored K1-K3 orthogneiss a silver-grey to greenish coloration; however, muscovite is rare in the dark-colored variety where biotite is the predominant mica (Fig. 4.2f). Thus the dark-colored K1-K3 orthogneiss variety should be described as biotite-albite orthogneiss.

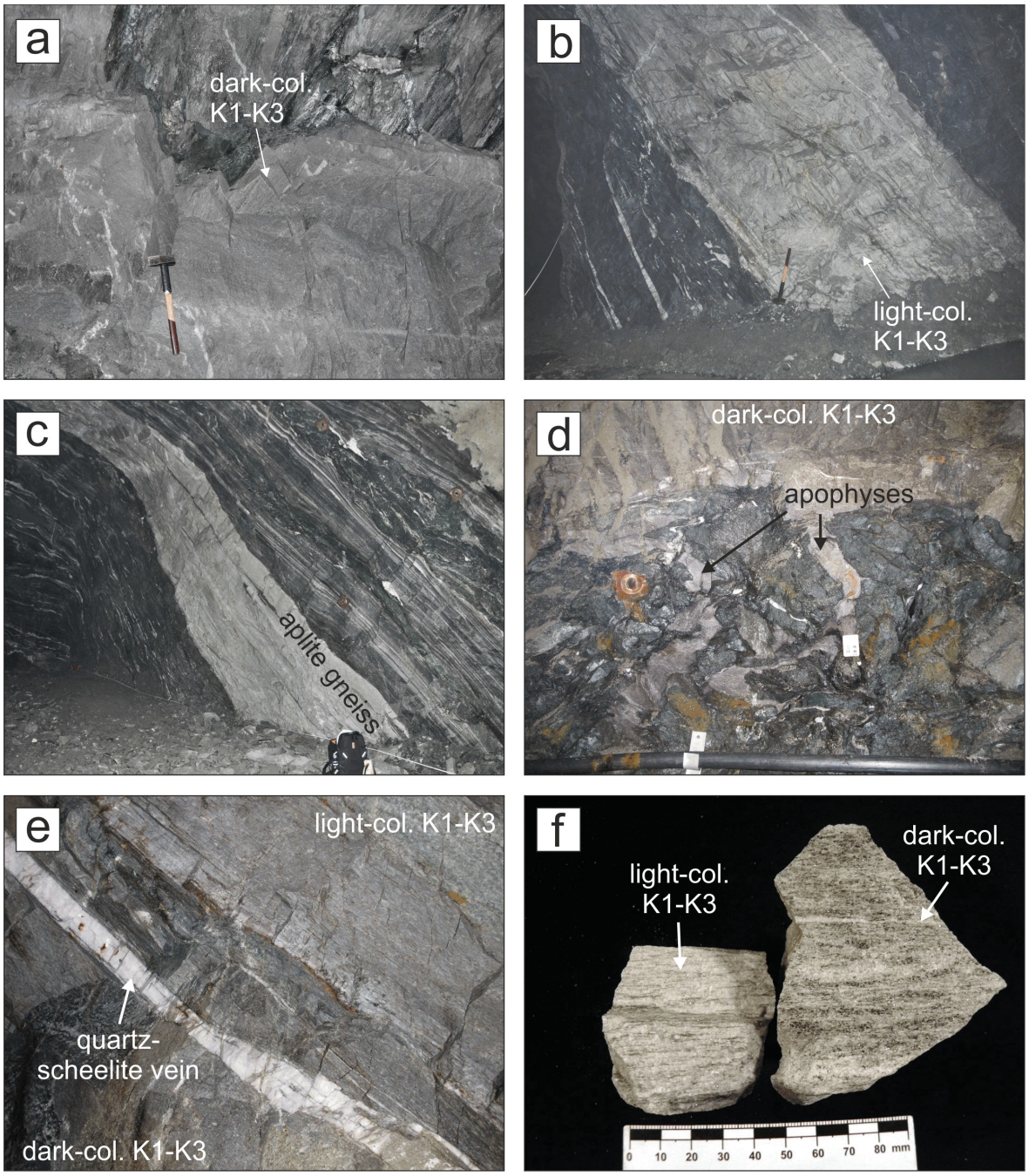

Fig. 4.2 Photographs of the K1-K3 orthogneiss in the underground mine on different levels. **a)** Dark-colored (dark-col.) K1-K3 orthogneiss; level 1065 m. **b)** Lamella of light-colored (light-col.) K1-K3 orthogneiss; level 1050 m. **c)** Aplite gneiss dike; level 940 m. **d)** Intrusive contact (apophyses) between dark-colored K1-K3 orthogneiss and fine-grained amphibolite; level 1164 m. **e)** Sharp contact between the dark-colored and light-colored K1-K3 orthogneiss varieties with a quartz-scheelite vein crosscutting the gneiss parallel to the schistosity; level 1164 m. **f)** Comparison of light-colored K1-K3 orthogneiss sample C-K1h-a (left) and dark-colored K1-K3 orthogneiss sample C-K1d-a (right).

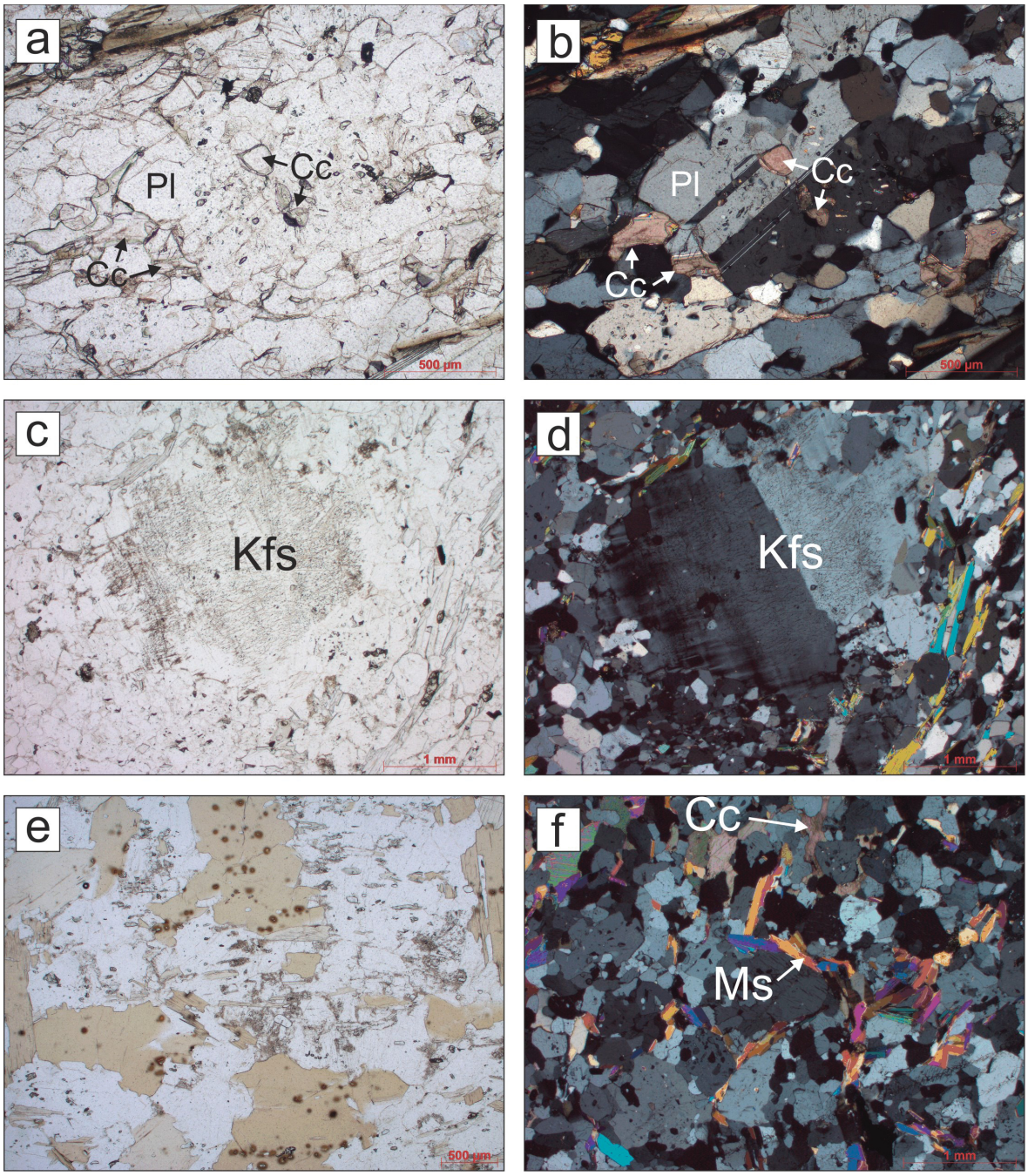

Fig. 4.3 Photomicrographs of the K1-K3 orthogneiss under parallel and crossed polarizers. **a)** Plagioclase (Pl) with inclusions of calcite (Cc); dark-colored K1-K3 orthogneiss sample C-K1d-a, plane polarized light. **b)** The same microarea in cross polarized light. The polysynthetic twin lamellae are clearly visible. **c)** Potassium feldspar (Kfs) porphyroclast with altered core and fresh rim; light-colored K1-K3 orthogneiss sample C-K1h-a, plane polarized light. **d)** The same microarea in cross polarized light. Clearly visible is the commencing transformation to microcline at the rim. **e)** Large biotite flakes with numerous zircon inclusions; dark-colored K1-K3 orthogneiss sample C-K1d-b, plane polarized light. **f)** Muscovite (Ms) and calcite (Cc) post-tectonically crystallized between the grain boundaries of feldspars and quartz; light-colored K1-K3 orthogneiss sample K1-31.59; crossed polarizers.

Under the microscope, possible relics of magmatic plagioclase (<1 mm) commonly feature polysynthetic twin lamellae and inclusions of quartz, white mica, clinozoisite and carbonate (Fig. 4.3a-b). Compared to the Zentralgneise (chapter 4.2), plagioclase in the K1-K3 orthogneiss is fresher and less altered. A second recrystallized plagioclase generation (<500 µm) shows evidence for commencing sericitization at its rims and forms together with quartz and potassium feldspar the granoblastic matrix.

Large primary potassium feldspars porphyroclasts (<5 mm) are rare in both varieties (Fig. 4.3c). The porphyroclasts are commonly twinned following the Karlsbader law and feature perthitic exsolutions. Frequently, the primary potassium feldspars show partial transition to the microcline structure at their rims (Fig. 4.3d). Occasionally, replacement of potassium feldspar porphyroclasts by secondary plagioclase, quartz and calcite can be observed. Recrystallized potassium feldspar (<500 µm) occurs within the matrix or replaces primary plagioclase. Potassium feldspar is rare in the aplite gneiss. Recrystallized quartz generally occurs in the granoblastic matrix. In more intense deformed domains, quartz crystals are slightly tabular and elongated. Micas crystallized syn- and post-tectonically. Biotite is in both orthogneiss varieties the only observed mafic mineral and shows a medium-brown to colorless pleochroism under plane polarized light. The grain size of biotite is highly variable; smaller biotite flakes are oriented parallel to the main foliation (<500 µm), while post-tectonically crystallized biotite overgrows the existing foliation and occasionally exceeds a grain size of 1 mm (e.g. sample C-K1d-b, Fig. 4.3e). Zircon inclusions creating pleochroitic halos in biotite are occasionally observed (Fig. 4.3e). Biotite is frequently replaced by chlorite or muscovite. Muscovite is similar to biotite either aligned parallel to the foliation or without particular orientation. In sample K1-31.59 from the light-colored K1-K3 orthogneiss, muscovite (<1 mm) crystallized between the grain boundaries of feldspar and quartz, indicating a network-like fabric (Fig. 4.3f). In the aplite gneiss biotite is generally absent and secondary muscovite occurs subordinately.

Accessory minerals in the K1-K3 orthogneiss are calcite, apatite, zircon, titanite, allanite, epidote, clinozoisite, zoisite, garnet, and scheelite. Calcite was observed in considerable quantities in the majority of the K1-K3 orthogneiss samples either in the strain shadows and cracks of mm- to cm-sized scheelite porphyroclasts (Fig. 4.4a) or disseminated within the matrix. Rare calcite inclusions occur in relict plagioclase (Fig. 4.3a-b). Colorless apatite forms anhedral grains (<150 µm) dispersed in the matrix or crystallized as euhedral prismatic inclusions (10-50 µm) in magmatic allanite and zircon.

Brownish allanite (<200 µm) is common in the dark-colored K1-K3 orthogneiss, though rare in the light-colored variety and is mantled throughout by a corona of epidote-(clino)zoisite (Fig. 4.4b). Similarly, zircon is more abundant in the dark-colored K1-K3 orthogneiss where both colorless and brown (metamict) elongated (<300 µm) prismatic zircons are observed (Fig. 4.4c). Dirty-brown titanite (<2 mm) rarely forms euhedral sphenoidal crystals but usually (re)crystallized as anhedral irregular shaped porous grains with uneven boundaries. Microscopic and EPMA studies revealed minute inclusions of Nb-rutile, scheelite, uraninite, apatite, allanite, muscovite, pyrrhotite, and bismuth sulfide in titanites. Titanite in sample B-K1h is almost completely altered and replaced by rutile, calcite, chlorite, and a Ca-Ti-Nb-REE oxide. Poikiloblastic garnet is restricted to the dark-colored K1-K3 orthogneiss (Fig. 4.4d).

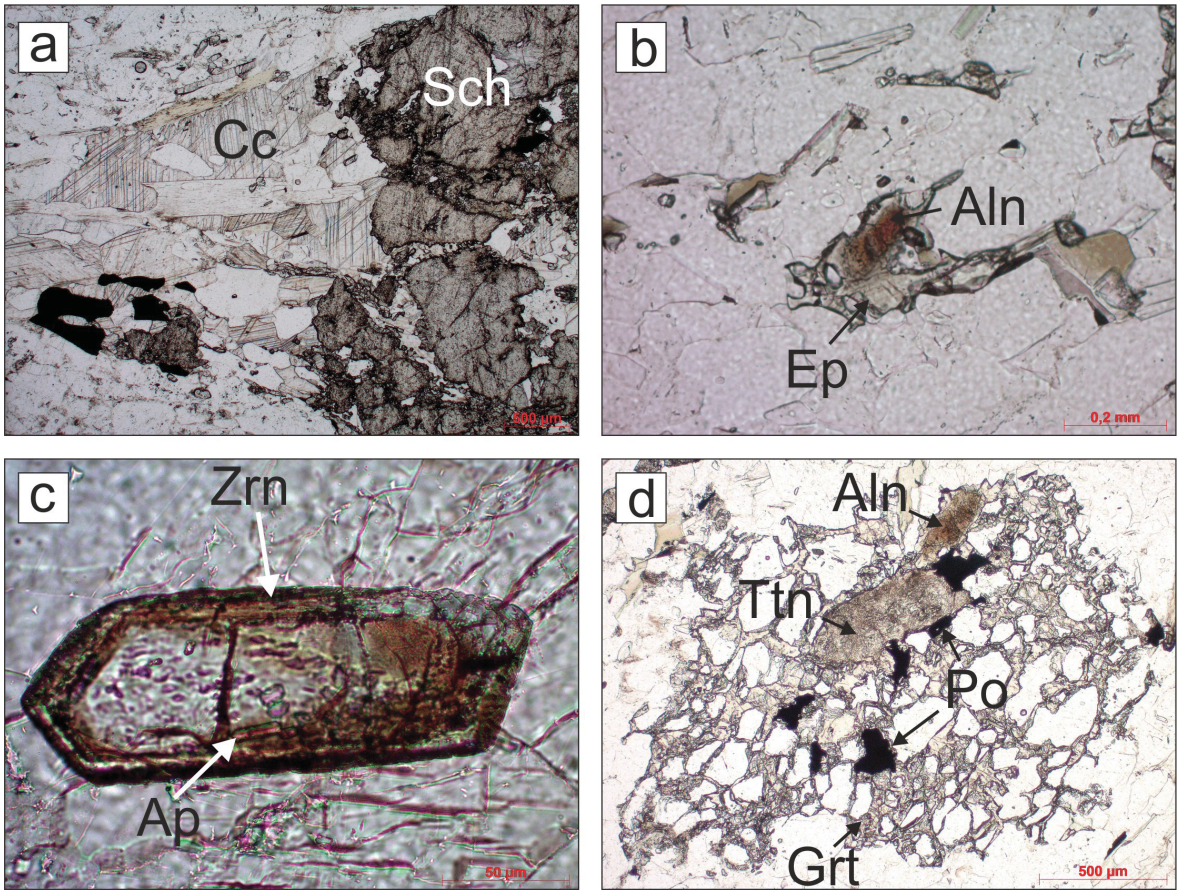

Fig. 4.4 Photomicrographs of accessory minerals in the K1-K3 orthogneiss; plane polarized light. **a)** Scheelite (Sch) porphyroclast with calcite (Cc) in the strain shadow, dark-colored K1-K3 orthogneiss sample Gn-1065b. **b)** Allanite (Aln) mantled by epidote (Ep); dark-colored K1-K3 orthogneiss sample Gn-1065a. **c)** Colorless zircon (Zrn) in the core with brown metamict rim. The small prismatic inclusions are apatite (Ap); light-colored K1-K3 orthogneiss sample B-K1h. **d)** Poikiloblastic garnet (Grt) with allanite (Aln), titanite (Ttn), and opaque pyrrhotite (Po); dark-colored K1-K3 orthogneiss sample K1-48.

Additionally, a diverse assemblage of opaque minerals occurs in the K1-K3 orthogneiss. The most abundant ore mineral is pyrrhotite but also chalcopyrite is very common. Pyrite, molybdenite, arsenopyrite, and galena are subordinate constituents. Oxides were not observed in course of this work. Usually, opaque phases are dispersed in the K1-K3 orthogneiss, though may be concentrated in pods and at vein selvages of mineralized quartz veins (chapter 4.1.7).

The mineralogical differences between the two K1-K3 orthogneiss varieties and the aplite gneiss can be summarized as follows (Tab. 4.1): The dark-colored K1-K3 orthogneiss is characterized by a higher modal abundance of biotite and accessory minerals (allanite, titanite, apatite, zircon, scheelite) as compared to the light-colored variety. Garnet occurs exclusively in the dark-colored variety. In contrast, the quartz- and muscovite contents are higher in the light-colored K1-K3 orthogneiss. Calcite and opaque minerals are disseminated in both varieties throughout. The aplite gneiss is virtually free of mafic minerals; additionally, plagioclase is the pre dominant feldspar and muscovite is abundant. Scheelite is rare in the aplite gneiss.

	Dark-colored K1-K3 orthogneiss	**Light-colored K1-K3 orthogneiss**	**Aplite gneiss**
Quartz	xx	xxx	xx
Plagioclase	xx	xx	xxx
K-feldspar	x	x	o/-
Biotite	xx	o	-
Muscovite	x	xx	xx
Allanite	x	o	o/-
Epidote/ (Clino-)zoisite	x	x	x
Garnet	x	-	-
Titanite	x	o	o
Apatite	xx	x	o/-
Zircon	xx	xx	x
Scheelite	xx	x	o
Calcite	xx	xx	xx
Pyrrhotite	x	x	o
Chalcopyrite	x	x	o/-

xxx very abundant xx abundant x common o rare - absent

Tab. 4.1 Qualitative modal characterization, based on optical microscopy, of the mineral assemblage of the K1-K3 orthogneiss varieties and the aplite gneiss. A quantitative modal analysis is given in Jahoda (1984).

4.1.3 K2 orthogneisses

The K2 orthogneisses belongs to the group of Early Paleozoic gneisses that are associated with the K2 ore body located in the western ore field (Höll and Eichhorn 2000). In previous studies material of the K2 orthogneiss was studied at the higher levels of the underground mine (chapter 2.2.1); however, equivalent rocks were identified during this work in the K2´ ore body on the 800 m and 700 m levels (e.g. sample Gn-800_K2´).

K2 groundmass equivalent

UB-335_55-57

The sample originated from drilling meter 55 to 57 of exploration well UB-335 (level 700 m). Macroscopic description of the drill core reveals a fine-grained dark biotite-albite gneiss with xenolithic fragments of mafic (amphibolitic) material (<1 cm). A striking feature of this sample is the disseminated moderate- to high-grade mineralization. No further microscopic-petrographic investigations were carried out.

Younger K2 orthogneiss

AP-3.82, AP-63.31, Gn-800_K2´, K2-1005b, K2-1005c, UB-336_155-157

In several drill cores (UB-336, UB-343, UB-344), 1-4 m thick dikes of fine-grained leucocratic biotite-poor gneiss with variable amounts of quartz, plagioclase, muscovite, and biotite were intersected. Additionally, a similar orthogneiss was sampled on the levels 1005 m and 800 m. Comparison of the geochemical signature with published data from the K2 orthogneisses (Höll and Eichhorn 2000) revealed an affiliation to the group of *younger* K2 orthogneiss.

Relict magmatic plagioclase porphyroclasts (<3 mm) with minute inclusions of muscovite and clinozoisite rarely occur. When preserved, they occasionally feature polysynthetic twin lamellae and a thin rim of secondary inclusion-free plagioclase. Syn- to post-tectonic biotite is unaltered, showing brown-orange colors in plane polarized light. Prismatic zoisite (100-500 µm) is abundant and frequently associated with micas parallel the foliation of the rock. Accessory minerals are titanite, allanite, clinozoisite, calcite, scheelite, garnet, zircon, and tourmaline. Garnet (<200 µm) forms euhedral crystals and occurs frequently in the presence of biotite. Rarely, larger crystals (<1 mm) are observed; however if present they commonly feature a zoning pattern with a dark rim-domain in plane polarized light. Scheelite is mainly restricted to quartz veinlets crosscutting the gneisses but also occurs disseminated.

Pyrrhotite is the dominant opaque mineral in the younger K2 gneiss; chalcopyrite and molybdenite are very rare. Large pyrrhotite (<2 mm) is concentrated in sample Gn-800_K2´ within a 3-5 mm thick domain (Fig. 4.5a) commonly with abundant zoisite, biotite and rare tourmaline. The latter appears exclusively in this zoisite-rich domain (Fig. 4.5b). Additionally, pyrrhotite and chalcopyrite crystallized in cracks of zoned garnets.

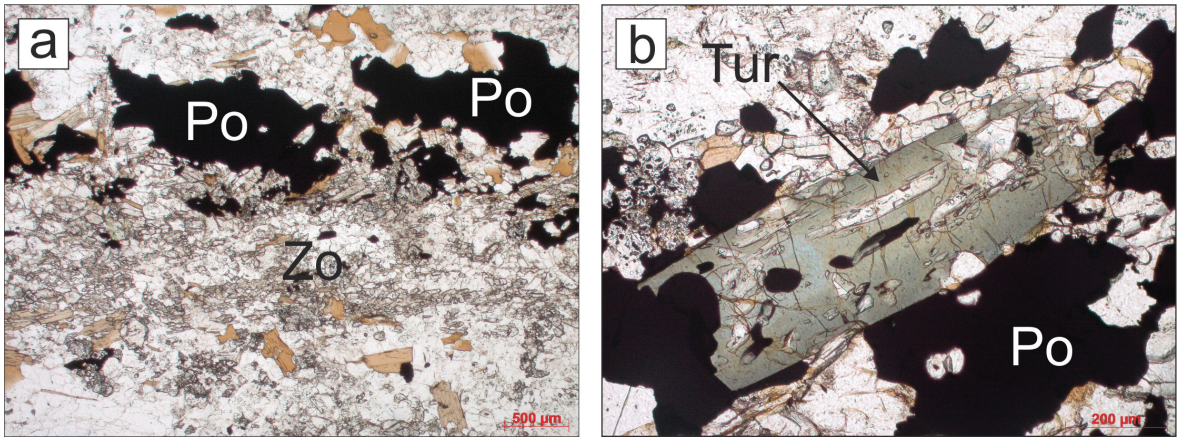

Fig. 4.5 Photomicrographs of sample Gn-800_K2´ in plane polarized light. **a)** 3-5 mm thick domain rich in zoisite (Zo) and large pyrrhotite (Po). **b)** Tourmaline (Tur) associated with pyrrhotite (Po).

4.1.4 Quartz-diorite gneiss

Gn-736-1, Gn-736-2, Gn-795, Gn-940, Gn-940K2´, Gn-1038a, Gn-1262

Fine- to medium-grained, poorly mineralized, mesocratic biotite-albite gneiss was sampled on the 736 m, 795 m, 940 m, 1038 m, and 1262 m levels of the underground mine. The gneiss occurs as up to one meter thick dikes concordant to the main foliation of the wall rocks (Fig. 4.6a). The mineral assemblage of the quartz-diorite gneiss is characterized by pale-brown biotite, albite, quartz, prismatic zoisite and subordinate amounts of anhedral to euhedral titanite, apatite, calcite, amphibole, and euhedral garnet. Relict plagioclase features minute muscovite and clinozoisite inclusions. Biotite in sample Gn-1262 crystallized syn- to post-tectonically and displays a gradual transition from fresh, dark brown biotite to chloritized biotite and finally to chlorite. Quartz is aligned in lenticular clusters and shows significant evidence of recrystallization. Zoisite is common and forms prismatic crystals parallel to the foliation of the rock. Scheelite is rare in most samples or even absent (Gn-1262 and Gn-795).

4.1.5 Fine-grained amphibolite

K2-1005M, SE-1038a

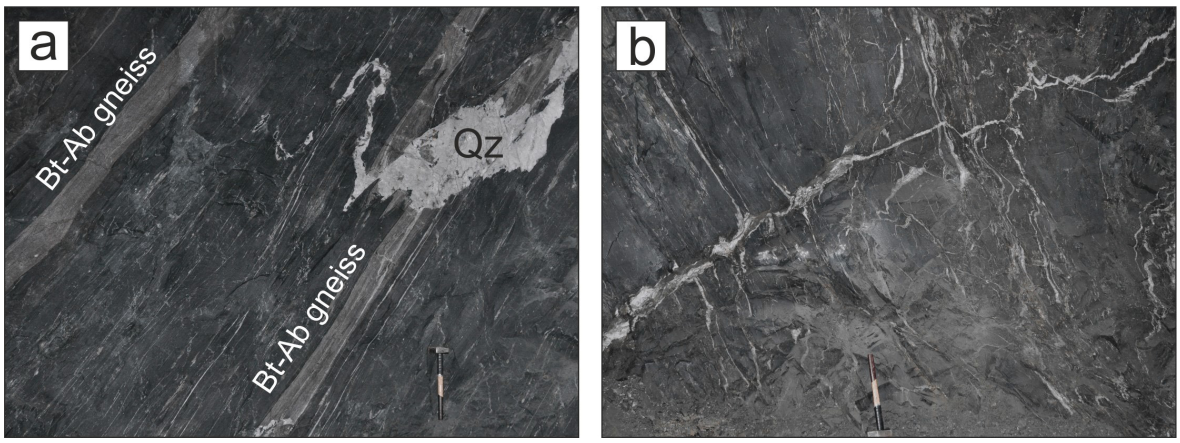

Fig. 4.6 Photographs of intermediate to mafic lithologies in the western ore field. **a)** Dikes of quartz-diorite gneiss (Bt-Ab gneiss). Late Alpine metamorphic and tectonic overprint caused displacement of the dike and formation of Alpine quartz veins (Qz); level 940 m. **b)** Fine-grained chlorite-biotite amphibolite with network of crosscutting quartz veins (referred to as “Schwarzerz”); level 1038 m.

Höll (1975), Jahoda (1984) and von Quadt (1985) distinguished a variety of mafic lithologies within the LMS in the Felbertal tungsten deposit. These mainly comprise polymetamorphic amphibole-, chlorite-, and plagioclase-bearing (ultra-)basic rocks, which are usually distinguished according to their petrographic description and modal mineral abundances. In course of this project two samples of fine-grained chlorite-biotite-amphibolite (“Prasinit”) associated with the K2 ore body on the levels 1038 m and 1005 m were taken for mineral chemical studies. Both samples feature quartz-scheelite veins. In the case of sample K2-1005M, cm thick quartz-scheelite veins crosscut the amphibolite parallel to the main foliation. On the contrary, sample SE-1038a was taken from a fine-grained amphibolite, known as “Schwarzerz” in the mine, featuring a network of mm- to cm-thick quartz-scheelite veins crosscutting the rock more or less discordantly (Fig. 4.6b). The schistosity of the amphibolites is well pronounced with green pleochroitic amphibole in close association with chlorite and prismatic zoisite aligned parallel to the foliation. Unaltered large orange-brown biotite (<1 mm) overgrows the main foliation, indicating its post-tectonic growth; however smaller biotite flakes (<500 µm) occur aligned with chlorite and hornblende parallel to the foliation. Plagioclase porphyroclasts (<3 mm) commonly feature muscovite- and clinozoisite-rich cores and inclusion-free rims. Calcite is a common accessory mineral in addition to scheelite, titanite, garnet, clinozoisite, and epidote. Pyrrhotite, chalcopyrite and molybdenite are the usual opaque minerals observed under the microscope.

4.1.6 Laminated scheelite-quartz ore and gneiss

FT-74, FS-1

Both samples were not collected in course of this study but are from archive material of previous projects. The sample FT-74 is a laminated scheelite-quartz ore from the former open pit mine in the eastern ore field. In the past this ore type has been described as scheelite-rich quartzite ("Scheelitreicherz"; Höll 1975). Scheelite is very fine-grained (<0.4 mm) and strongly aligned, causing a prominent foliation in this high-grade ore. Saccharoidal quartz, the major mineral, is completely recrystallized. In contrast, scheelite shows incomplete recrystallization. Stringers of very fine-grained scheelite aggregates are composed of elongated porphyroclasts of yellow-white fluorescent scheelite (Scheelite 1) with recrystallized blue-fluorescent scheelite material (Scheelite 3) at its rims. The Scheelite 1 relicts preserve fine oscillatory growth zoning, best to be seen under cathodoluminescence (Fig. 2.2a). White mica occurs as an accessory mineral.

Additionally, a leucocratic, laminated, scheelite-rich gneiss comes from the eastern ore field (sample FS-1). FS-1 differs from the laminated scheelite-quartz ore in that it contains more plagioclase, muscovite, epidote, apatite and zircon but less quartz than sample FT-74. However, FS-1 also has a high content of fine-grained Scheelite 1.

4.1.7 Macro- and microscopic vein types

A prominent feature of numerous studied samples is the occurrence of various vein types (Fig. 4.7) reflecting the distinct magmatic-hydrothermal and/or polymetamorphic overprint that affected the Felbertal scheelite deposit. These veins are either present as macroscopic structures easily identifiable (e.g. quartz-scheelite vein) or as structures only visible under the microscope (e.g. potassium feldspar veinlets). Some vein-types are clearly related to the ore-forming processes such as the quartz-scheelite veins and some correspond probably with the metamorphic overprint that affected the ores (e.g. potassium feldspar veins). Consequently, it is important to consider the various vein types in greater detail for a better understanding of the genetic evolution of the Felbertal scheelite deposit and the processes which are responsible for W mineralization and its possible dispersion/mobilization.

All vein types were also observed in the K1-K3 orthogneiss and in related quartz-scheelite veins, by what a maximum Early Carboniferous formation age for the various veins is constrained.

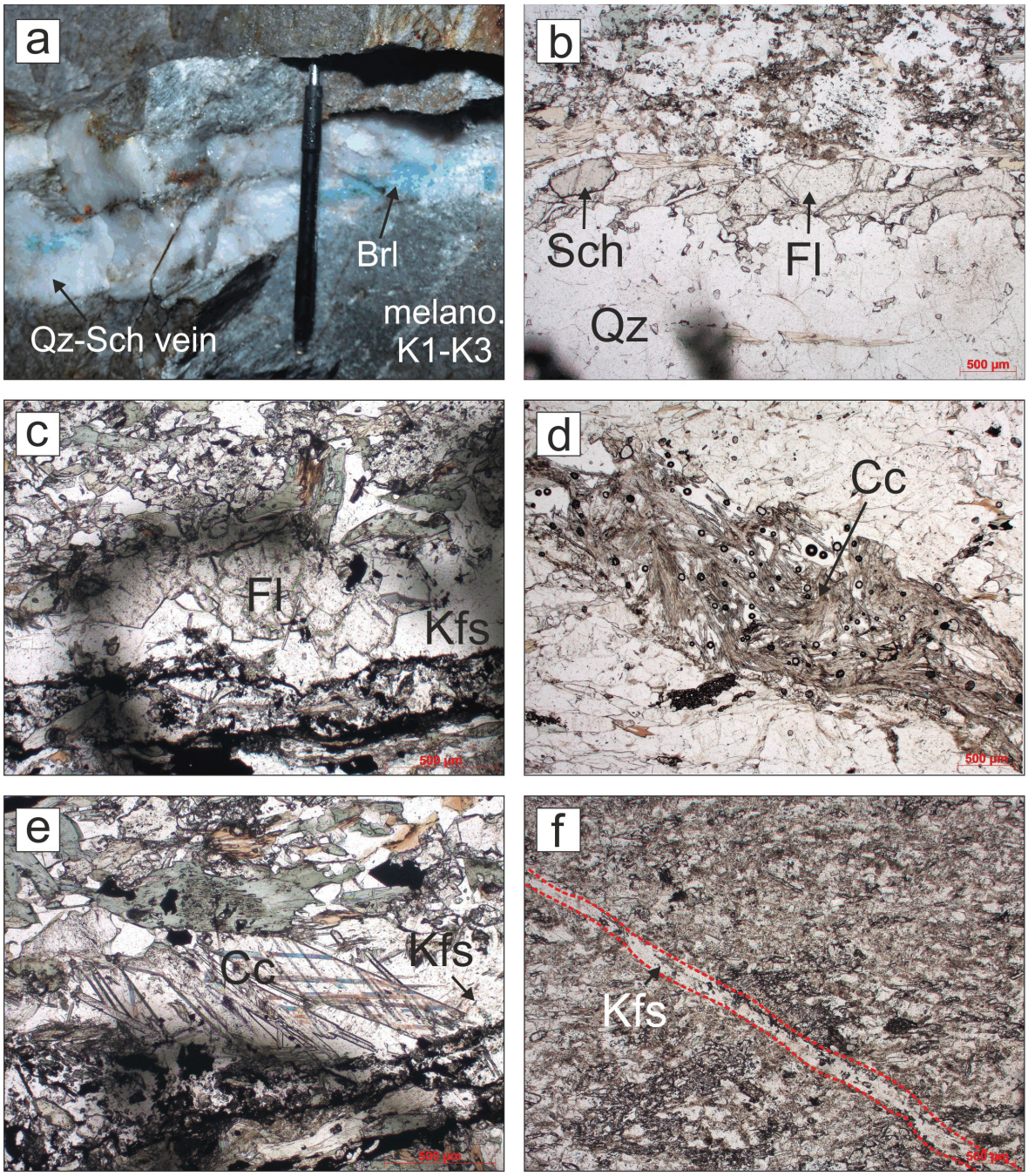

Fig. 4.7 Various vein types observed in the western ore field. **a)** A cm-thick quartz-scheelite (Qz-Sch) vein (Quartz1) crosscutting the dark-colored K1-K3 orthogneiss containing blue beryl (Brl); level 1164 m. **b)** Fluorite (Fl) veinlet associated with scheelite (Sch) parallel to the foliation in a quartz-diorite gneiss; plane polarized light, sample Gn-1038a. **c)** Sub- to euhedral fluorite (Fl) in a potassium feldspar (Kfs) filled crack; plane polarized light, sample SE-1038a. **d)** Fracture with bladed calcite (Cc) discordantly crosscutting the dark-colored K1-K3 orthogneiss; plane polarized light, sample K1-23.29. **e)** Remobilized bladed calcite (Cc) in the same potassium feldspar vein (Kfs) shown in Fig. 4.7c; plane polarized light, sample SE-1038a. **f)** A 500 µm-thick potassium feldspar veinlet discordantly crosscutting the younger K2 orthogneiss which shows pervasive sericitization of adjacent plagioclase; plane polarized light, sample AP-3.82.

Quartz-scheelite veins

A-K1q-b, A-K1q-c, B-K1q-a, B-K1q-b

Quartz-scheelite veins crosscut both Early Paleozoic host rocks as well as Variscan orthogneisses in the western ore field where these veins represent the major ore type. In the mine these scheelite-rich quartz veins are termed “Quartz 1” veins. The veins are often aligned to the foliation of the host rocks and show evidence of ductile deformation (Raith and Schmidt 2010). Two quartz-scheelite veins were sampled on the 1164 m level, from which two thin sections were prepared. The mineral assemblage of the veins includes quartz, scheelite and minor to accessory muscovite, epidote, clinozoisite, zoisite, calcite, fluorite, phenakite, beryl, titanite, (Y,REE,U,Th)-(Nb,Ta,Ti) oxide minerals, pyrrhotite, molybdenite, pyrite, and chalcopyrite. Moreover, a variety of rare Pb-Bi-sulfosalts has been reported from these quartz veins (Topa et al. 2002 and references therein).

The beryl variety aquamarine is very common in quartz-scheelite veins and can be easily identified by its blue color (Fig. 4.7a). Beryl is associated with the colorless Be-silicate phenakite, scheelite, calcite, muscovite, and fluorite and occurs as poikiloblastic crystals with inclusions of phenakite or replaces cm-large phenakite porphyroclasts (Franz et al. 1986).

Discrete (Y,REE,U,Th)-(Nb,Ta,Ti) oxide minerals (<200 µm) were observed in the W-deposit only in quartz-scheelite vein sample A-K1q-c. Petrographic studies reveal a zoning pattern with dark-brown cores and orange-brown rims in plane polarized light. Reflected light microscopy revealed cracks in the Nb-Ta phases that are filled with bismuthinite and native bismuth. Minute scheelite and fluorite inclusions were detected in the cores of the oxide minerals during microprobe studies (chapter 5.2.4).

Fluorite veinlets (± calcite)

Fluorite is a common but frequently overlooked accessory mineral in the ores as known from the ore processing (flotation) and occurs either as small rims around scheelite porphyroclasts (e.g. Gn-1038a; chapter 5.3.1) or as veinlets and lenses (<1 mm) parallel to the foliation of the rocks (Fig. 4.7b). Occasionally, Scheelite 2 and 3 are associated with fluorite (Fig. 4.7b). Additionally, fluorite is frequently accompanied by calcite within the veins. Samples in which fluorite veins were observed are Gn-1038a (quartz-diorite gneiss) and the dark-colored K1-K3 orthogneiss samples Gn-1065a and K1-23.29. Fluorite in the amphibolite sample SE-1038a is remarkable, as it was observed as euhedral cleft-crystals

grown in a feldspar-filled crack (Fig. 4.7c). Consequently, fluorite-precipitation is preceding the highly aluminous alteration assemblage (see feldspar veins).

Calcite veins

Calcite was observed in all thin sections as inclusions in plagioclase, in the granoblastic matrix or in the strain shadow of scheelite porphyroclasts. Distinct unmineralized veinlets in which calcite crystallized where recognized only in samples K1-23.29 (dark-colored K1-K3 orthogneiss), Gn-1262 (quartz-diorite gneiss) and SE-1038a (amphibolite). The difference of the vein calcite to the matrix calcite is the habitus of the crystals. Matrix calcite is usually of rhombohedral shape while vein calcite features a bladed habitus (Fig. 4.7d) which is characteristic for crystallization from boiling fluids as the result of CO_2-loss to the vapor phase during boiling (Simmons and Christenson 1994). In samples Gn-1262 and K1-23.29 the respective calcite vein discordantly crosscuts the main foliation. Calcite in sample SE-1038a is different to the other samples in that calcite crystallized in a rhombic shape within the vein which is then again crosscut by a feldspar vein. At the intersection, calcite was remobilized and crystallized in the bladed form (Fig. 4.7e).

Potassium feldspar veins

A highly potassic alteration assemblage in form of potassium feldspar veinlets was observed in samples AP-3.82 (younger K2 orthogneiss), B-K1q-a (quartz-scheelite vein) and SE-1038a (amphibolite). AP-3.82 shows evidence of potassic alteration in form of a network of thin (< 200 µm) potassium feldspar veinlets. Where these small veins crosscut the gneiss, plagioclase is altered to sericite (Fig. 4.7f). Zoisite crystallized at the edges of the veinlets as shown in figure 4.7f. As described in the previous chapter, the potassium feldspar veinlets in sample SE-1038a crosscuts a calcite veinlet where it remobilizes calcite. Additionally, the veinlet contains molybdenite at its selvages.

4.2 Zentralgneise

4.2.1 Introduction

Field work in the central Tauern Window was done during the summer months in 2012 and 2013 with the objective to sample the Zentralgneise occurring in the vicinity of the Felbertal W-deposit. The purpose was to study petrographic, mineralogical and geochemical features of the barren Zentralgneise and to compare them with the W mineralized K1-K3 orthogneiss. This part of the study aimed for identifying a potential parental granitoid from which the K1-K3 orthogneiss was derived and clarifying the petrogenetic evolution of the scheelite-bearing orthogneiss in the course of Variscan magmatism.

For comparative purposes samples were taken from several Early Carboniferous orthogneisses including the Felbertauern augengneiss (340 ± 4 Ma, Eichhorn et al. 2000), Knorrkogel gneiss (334 ± 8 Ma, Finger and von Quadt 1993), and Hochweißenfeld gneiss (342 ± 5 Ma, Eichhorn et al. 2000). The Zentralgneise of supposed Late Carboniferous to Permian age were additionally considered. This group comprises the Weißeneck-Dichtensee gneiss which is interpreted as the eastern extension of the Venediger pluton (296 ± 4 Ma, Eichhorn et al. 2000) and the Granatspitz gneiss. For the latter Eichhorn et al. (2000) suggested a Permian intrusive age (271 ± 4 Ma), whereas Kebede et al. (2005) proposed a Late Carboniferous age (314 ± 4 Ma). Because of reported small scheelite showings in aplites near the historical Pb-Zn-F district Achselalm-Flecktruhalm (Kwasnitschka 1983), a poorly mineralized aplite was sampled from the respective locality.

Altogether, 42 samples of Zentralgneise and related rocks from the central Tauern Window were taken and investigated. Sample localities are shown on Figure 4.8; for exact GPS-coordinates refer to Appendix C.

Fig. 4.8 ÖK 50 maps 3220 and 3226 with sample localities and sample numbers of studied Zentralgneise (©BEV – Bundesamt für Eich- und Vermessungswesen).

4.2.2 Felbertauern augengneiss

SP-07/30, FB-12/30, SP-25/34, SP-26/34, SP-27/34, SP-28/34, SP-29/34, SP-30/34, SP-31/34, FB-33/34, FB-48/39

The Felbertauern augengneiss (Cornelius 1942a; Frasl 1955; Fuchs 1958) probably occurs at the basis of the Zillertal-Riffl Nappe as a several km-long, N-S striking, sill-like gneiss body (Fig. 2.1). The strongly deformed gneiss sheet, showing tectonic contacts to its foot- and hanging wall (Pestal and Hejl 2005) can be traced from an elevation of 1700 m atop the western ore field south towards the St. Pöltner Hütte (2481 m). Several hundred meters thick outcrops of the Felbertauern augengneiss are also exposed to the southwest of the Granatspitz gneiss core.

The Felbertauern augengneiss is a medium- to coarse-grained, strongly foliated (mylonitic), leucocratic orthogneiss, characterized by deformed and elongated whitish-grey feldspar augen (<1 cm, Fig. 4.9a) and quartz-lenses (<10 cm, Fig. 4.9b). The matrix consists of quartz, plagioclase and partly chloritized biotite; quartz always shows evidence of dynamic recrystallization. Common accessory phases are calcite, muscovite, chlorite, allanite, epidote, (clino-) zoisite, apatite, titanite and zircon. Scarce scheelite mineralization was found in sample SP-25/34. Based on the feldspar habitus, Frasl (1955) proposed an intrusive nature of the Felbertauern augengneiss; the occurrence of meter-thick amphibolite xenoliths within the metagranitoid corroborates its intrusive nature.

Under the microscope, two generations of K-feldspar can be distinguished. The primary magmatic potassium feldspar porphyroclasts (Kfs I), characterized by exsolutions of perthitic plagioclase are frequently twinned after the Karlsbader law. Less common are plagioclase (Pl I) porphyroclasts (<1 cm) with abundant inclusions of muscovite and clinozoisite (Fig. 4.9c). Myrmekitic intergrowth of quartz and plagioclase may occur at the rims of the feldspar phenocrysts. A second generation of K-feldspar (Kfs II) either partly replaced primary magmatic plagioclase or recrystallized in the matrix, forming anhedral grains (<1 mm). Kfs II is free of perthitic exsolutions and commonly shows the tartan twinning of microcline. A secondary plagioclase generation (Pl II) recrystallized as subhedral grains (<0.5 mm). Contrary to Pl I, muscovite and clinozoisite inclusions are absent in Pl II. Both plagioclase generations are commonly sericitized (Fig. 4.9c). Quartz commonly dynamically recrystallized (subgrain rotation recrystallization). Fresh biotite shows a light brown color but is usually partly chloritized at the rims. Chlorite is common in the most fissured portions of the Felbertauern augengneiss where the gneiss appears slightly greenish (e.g. sample locality SP-29/34).

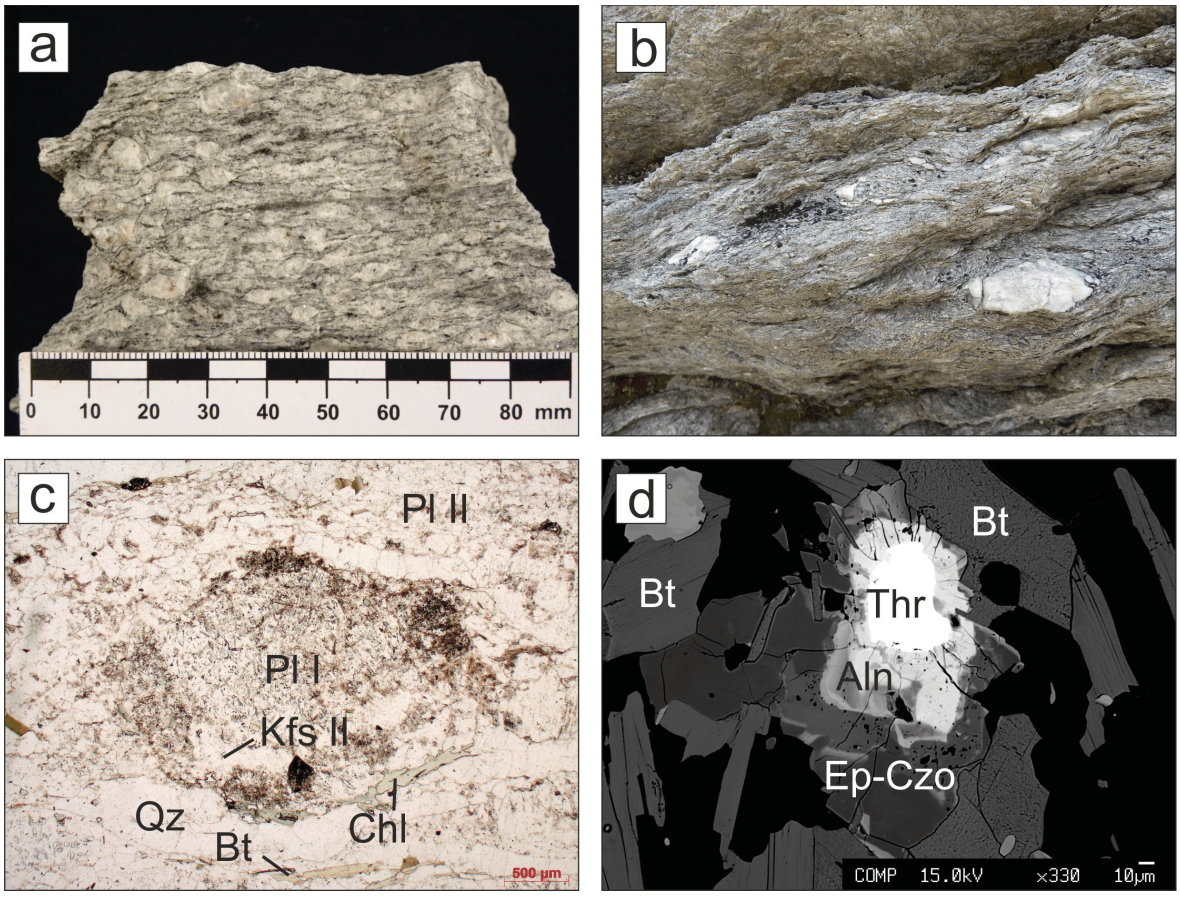

Fig. 4.9 Photographs of the Felbertauern augengneiss. **a)** Sample SP-30/34 with whitish-grey feldspar porphyroclasts (<1 cm) creating an augen texture; quartz, feldspar and micas occur in the matrix. **b)** Mylonitic Felbertauern augengneiss with c. 10 cm large elongated quartz lenses at hiking trail between Plattachsee and St. Pöltner Hütte. **c)** Photomicrograph of a magmatic plagioclase porpyhroclast (Pl I) with muscovite and clinozoisite inclusions that is partly replaced by secondary potassium feldspar (Kfs II); plane polarized light, Qz = quartz, Bt = biotite, Chl = chlorite. **d)** BSE-image of metamict allanite (Aln) with thorite inclusion (Thr) mantled by an epidote-clinozoisite rim (Ep-Czo). Anastomosing cracks emanating from the thorite into adjacent minerals are indicative of volume increase due to metamictization and hydration.

Brownish-red allanite forms elongated prismatic crystals (<500 µm) that are mantled by a corona of epidote-clinozoisite and zoisite throughout. Allanite is commonly metamict as a result of minute inclusions of thorite and uraninite. Hydration and metamictization accompanied with volume expansion of the thorite inclusion caused formation of anastomosing cracks radiating into the adjacent minerals (cf. Zacek et al. 2009, Fig 4.9d). Primary titanite forms euhedral sphenoidal crystals (<500 µm) with inclusions of apatite or zircon; zoning is evident under crossed polarizer. However, a secondary generation of titanite can be identified by its anhedral shape, high porosity and the lack of any zoning. Apatite crystallized as small anhedral grains (50-100 µm) in the matrix, whereas apatite inclusions in magmatic minerals (titanite, zircon, allanite) display euhedral prismatic

habitus. Calcite occurs either in thin veinlets or disseminated in the recrystallized quartz-feldspar matrix. Fuchsite was observed in the hand-specimen of sample FB-48/39.

4.2.3 Knorrkogel gneiss

FB-09/30, IG-20/34, IG-21/34, IG-22/34, IG-23/34, IG-24/34, FB-36/37, FB-37/37, FB-38/37, FB-39/37

The Knorrkogel gneiss (Cornelius 1942b) is restricted to the southern parts of the central Tauern Window where it occurs, similar to the Felbertauern augengneiss, as a several hundred m thick W-E striking gneiss sheet that can be traced over ~22 km from the southern Venediger group eastwards to the southern Granatspitz group (north of Kals am Großglockner; Fig. 2.1). In the eastern parts of the central Tauern Window an equivalent orthogneiss type is described as Luckenkogel gneiss (Benedict 1952).

Continuous transition of the orthogneiss into its respective host rocks (e.g. biotite-plagioclase gneiss, white-mica gneiss) and the lack of intrusive contacts suggest a petrogenetic evolution of the Knorrkogel gneiss by crustal anatexis similar to the Hochweißenfeld gneiss (Schermaier 1993). The genetic correlation of both orthogneisses was first proposed by Cornelius (1942b) who mentioned a gradual transition of the Hochweißenfeld gneiss (footwall) into the Knorrkogel gneiss (hanging wall) with additional anatectic and migmatitic transitional stages at the hiking trail to Löbbentörl (cf. sample locality IG-21/34). However, Fuchs (1958) postulated an intrusive origin for the Knorrkogel gneiss (“Schmelzflussgranit”) based on the potassium feldspar habitus and the absence of migmatites; migmatitic material was also not observed in course of this work.

The Knorrkogel gneiss appears to be heterogeneous in its texture and optical appearance. In general the Knorrkogel gneiss represents a deformed pale-grey fine- to medium grained two-mica orthogneiss with potassium feldspar porphyroclasts <3 cm (Schermaier 1993). The partly idiomorphic porphyroclasts were interpreted as magmatic relicts (Frasl 1955; Fuchs 1958). The grain-size distribution and degree of tectonic deformation of the Knorrkogel gneiss varies significantly in the area Löbbentörl – Innerer Knorrkogel – Wildenkogel (see Fig.4.10a-c).

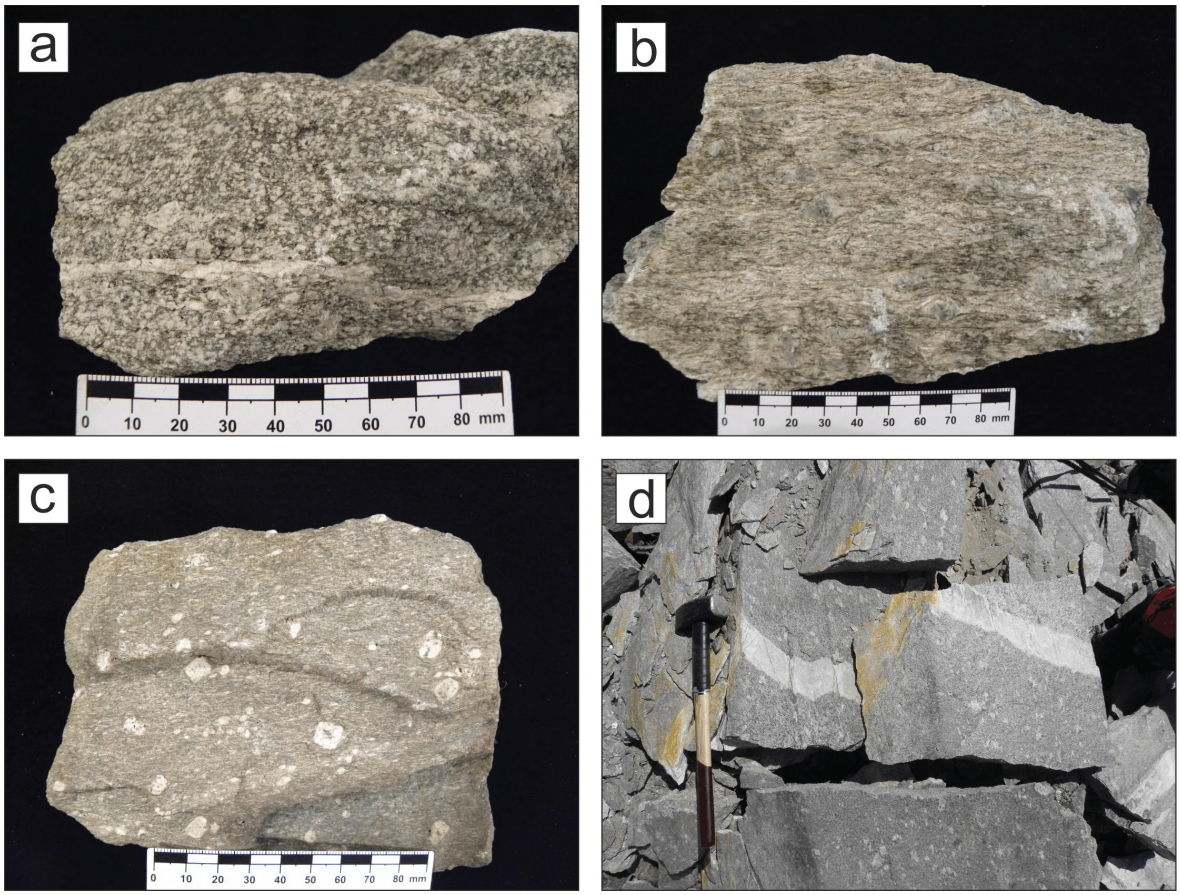

Fig. 4.10 Photographs of the Knorrkogel gneiss. **a)** A weakly foliated medium-grained biotite-plagioclase gneiss with whitish-grey feldspars (<3 mm) and few isolated feldspar porphyroclasts (<0.8 mm); sample IG-23/34. **b)** Feldspar porphyroclasts (<1.5 cm) are whitish-grey with blueish-grey cores; sample FB-39/37. **c)** Foliated, fine-grained porphyritic orthogneiss with feldspar porphyroclasts (<1 cm); sample IG-24/34. **d)** Scree near locality Löbbentörl with fresh Knorrkogel gneiss boulders crosscut by a leucocratic dm-thick aplitic dike.

A medium-grained biotite-plagioclase variety (Fig. 4.10a) is virtually free of phenocrysts (sample IG-23/34 near contact to Hochweißenfeld gneiss, Löbbentörl). The white-grey tabular feldspars occurring in a fine-grained biotite-rich matrix are slightly deformed. In the area near Wildenkogel (e.g. sample FB-39/37, Fig. 4.10b) the Knorrkogel gneiss is characterized by elongated and more deformed whitish-grey to blueish feldspar porphyroclasts (<1.5 cm) occurring in a fine-to medium grained matrix consisting of muscovite, biotite, feldspar, and quartz. There is more muscovite in this variety of the Knorrkogel gneiss as compared to the biotite-plagioclase gneiss. Additionally, a fine-grained, strongly foliated, porphyritic gneiss/schist can be distinguished with characteristic larger feldspar crystals (<1 cm, sample IG-24/34, Fig. 4.10c) embedded in a mica-rich matrix.

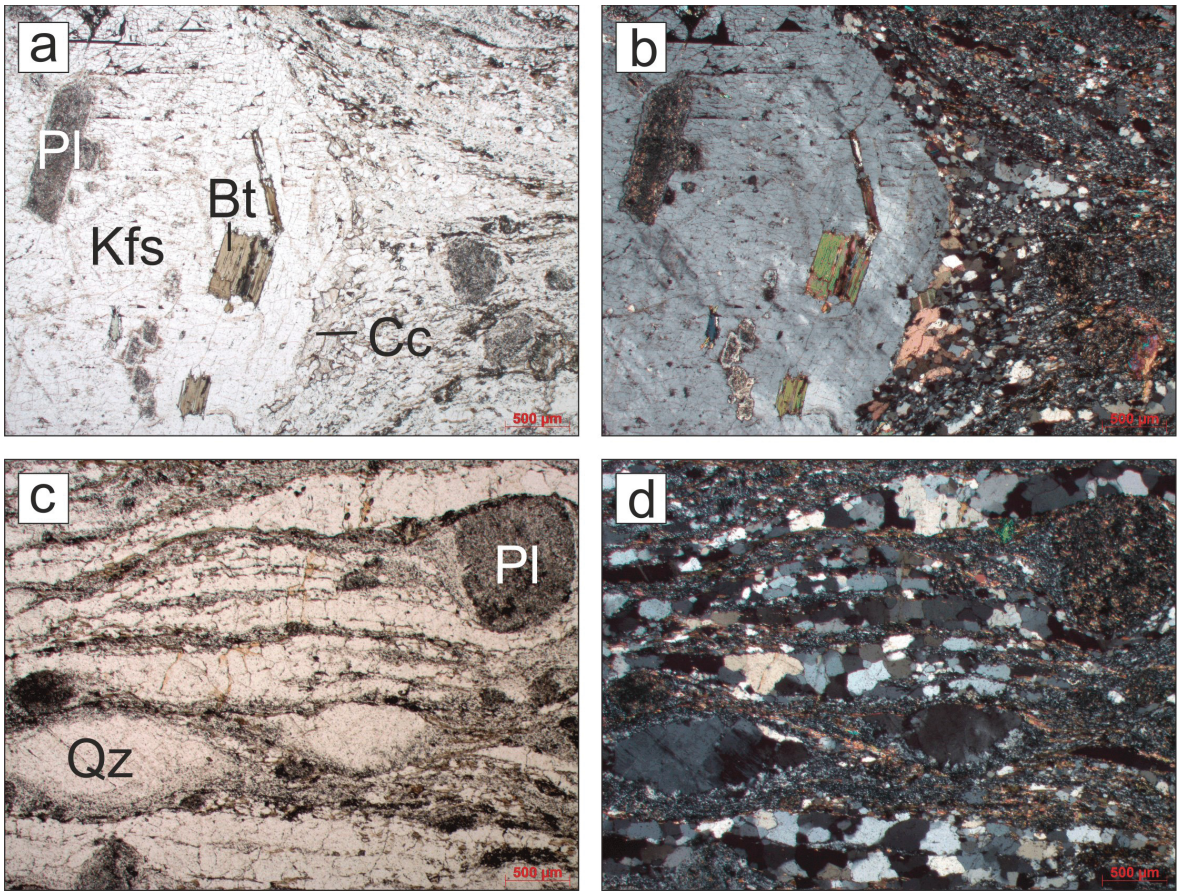

Fig. 4.11 Knorrkogel gneiss sample FB-37/37 under the microscope. **a)** Potassium feldspar porphyroclast (Kfs) with oriented biotite (Bt) and plagioclase (Pl) inclusions in a fine grained matrix, plane polarized light. **b)** Calcite (Cc) in the strain shadow of the recrystallized feldspar porphyroclasts; cross polarized light. **c-d)** Quartz (Qz) in a very fine-grained matrix of quartz, feldspars and micas. Plagioclase is decomposed to clinozoisite and white mica; plane polarized light, bulging and subgrain rotation are the dominant recrystallization processes in quartz; cross polarized light.

The latter sample was taken in the direct vicinity to sample IG-23/34 (biotite-plagioclase gneiss). Occasionally, the Knorrkogel gneiss is crosscut by both concordant and discordant aplitic dikes (Fig 4.10d).

Biotite, tabular plagioclase and allanite are common inclusions in the potassium feldspar porphyroclasts; they are oriented subparallel to the c-axis of the host potassium feldspar (Fig. 4.11a). The K-feldspar rarely shows perthitic exsolution. Frequently, calcite crystallized in the strain shadows of the porphyroclasts (Fig. 4.11b). Plagioclase, occurring as inclusion in potassium feldspar (<1 mm) and in the matrix (<5 mm), shows generally intense alteration to clinozoisite and white mica. Occasionally, plagioclase replaces potassium feldspar. Fresh biotite inclusions in feldspars are of pale-brown color and are partly replaced by muscovite. Matrix biotite is often completely replaced by muscovite.

Quartz dynamically recrystallized as indicated by bulging and subgrain rotation recrystallization giving the rock a prominent tectonic fabric (Fig. 4.11c-d). Common accessory minerals are euhedral allanite and titanite, subhedral apatite and subordinate epidote, clinozoisite, and zircon.

4.2.4 Hochweißenfeld gneiss

FB-10/30, FB-11/30L, FB-11/30M, IG-15/34, IG-16/34, IG-17/34, IG-18/34, IG-19/34, FB-34/37, FB-35/37

The Hochweißenfeld gneiss (Cornelius and Clar 1939) occurs as isolated lenses south of Kitzsteinhorn (Kapruntal), while the largest continuous gneiss body can be traced from southern Hollersbachtal ca. 16 km southeast to Tauerntal (Landeggalm, Fig. 2.1).

The Hochweißenfeld gneiss is a medium- to coarse-grained metagranitoid located within an aureole of metatectic and diatectic gneisses and amphibolites (Finger et al. 1993). Similar to the Knorrkogel gneiss, no clear boundary of the orthogneiss to its country rocks can be drawn (Schermaier 1991, 1993; Finger et al. 1993). An inhomogeneous appearance is characteristic for the Hochweißenfeld gneiss. Domains of stromatic migmatitic schlieren (Fig. 4.12a) with mm- to cm-thick layers of light leucosomes and dark biotite-rich melanosomes alternate with potassium feldspar-porphyritic biotite-rich orthogneisses and fine-grained dark biotite-schists and biotite-plagioclase gneisses (Fig. 4.12b). Occasionally, the boundaries between dark biotite-rich migmatitic lithologies and the leucocratic orthogneiss are obliterated, creating a nebulous migmatitic texture in the Hochweißenfeld gneiss (Fig. 4.12c). Small elongated cm- to dm-thick enclaves of biotite-plagioclase gneiss with partially molten mm-thick fine-grained biotite-rich rims occur within the leucocratic orthogneisses (Fig. 4.12d). Additionally, up to several meters thick amphibolite xenoliths exhibiting migmatitic transition into the Hochweißenfeld gneiss are common. According to field observations, the Hochweißenfeld gneiss is regarded as an in-situ formed anatectic melt generated at deep-crustal levels (Schermaier 1991, 1993; Finger et al. 1993).

A further characteristic feature of the Hochweißenfeld gneiss is the occurrence of dm- to m-thick pegmatites with blueish-grey potassium feldspar porphyroclasts (<2 cm). The dikes are oriented both concordant and discordant to the prominent foliation of the gneiss and crosscut the anatectic domains of the Hochweißenfeld gneiss (Schermaier 1991).

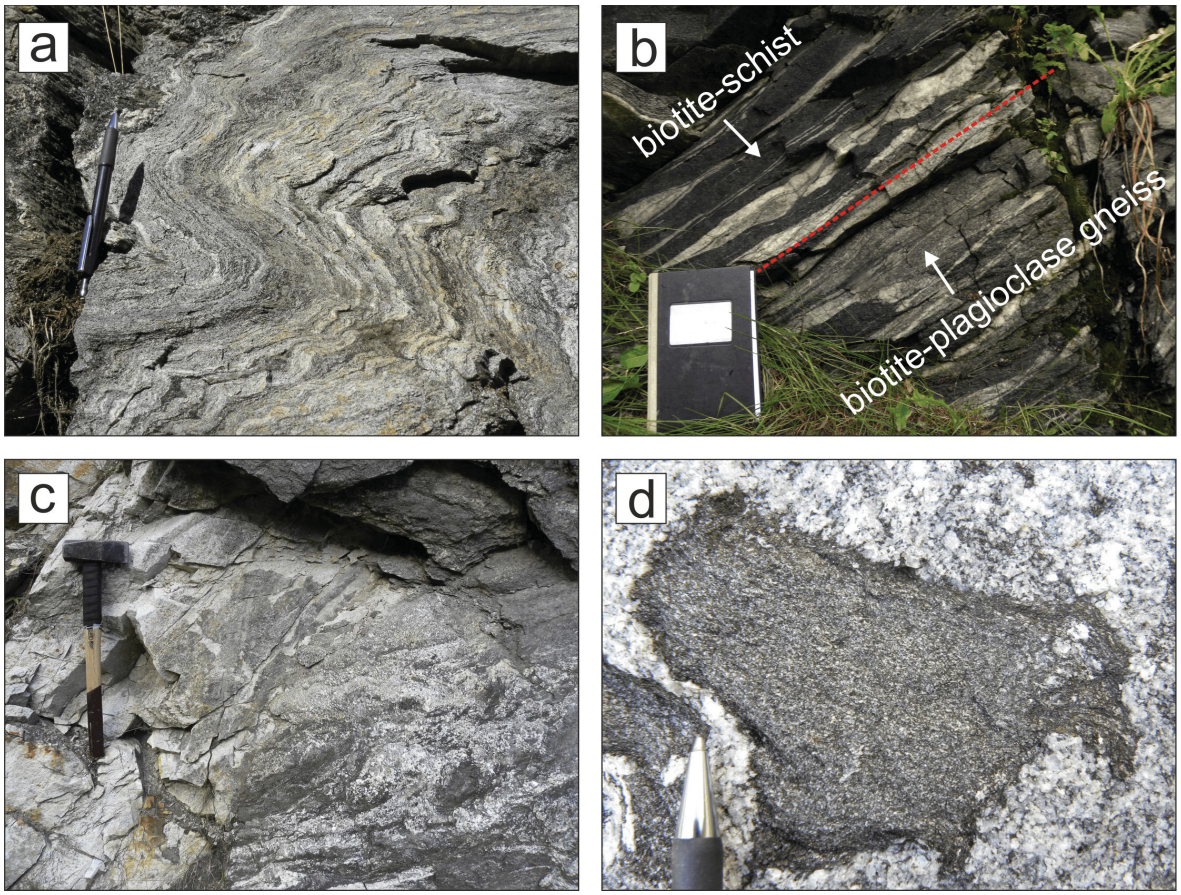

Fig. 4.12 Photographs of the inhomogeneous Hochweißenfeld gneiss along the Felbertauern road B 108. **a)** Folded stromatic migmatite with alternating mm- to cm-thick layers of light leucosomes and dark melanosomes; sample locality FB-35/37. **b)** Alternating layers of foliated dark biotite-schist and dark-grey biotite-plagioclase gneiss (separated by the red dashed line). Leucocratic feldspar-rich orthogneiss showing pinch and swell structures occurs in both lithologies; book height is 21 cm, sample locality FB-11/30. **c)** Hochweißenfeld gneiss grading into migmatic rocks creating a cloudy texture; sample locality FB-35/37. **d)** A cm-thick enclave of biotite-plagioclase gneiss with biotite-rich rim in a medium-grained feldspar-rich orthogneiss; sample locality FB-35/37.

Under the microscope, potassium feldspar occasionally shows perthitic exsolutions and contains inclusions of plagioclase, oriented parallel to the c-axis of the feldspar. Myrmekitic intergrowth of quartz and plagioclase at the rim of the potassium feldspars is common. Plagioclase (Pl I) crystallized both as isolated phenocrysts (<5 mm) or recrystallized in the matrix of the orthogneiss (Pl II). Similar to the Felbertauern augengneiss, the Pl I phenocrysts are characterized by polysynthetic twin-lamellae and small inclusions of muscovite and clinozoisite. These inclusion-rich plagioclase grains are rarely mantled by inclusion-free Pl II. Orange-brown biotites form unoriented aggregates or are aligned parallel to the main foliation of the rocks. Common are inclusions of zircons within biotite creating pleochroic halos in the host biotites. Recrystallized quartz constitutes together with Pl II.

Accessory minerals are muscovite, titanite, allanite, apatite, zircon, amphibole, tourmaline, and calcite. The large grain size of titanite, allanite, zircon, and apatite is remarkable (Fig. 4.13a-b). Reddish-brown allanite (Fig. 4.13a) forms elongated prismatic crystals (<2 mm), characterized by pale brown to reddish-brown pleochroism and twinning after {100}. Under crossed polarizers allanite displays blue to orange interference colors of second and third order, revealing distinctive chemical zoning patterns. Inclusions of biotite, apatite, zircon and coronas of (clino-) zoisite are common.

Euhedral titanite forms sphenoidal crystals of light brown color (<1 mm). They occur together with biotite, often in unoriented agglomerates of micas and apatite, and occasionally reveal chemical zoning under crossed polarizers. Apatite in the matrix is characterized by anhedral grain shape (<500 µm); however a hexagonal prismatic habitus is observed where apatite is preserved as inclusion in biotite (Fig. 4.13b). Prismatic zircon is of pale-brown color (Fig. 4.13b) with a grain size varying between 100 µm and 1000 µm. Subordinate amphibole is characterized by its euhedral shape, good cleavage parallel {110} and pale-green pleochroism. Tourmaline forms small (100 µm) subhedral grains with pale blue cores and brown rims. Calcite may occur either aligned along veinlets or disseminated in the matrix.

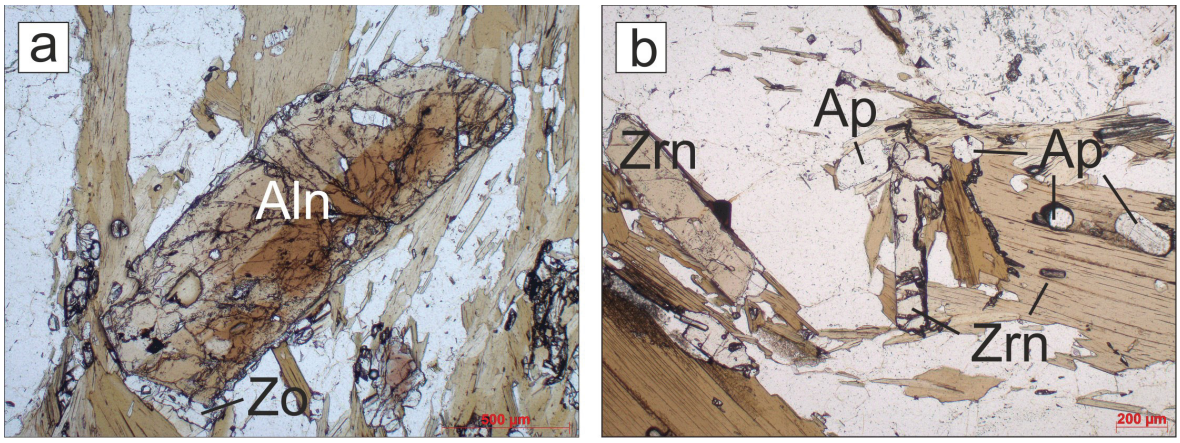

Fig. 4.13 Photomicrographs of Hochweißenfeld gneiss sample FB-35/37; plane polarized light. **a)** Twinned allanite (Aln) mantled by zoisite (Zo). Biotite is oriented parallel to the foliation. **b)** Large pale-brown zircons associated with unoriented biotite; note small prismatic zircon inclusion in biotite. Apatite as inclusion in biotite reveals a hexagonal prismatic habitus.

4.2.5 Granatspitz gneiss

ST-03/30, ST-04/30, FB-08/30

The Granatspitz gneiss occurs in the lowest tectonic unit in the central Tauern Window and forms a dome-like intrusive body (ca. 100 km^2) between Amertal and Kapruntal (Fig. 2.1). The wall rocks are amphibolites and biotite-schists showing tectonic contacts to the orthogneiss. Xenoliths of wall rocks and intrusive contacts were reported by Cornelius (1942a), indicating that the cover of the Granatspitz gneiss reflects the primary country rocks of the metagranitoid (Finger et al. 1993).

Basically, the Granatspitz gneiss is a medium- to coarse-grained two-mica leucogranite (Fig. 4.14a). According to the degree of deformation, porphyritic augengneisses (Fig. 4.14b) and more pristine undeformed metagranitoids occur. The major difference to the Zentralgneise of the Zillertl-Riffl Nappe is the occurrence of intertwined biotite and muscovite forming rectangular pseudomorphs (<1 cm) after cordierite (Frasl 1967; Fig. 4.14c-d). Matrix-biotite is commonly reddish-brown and partly reacted at its rims to white-mica and/or chlorite. Euhedral porphyritic potassium feldspars (<2 cm) with abundant plagioclase inclusions are commonly twinned after the Karlsbader law and show perthitic exsolution. Plagioclase phenocrysts (<1 cm) are twinned following the albite law with narrow-spaced polysynthetic twin lamellae. They usually display minute white mica and clinozoisite inclusions. Additionally, a second inclusion-free plagioclase generation forms rims around primary plagioclase porphyroclasts or occurs as individual recrystallized grains (<100 µm) in the matrix. Typical accessory minerals are apatite, allanite, epidote, zircon, garnet, and monazite. The latter was not found in the studied samples but has been described as altered grains overgrown by a corona of apatite, allanite and epidote by Finger et al. (1998). Blueish-fluorescent scheelite was observed in the Granatspitz gneiss sample ST-03/30.

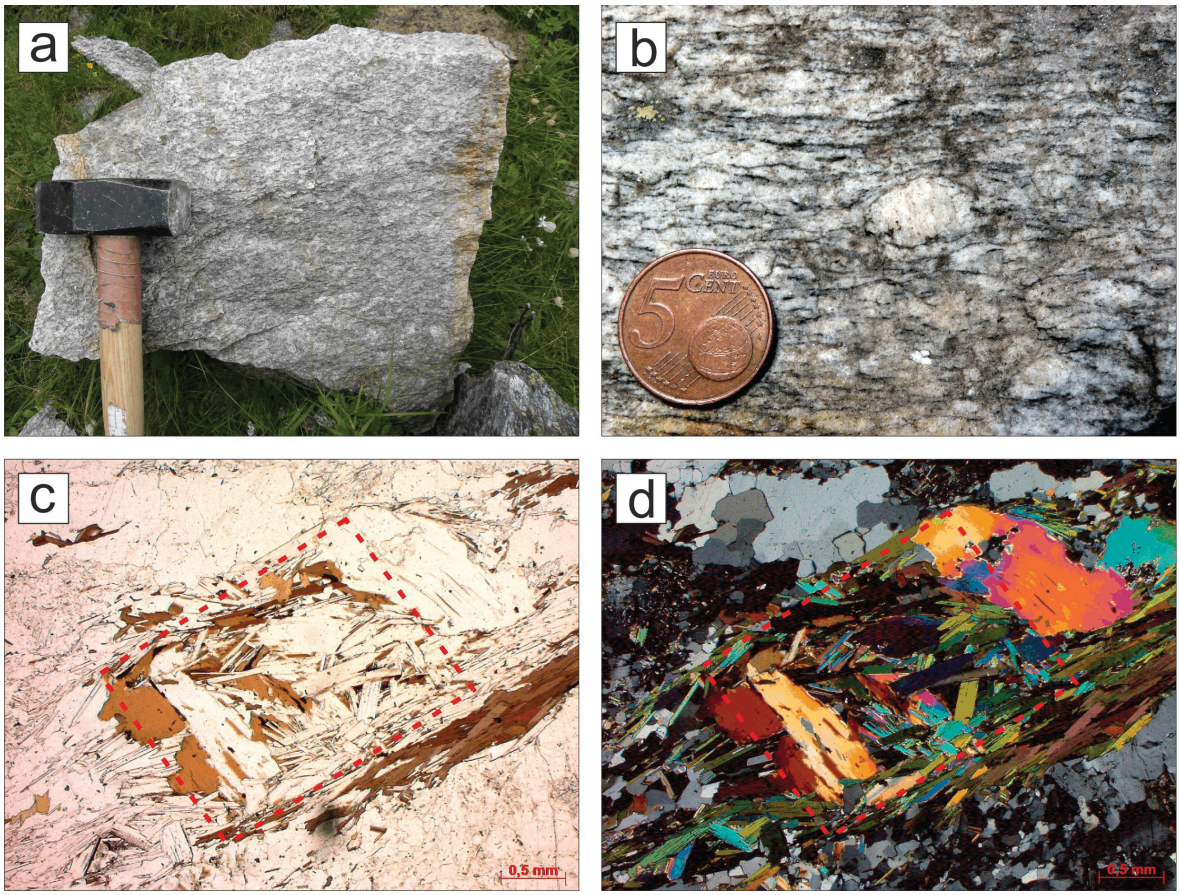

Fig. 4.14 Photographs of the Granatspitz gneiss. **a)** A loose boulder of Granatspitz gneiss near the north-eastern Felbertauerntunnel portal; sample locality FB-08/30. **b)** Gneissic texture with isolated potassium feldspar porphyroclasts; sample FB-08/30. **c)** Photomicrograph of a rectangular pseudomorph of biotite and muscovite after cordierite. The red dashed line approximately illustrates the former grain shape of cordierite; plane polarized light, sample FB-08/30. **d)** The same pseudomorph in cross polarized light.

4.2.6 Weißeneck-Dichtensee gneiss

FH-42/37, FH-43/37, FH-44/37, FH-45/37, FH-46/37, FH-47/37

The Weißeneck-Dichtensee gneiss occurs in the area around Kratzenbergsee (Hollersbachtal) and can be traced eastwards to Dichtensee, near St. Pöltner Hütte (Fig. 2.1). It is a fine- to medium grained leucocratic orthogneiss (Fig. 4.15a), which is interpreted to reflect a higher differentiated and more felsic stage of the Zillertal-Venediger granitoid (Fuchs 1958; Schermaier 1991). The country rocks are migmatites of the Zillertal-Riffl Nappe that are discordantly intersected by the Weißeneck-Dichtensee gneiss. Occasionally, xenoliths of biotite-rich orthogneisses and discordant aplitic dikes occur (Schermaier 1991, Fig. 4.15b).

Under the microscope, plagioclase forms subhedral grains (<500 µm) showing the typical exsolution of white mica and clinozoisite as described from other Zentralgneise. Frequently, plagioclase is twinned after the albite law and displays polysynthetic twin lamellae. Additionally, untwinned and inclusion-free plagioclase forms part of the matrix assemblage. Most of the potassium feldspars display tartan twinning of microcline; perthitic exsolution is rare. Contrary to the above described orthogneisses, no potassium feldspar porphyroclasts were observed. Quartz forms layers of partly recrystallized grains (<200 µm, Fig. 4.15c-d). Biotite displays a strong pleochroism of dark-brown to pale-brown and is often chloritized. Accessory minerals are muscovite, apatite, allanite, clinozoisite, epidote, titanite, zircon and carbonate. Clinozoisite forms either a fine rim around allanite or occurs as isolated hexagonal grains in the matrix. Muscovite is very rare in the matrix.

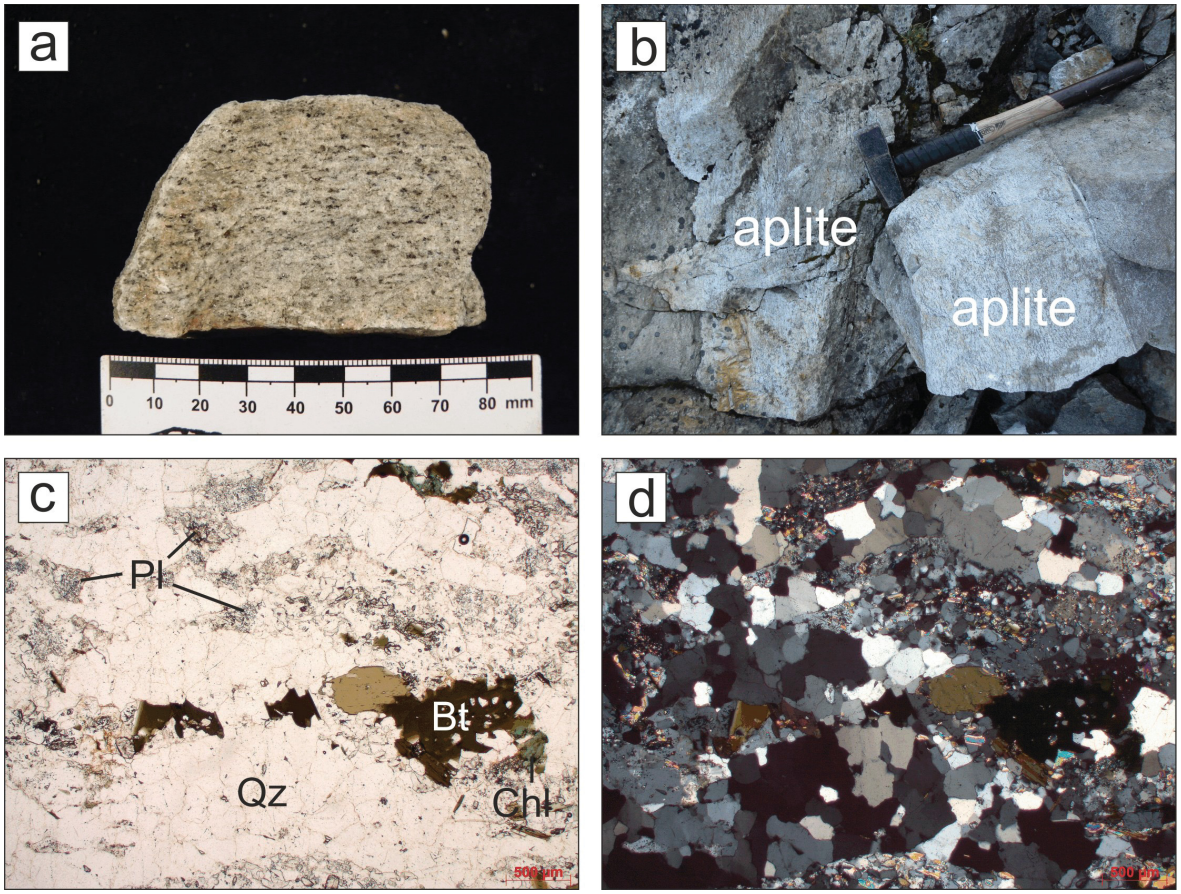

Fig. 4.15 Photographs of the Weißeneck-Dichtensee gneiss. **a)** A hand specimen of the fine-grained leucocratic sample FH-47/47. **b)** Aplitic dike crosscutting the Weißeneck-Dichtensee gneiss near Fürther Hütte. **c)** Coarse-grained dynamically recrystallized quartz ribbons in a fine-grained matrix consisting of plagioclase (Pl), quartz and biotite (Bt). Latter is partly chloritized (Chl); plane polarized light, sample FH-47/47. **d)** The microarea shown in c in cross polarized light.

4.2.7 Aplite from Achselalm

AA-49/39

Leucocratic aplitic dikes – 0.1-6.0 m thick – occur in the area of the historical Pb-Zn-F district Achselalm-Flecktruhalm. The aplites crosscut coarse-grained amphibolites and hornblendites (meta-diorites) belonging to the Habach Complex (Carl et al. 1988). These authors postulated a genetic relation of the aplites with the Tux meta-granitoid ("Habachzunge") though the boundary between the Zentralgneis and the meta-diorite is tectonic in nature (Petraschek 1945, page 133). Sparse scheelite mineralization in the aplites was described from the area Reichertleitenalm-Achselalm (Höll 1969). One sample of a very fine-grained scheelite-bearing quartz-aplite with subordinate amounts of plagioclase and biotite was sampled at the slope of Reichertleitengraben for analyses of the Rb/Sr isotopic systematics in scheelite and U-Pb, Lu/Hf isotopic systematics in zircon. No further petrographic studies were performed on the respective sample.

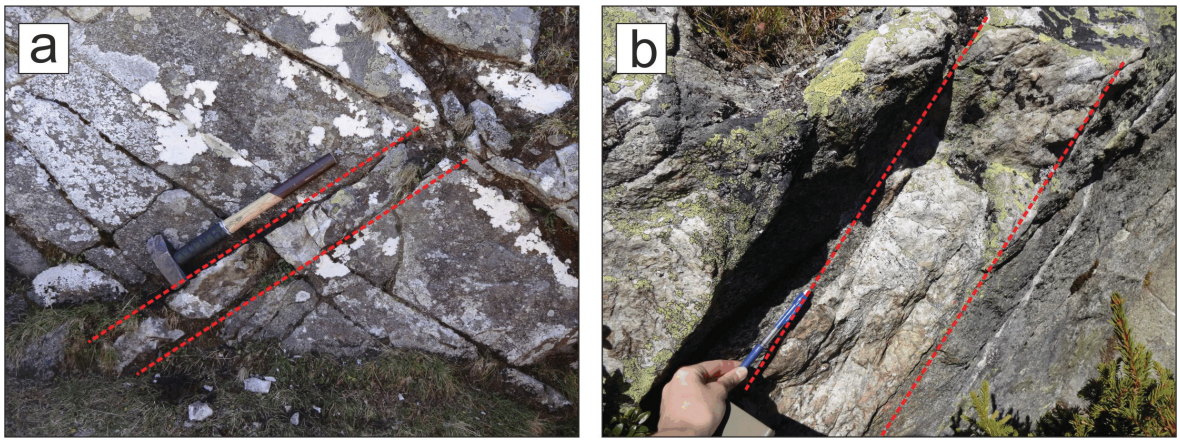

Fig. 4.16a-b Photographs of the leucocratic aplitic dikes containing sparse scheelite mineralization at the slope of Reichertleitengraben.

5 Results

5.1 Whole rock geochemical analyses

5.1.1 Classification based on the Q-ANOR diagram

From the Felbertal scheelite deposit the dark-colored K1-K3 orthogneiss (12 samples), light-colored K1-K3 orthogneiss (12 samples), aplite gneiss (3 samples), younger K2 orthogneiss (4 samples), K2 groundmass (1 sample), and quartz-diorite gneiss (6 samples) were considered for geochemical whole rock analyses. To complement the own data set, additional whole rock analyses of previous works (cf. page 244 in Höll and Eichhorn 2000) were taken into consideration. This includes analytical results from one sample of the granite gneiss underlying the laminated scheelite-quartz ore from the eastern ore field and the K2 groundmass (3 analyses) plus the younger K2 orthogneiss (1 analysis) from the western ore field. The group of Zentralgneise comprises the Felbertauern augengneiss (11 samples), Granatspitz gneiss (3 samples), Knorrkogel gneiss (10 samples), Hochweißenfeld gneiss (9 samples), and Weißeneck-Dichtensee gneiss (6 samples). The analytical results are listed in Appendix D.

Streckeisen and Le Maitre (1979) proposed an empirical binary CIPW-normative classification scheme, which tempts to reconcile modal and normative mineralogy. Their method is based on the two parameters Q (= CIPW-normative Qz/(Qz+Or+Ab+An)*100) and ANOR (= CIPW-normative An/(An+Or)*100). The nomenclature is analogous to Streckeisen (1976), although Streckeisen and Le Maitre (1979) additionally account for calcic tonalite (field 3b). The arbitrary field boundaries of the classification scheme were drawn after plotting a data set of 2500 plutonic rock analyses with mostly well-known modal mineralogy. The advantage of this method lies in the fact that knowledge of the modal mineral abundance of the rock is not required as it is for the classical IUGS quartz-alkali feldspar-plagioclase-feldspathoid (QAPF) classification scheme (cf. Streckeisen 1976, Le Bas and Streckeisen 1991).

EPMA analyses of plagioclase have revealed two different plagioclase generations with distinct anorthite composition ranging from An_{00} to An_{25} in all orthogneisses. Consequently, the use of the QAPF method might portray a delusive nomenclature because plagioclase with a composition between An_{00} and An_{05} has to be assigned to the alkali feldspar component and the modal abundances are unknown. Recently, Whalen and Frost (2013) compared five different classification schemes for granitic rocks based

on geochemical data of feldspathic igneous rocks published in Frost and Frost (2008). They could show that the Q-ANOR classification scheme corresponds best with the IUGS method based on the modal mineralogy of the plutonic rocks.

Felbertal scheelite deposit

In the Q-ANOR diagram (Fig. 5.1), the dark-colored K1-K3 orthogneiss plots within the field of monzogranite. Three outlying samples (A-K1h, Gn-1152a, K1-45.59) are shifted to a granodioritic composition because of lower K_2O concentrations and consequently lower normative orthoclase content. The light-colored K1-K3 orthogneiss variety is classified as syeno- and monzogranite. Again, one outlier (K1-31.59) plots in the granodiorite field. The aplite gneiss generally exhibits the highest ANOR values with respect to the K1-K3 orthogneiss series, showing a granodioritic composition.

The K2 groundmass displays a great affinity with the K1-K3 orthogneiss and plots within the fields of monzogranite and granodiorite. In contrast, the Younger K2 orthogneiss and the quartz-diorite gneiss show a differentiation trend from quartz diorite to tonalite. The granite gneiss underlying the laminated scheelite-quartz ore is tonalitic in composition.

Zentralgneise

The majority of the studied Zentralgneise (Felbertauern augengneiss, Knorrkogel gneiss, Weißeneck-Dichtensee gneiss) plot within the fields of syeno- and monzogranites (Fig. 5.1). The Granatspitz gneiss is classified as alkali feldspar granite in the Q-ANOR diagram. The compositional heterogeneity of the Hochweißenfeld gneiss is well shown by the significant spread across the quartz monzodiorite field towards granodiorite, monzogranite and even alkali feldspar granite. Finger et al. (1993) already mentioned the monzonitic affinity in the Hochweißenfeld gneiss. The presented classification of the Zentralgneise is in good agreement with published data, though a little shift to more granitic and normative Or-richer compositions is to be seen in the Q-ANOR plots when compared with those based on modal compositions (Finger et al. 1993).

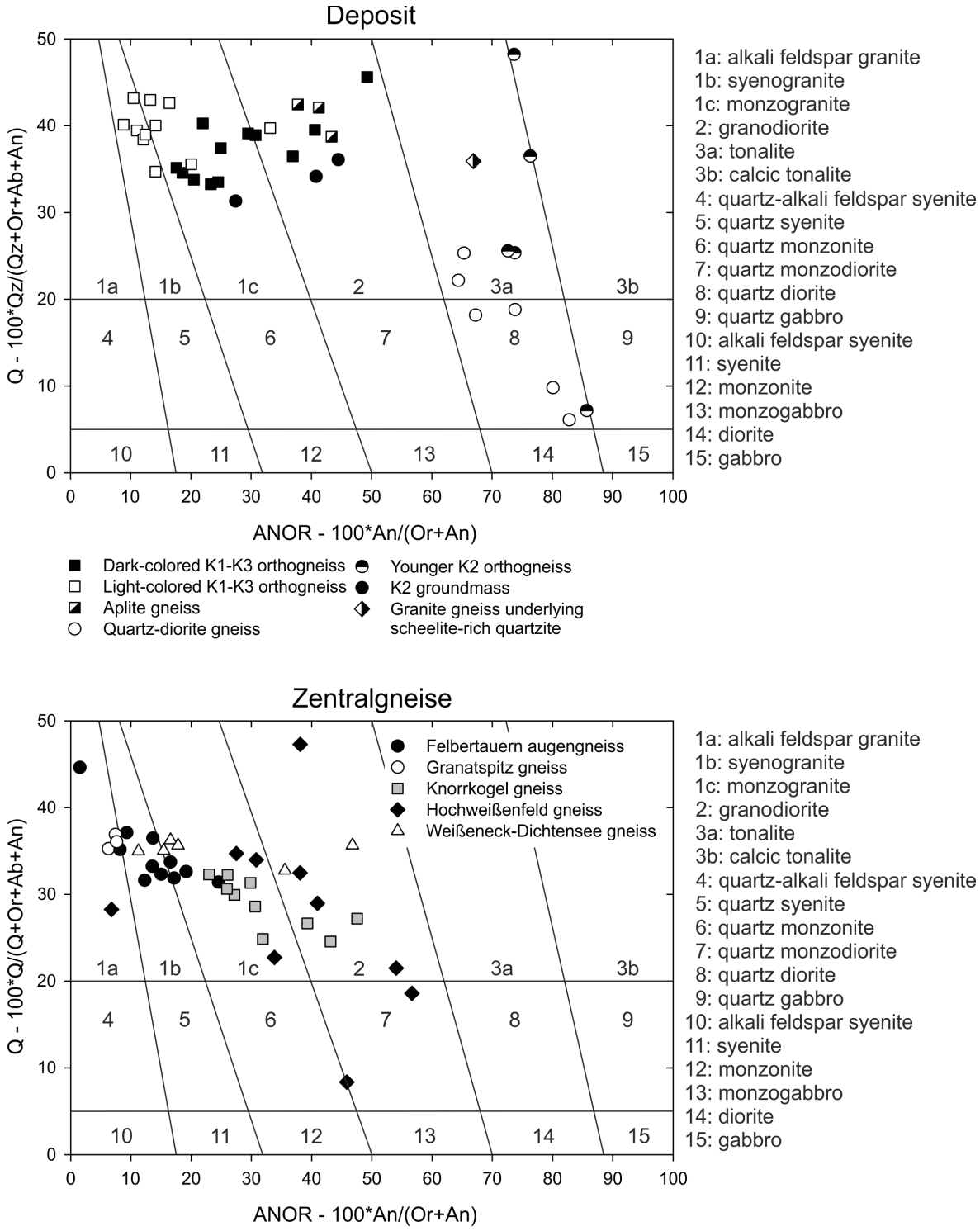

Fig. 5.1 Classification of metagranitoids based on the Q-ANOR scheme (Streckeisen and Le Maitre 1979). The upper diagram displays metagranitoids from the Felbertal scheelite deposit, the lower one the different Zentralgneise studied.

5.1.2 Geochemical classification of granitic rocks

To avoid classifying granites by their genetic environment, Frost et al. (2001) introduced a non-genetic, non-tectonic classification scheme for granitic rocks based on geochemical parameters that synthesizes criteria from already established schemes. Three major-element geochemical criteria account for the chemical complexity of granitic rocks. The ratio $FeO_{tot}/(FeO_{tot}+MgO)$ – termed Fe* – largely reflects the differentiation history of the granitoid and distinguishes granites with Fe enrichment from Mg-rich ones. The second parameter, based on the classification scheme of Peacock (1931), is the modified alkali-lime index MALI (Na_2O+K_2O-CaO) that mostly reflects the plutonic compositional trends inherited from the source of the granitic melts. The last criterion is the alumina saturation index (ASI) by Shand (1943), describing the ratio of molar $Al_2O_3/(CaO-1.67\cdot P_2O_5+Na_2O+K_2O)$ that subdivides granites into metaluminous, peraluminous and peralkaline composition. This expression of the ASI additionally involves the presence of apatite. Based on these parameters, Frost et al. (2001) distinguishes 16 possible compositional groups of granitic rocks, although ferroan calcic and calc-alkalic peralkaline granitoids should not exist in nature (Frost and Frost 2010). The quartz-diorite gneiss is excluded in this consideration since the respective rocks do not represent a granitic composition sensu lato.

Felbertal scheelite deposit

The K1-K3 orthogneisses are characterized by Fe* ranging from 0.64 in the dark-colored K1-K3 variety to 0.90 in the aplite gneiss (Fig. 5.2). Values of Fe* linearly increase with rising SiO_2-concentration from the dark-colored variety to the aplite gneiss, reflecting their protracted magmatic differentiation. Most analyses plot within the field of magnesian granitic compositions, expect the aplite gneiss and single light-colored K1-K3 orthogneiss sample (K1-1234).

The values of MALI scatter for the K1-K3 orthogneiss between the calc-alkalic and the calcic trend. The aplite gneiss and the granite gneiss underlying the laminated scheelite-quartz ore correspond to the calcic composition. The ASI separates the K1-K3 orthogneiss in a metaluminous dark-colored variety (ASI= 0.93-1.03) and in a mildly peraluminous light-colored K1-K3 orthogneiss variety (ASI= 0.99-1.08; one outlier at 1.18); the aplite gneiss shows the highest peraluminosity (ASI= 1.11-1.12).

The K2 groundmass has low Fe* values (0.47-0.64), while the younger K2 orthogneiss plots along the field boundary of magnesian and ferroan granitic compositions

indicating high Fe/Mg ratios ranging between 0.78 and 0.88 (Fig. 5.2). The values of MALI are low for both younger K2 orthogneiss (0.57-4.14) and K2 groundmass (-0.03-3.33) reflecting their calcic composition. According to the ASI, the K2 groundmass is strongly metaluminous (0.66-0.87), whereas the younger K2 orthogneiss plots at higher values similar to the dark-colored K1-K3 orthogneiss (0.92-1.03). Table 5.1 summarizes the different granitic rocks of the Felbertal scheelite deposit according to the three classification criteria.

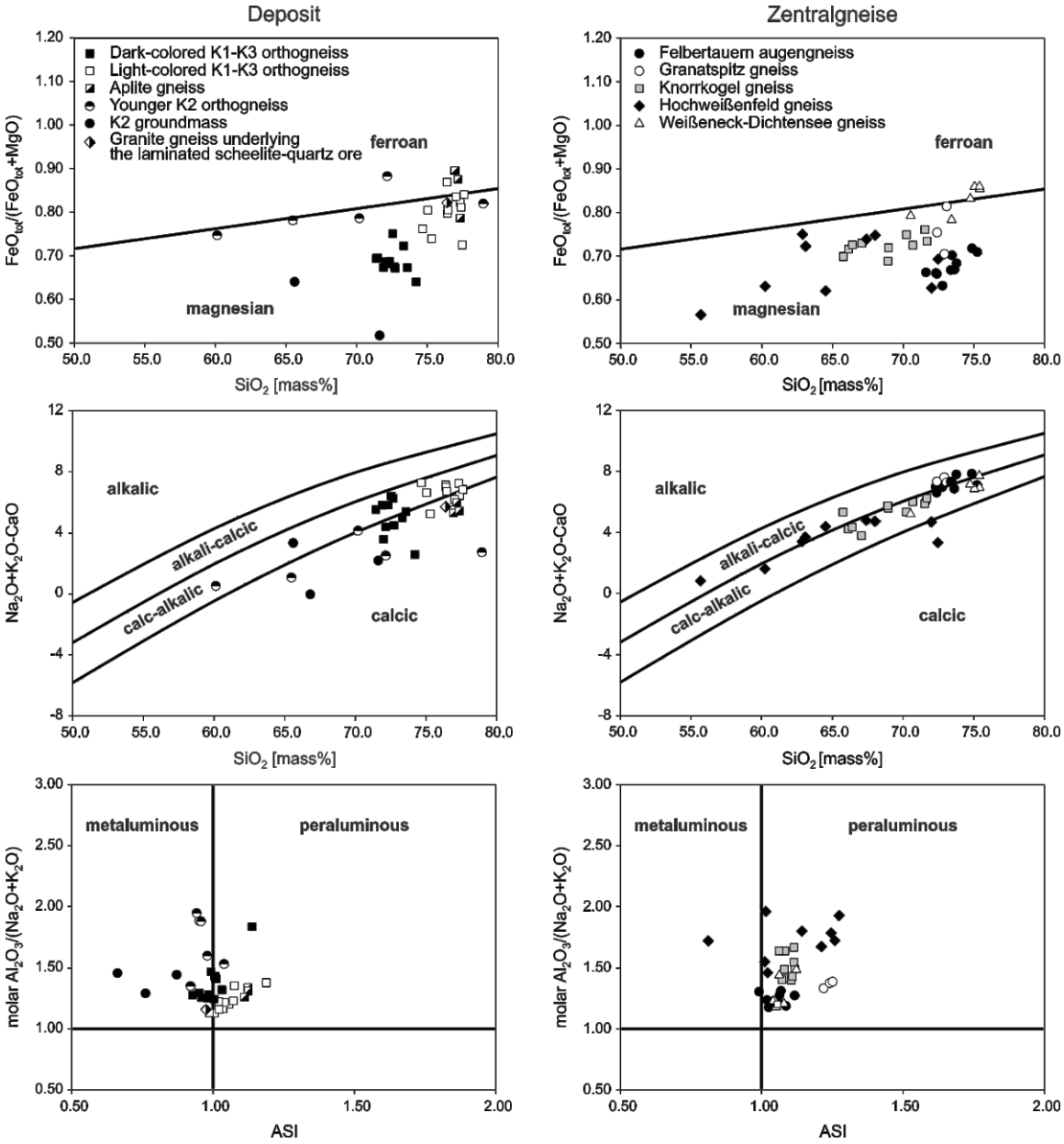

Fig. 5.2 Illustration of the geochemical classification scheme for granitic rocks based on the Fe*, MALI and ASI (Frost et al. 2001). Field boundaries were drawn referring to the line fits given in Frost et al. (2001).

	Dark-colored K1-K3 orthogneiss	Light-colored K1-K3 orthogneiss	Aplite gneiss	Younger K2 orthogneiss	K2 groundmass
Fe*	magnesian	magnesian	ferroan (magnesian)	magnesian (ferroan)	magnesian
Modified MALI	calc-alkalic calcic	calc-alkalic (calcic)	calcic	calcic (calc-alkalic)	calcic (calc-alkalic)
ASI	metaluminous	peraluminous	peraluminous	metaluminous	metaluminous

	Felbertauern augengneiss	Granatspitz gneiss	Knorrkogel gneiss	Hochweißen-feld gneiss	Weißeneck-Dichtensee gneiss
Fe*	magnesian	magnesian	magnesian	magnesian	ferroan (magnesian)
Modified MALI	alkali-calcic calc-alkalic	alkali-calcic	calc-alkalic	alkali-calcic calc-alkalic	calc-alkalic
ASI	peraluminous	peraluminous	peraluminous	peraluminous	peraluminous

Tab. 5.1 Descriptive prefixes for granitic rocks of the Felbertal scheelite deposit and Zentralgneise based on the classification scheme of Frost et al. (2001).

Zentralgneise

The Zentralgneise are magnesian in respect of Fe* with the exception of the Weißeneck-Dichtensee gneiss that displays an evolutionary trend across the field boundary towards weakly ferroan compositions. According to MALI, all Zentralgneise are distributed along the field boundary between alkali-calcic and calc-alkalic. A striking feature of all Zentralgneise in the central Tauern Window is their peraluminous character. The Felbertauern augengneiss, the Knorrkogel gneiss and the Weißeneck-Dichtensee gneiss are similar regarding their ASI (ASI= 0.99-1.12, mildly peraluminous). On the contrary, the Hochweißenfeld gneiss and the Granatspitz gneiss display the highest enrichment in Al in respect to the alkalis (ASI= 1.20-1.30) conforming their crustal source (Finger et al. 1993, Finger et al. 1998, Eichhorn et al. 2000). Table 5.1 summarizes the different Zentralgneise according to the three classification criteria.

5.1.3 Bivariate major and trace element distribution diagrams

Harker diagrams for major (Fig. 5.3) and trace elements (Fig. 5.4) highlight the compositional range observed in orthogneisses from the scheelite deposit and adjacent Zentralgneise and reveal information about differentiation trends, compositional variations and magma evolution. Using the SiO_2 concentration as an index of differentiation for the studied rocks is appropriate, since SiO_2 is the element that shows the maximum variability among all samples and increases with progressive differentiation of the evolving granitic melts. Additionally, indication of silica-(re)mobilization (e.g. greisen), which would alter the primary SiO_2 signature of the rocks, was not observed. The complete data of whole rock analyses are listed in Appendix D.

Felbertal scheelite deposit

SiO_2 concentrations increase from the dark-colored K1-K3 orthogneiss (71.45-74.21 mass%) to the light-colored K1-K3 orthogneiss (75.30-80.36 mass%). The aplite gneiss displays elevated SiO_2 concentrations equal to the light-colored K1-K3 variety in the range of 76.94 to 77.33 mass%. A reverse trend can be recognized in the elemental concentrations of Al_2O_3, Fe_2O_3, MgO, CaO, TiO_2, P_2O_5, and MnO, which are highest in the dark-colored K1-K3 orthogneiss and decrease towards the light-colored type and the aplite gneiss (Fig. 5.3). With respect to the Na_2O and K_2O concentrations (2.55-4.36 mass% Na_2O; 3.38-5.40 mass% K_2O), no significant correlation with SiO_2 exists and compositional differences between the dark-colored and the light-colored K1-K3 orthogneiss varieties were not observed. However, samples A-K1h, Gn-1152A and K1-45.59 from the dark-colored K1-K3 orthogneiss and samples Gn-700 and K1-31.59 from the light-colored variety are displaced to lower K_2O contents (1.49-2.62 mass%) compared to the corresponding cluster. Na_2O is highest in the aplite gneiss (4.94-5.94 mass%) while K_2O is very low (0.86-1.39 mass%).

Regarding the trace element composition of the K1-K3 orthogneisses, a systematic decrease in the elements Ba, Sr, F, and the total rare earth elements (∑REE) from the dark-colored variety to the light-colored K1-K3 orthogneiss is evident in figure 5.4. The same trends are seen for Zr, V, Sn, Zn, Ni and Tl (not shown). The Cs contents in the dark-colored K1-K3 orthogneiss (10-39 ppm) are slightly higher than in the light-colored variety (5-15 ppm) and decrease to 3 ppm in the aplite gneiss (Fig. 5.4). Rb is irregularly distributed in the dark-colored and light-colored K1-K3 orthogneiss (300-580 ppm); however, similar to K_2O, samples A-K1h, Gn-1152A and K1-45.59 from the dark-colored

variety and samples Gn-700 and K1-31.59 from the light-colored variety display lower Rb contents ranging from 130-272 ppm, which are concentrations comparable to the aplite gneiss (101-252 ppm). Thorium slightly decreases from the dark-colored variety (26-38 ppm) to the light-colored variety (21-29 ppm) and the aplite gneiss (22-24 ppm). Remarkable characteristics of the K1-K3 orthogneiss are the high concentrations of F in the dark-colored variety (2383-4438 ppm) and Nb (45-58 ppm; one outlier with 86 ppm), Ta (5-13 ppm) and U (33-51 ppm; one outlier with 74 ppm) in both types (Fig. 5.4). The aplite gneiss features the highest Nb and Ta contents ranging from 68 to 74 ppm Nb and 16 to 18 ppm Ta, whereas U is equally high as in the dark-colored and light-colored orthogneiss varieties.

Interestingly, the chemical signature of the aplite gneiss from the western ore field perfectly matches that of the granite gneiss underlying the laminated scheelite-quartz ore in the eastern ore field reported by Höll and Eichhorn (2000). Other significant features of the K1-K3 orthogneiss and the aplite gneiss are high and variable concentrations of Be (< 111 ppm), Mo (< 417 ppm), Pb (< 343 ppm), As (< 127 ppm), W (< 4683 ppm) and Bi (< 787 ppm) (cf. Appendix D). Analyses of Hf reveal a limited range in concentrations of 4.3-7.9 ppm, similar to all other lithologies considered.

Similar trends in major element concentrations (Fig. 5.3) as observed in the K1-K3 orthogneisses are displayed by the younger K2 orthogneiss, though the respective orthogneiss covers a wider range of SiO_2 concentrations; i.e. from 60.13 to 78.95 mass% SiO_2. Samples showing the highest SiO_2 concentrations (Gn-800 and AP-63.31) have major element concentrations similar to the K1-K3 orthogneiss. Only CaO is slightly elevated in the younger K2 orthogneiss (2.11-6.48 mass%) and K_2O is constantly lower than in the K1-K3 orthogneiss (0.63-1.28 mass%). Moreover, a poor correlation of Na_2O and K_2O with SiO_2 can be inferred from the Harker diagrams. The low-SiO_2 members of the younger K2 orthogneiss show higher concentrations of Al_2O_3 (16.65-21.76 mass%), Na_2O (4.54-6.23 mass%) and CaO (4.75-6.48 mass%) than the K1-K3 orthogneiss. With respect to trace element composition, the younger K2 orthogneiss has Ba, Cs, and REE contents in the range of the K1-K3 orthogneisses, whereas Sr and Zr concentrations are higher. Fluorine contents in the younger K2 orthogneiss are comparable to the light-colored K1-K3 orthogneiss. In contrast, Nb, Ta, U, and Th are significantly lower in the younger K2 orthogneiss. Furthermore, the respective orthogneiss contains scattering but lower concentrations of Be (8-78 ppm), Sn (6-68 ppm), Mo (21-66 ppm), Cu (45-555 ppm), Pb (2-99 ppm), Zn (9-31 ppm), W (65-1790 ppm), Ni (3-10 ppm),

As (1-22 ppm), and Bi (1-149 ppm). Based on the chemical data a differentiation trend with increasing SiO_2 concentrations and decreasing Al_2O_3, CaO, TiO_2, P_2O_5, Ba, Sr, and REE contents can be established for the younger K2 orthogneiss.

The quartz-diorite gneiss is characterized by low SiO_2 concentrations and high Al_2O_3, Fe_2O_3, CaO, MgO and TiO_2 contents. K_2O is below 2.00 mass% and Na_2O concentrations range from 3.80 to 5.14 mass% showing a linear positive (K_2O) and negative (Na_2O) trend with increasing SiO_2 (Fig. 5.3). Phosphorous concentrations are slightly higher compared to the dark-colored K1-K3 orthogneiss. An increase of Ba, Cs and Rb with rising SiO_2 concentrations is peculiar for the quartz-diorite gneiss, while Zr, REE and Nb decrease (Fig. 5.4). The highest concentrations of ∑REE (182-390 ppm), Sr (315-537 ppm), V (125-196 ppm), Zr (197-404 ppm), and Tl (1.1-5.3 ppm) were detected in the quartz-diorite gneiss. Fluorine contents are similar to the light-colored K1-K3 orthogneiss variety. The concentrations of U, Nb and Ta are slightly higher than in the younger K2 orthogneiss, but lower than in the K1-K3 orthogneiss.

The K2 groundmass features SiO_2 concentrations in the range of 65.61 to 73.62 mass% (Fig. 5.3). A decrease of Fe_2O_3, CaO, K_2O, TiO_2, MnO, and Ba contents with increasing SiO_2 is characteristic. The highest concentrations of P_2O_5 (0.57-0.67 mass%), Cs (92-235 ppm), Rb (131-673 ppm) and F were detected in the K2 groundmass. Fluorine in the K2 groundmass is above the upper detection limit, exceeding 1 mass% F. Uranium (6-32 ppm) and Nb (13-30 ppm) are slightly elevated and comparable to the K1-K3 orthogneiss, whereas Ta is low (2-4 ppm).

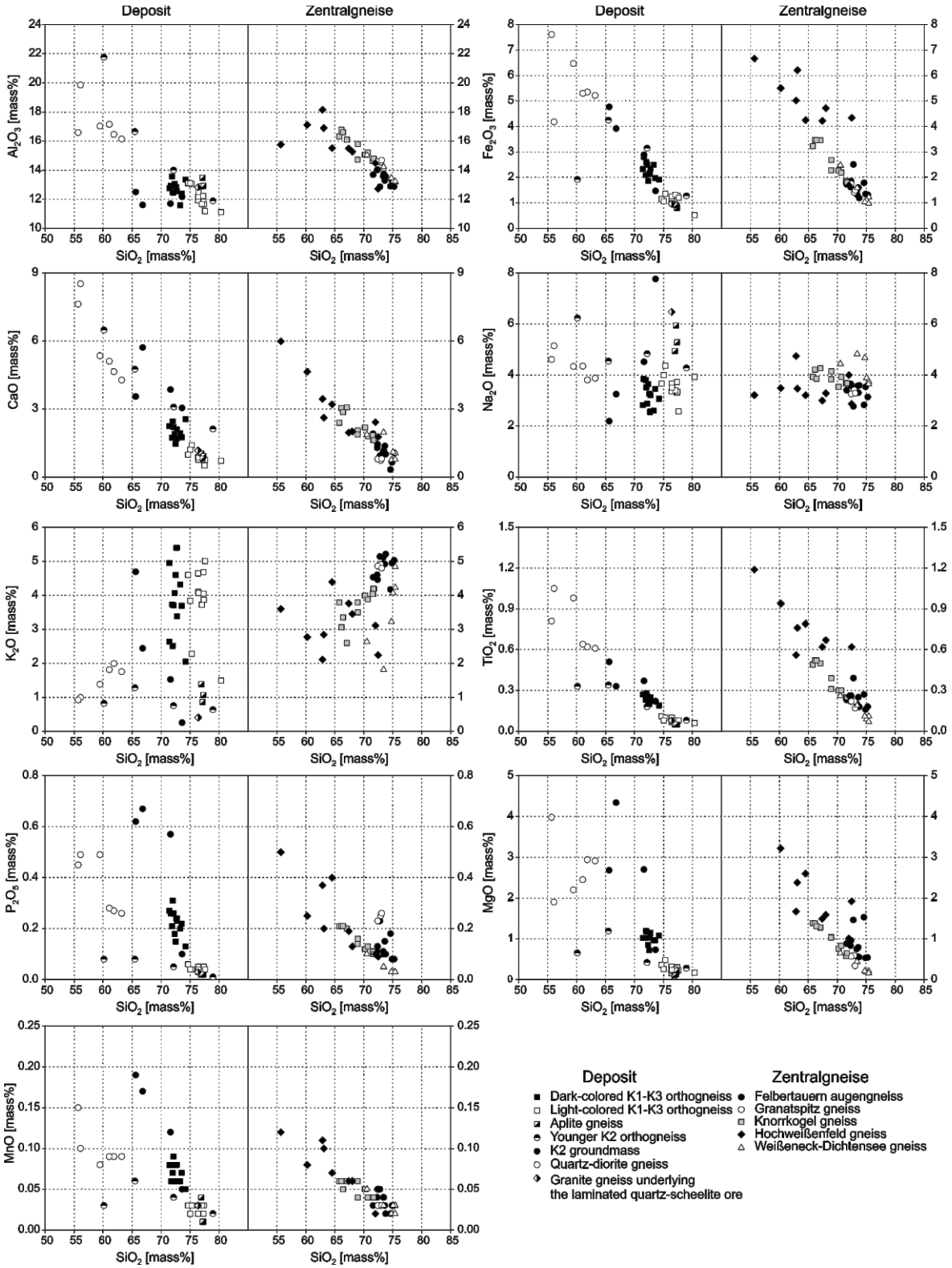

Fig. 5.3 Harker diagrams for major elements in orthogneisses from the Felbertal scheelite deposit and Zentralgneise.

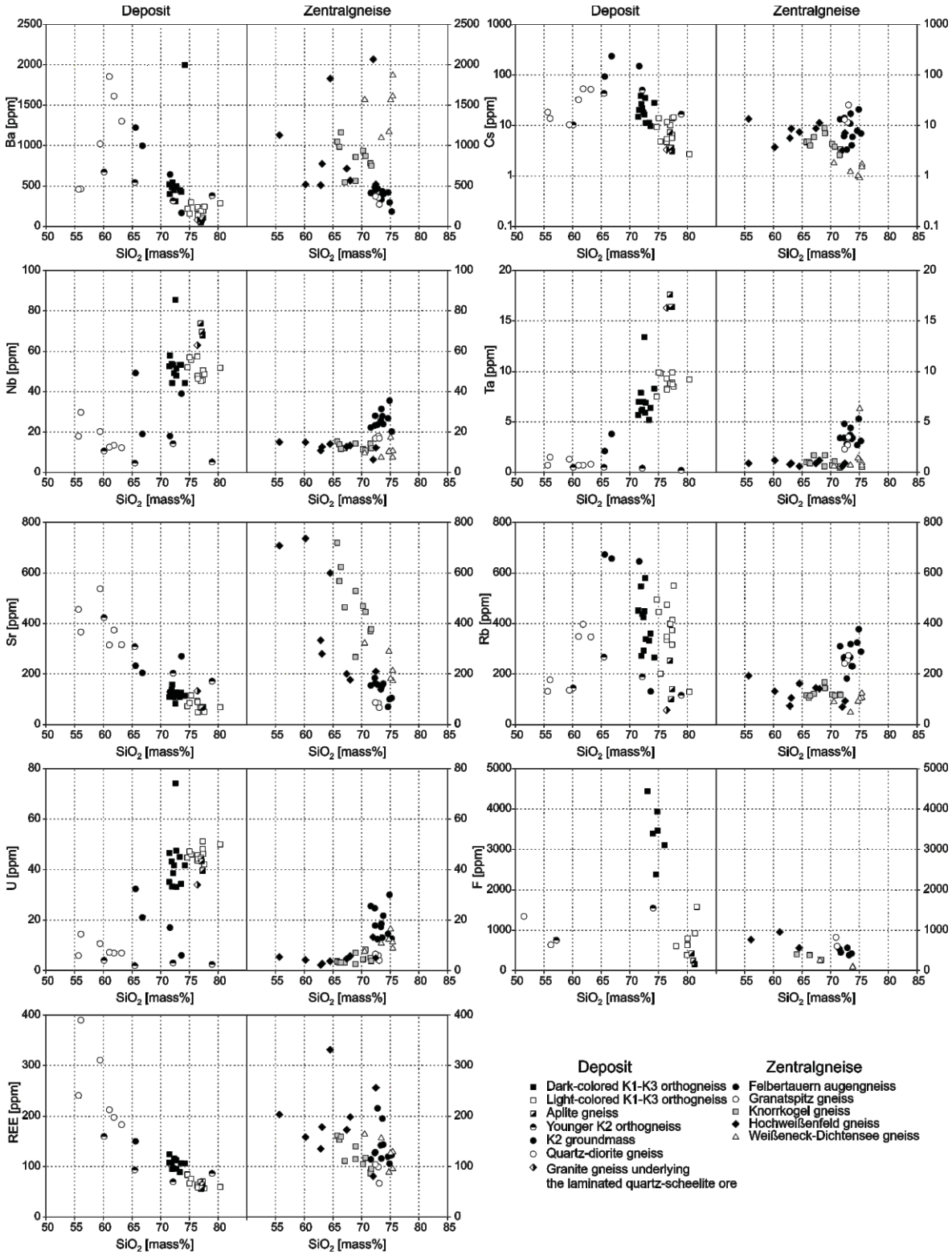

Fig. 5.4 Harker diagrams for trace elements in orthogneisses from the Felbertal scheelite deposit and Zentralgneise. Note logarithmic scale for Cs.

Zentralgneise

Analytical results of the Felbertauern augengneiss display high SiO_2 concentrations (71.60-75.24 mass%) and a linear trend of decreasing Al_2O_3, Fe_2O_3, CaO, TiO_2, Ba, and Sr with increasing SiO_2 content (Appendix D). Aluminum is slightly elevated (12.88-14.04 mass%) when compared to the K1-K3 orthogneiss. The highest K_2O concentrations in Zentralgneise prevail in the Felbertauern augengneiss with values, similar to the K1-K3 orthogneisses, ranging from 4.17 to 5.21 mass% K_2O. The Na_2O concentrations of all analyzed Zentralgneise generally scatter within a small compositional range, whereby the Felbertauern augengneiss is characterized by relatively low concentrations (2.82-3.65 mass% Na_2O). Phosphorous shows no conclusive trend with concentrations scattering between 0.08 and 0.23 mass%. Fluorine concentrations are in the range of other Zentralgneise with values between 383 and 561 ppm. Furthermore, Cs and Rb contents are relatively high and variable, ranging from 4 to 21 ppm Cs and 182 to 377 ppm Rb, respectively. The most striking features of the Felbertauern augengneiss are its elevated concentrations of U (12-30 ppm), Th (26-42 ppm), Nb (20-36 ppm), and Ta (2.7-5.3 ppm).

Thus, the Felbertauern augengneiss shares certain compositional characteristics with the K1-K3 orthogneiss varieties, though some chemical differences exist. Compositional consistency between the Felbertauern augengneiss and the dark-colored K1-K3 orthogneiss variety is reflected by comparable concentrations of SiO_2 (71.60-75.24 mass%), TiO_2 (0.16-0.39 mass%), Zr (98-157 ppm; one outlier with 209 ppm), Ba (295-482 ppm; one outlier with 185 ppm), Th (26-42 ppm), and REE (106-143 ppm; two outliers with 195 and 215 ppm), whereas concentrations of CaO (0.32-1.90 mass%), MnO (0.02-0.05 mass%), Cs (4-21 ppm), and F (383-561 ppm) correspond to the light-colored K1-K3 orthogneiss. Aluminum and Sr are slightly higher in the Felbertauern augengneiss in comparison with the K1-K3 orthogneiss, whereas Fe_2O_3, P_2O_5 and MgO concentrations plot between the dark-colored and light-colored variety. Particularly the elevated Nb, Ta, Rb, U, and Th concentrations in the Felbertauern augengneiss are major parallels to the W mineralized K1-K3 orthogneiss, despite concentrations in the Felbertauern augengneiss are lower than in the K1-K3 orthogneiss (Fig. 5.4). Differences between both orthogneisses exist in the F, P, and HREE concentrations, whereby the Felbertauern augengneiss generally has lower concentrations of these elements than the K1-K3 orthogneiss.

The chemical composition of the Granatspitz gneiss matches in some respects the major and trace element distribution of the Felbertauern augengneiss. However, significant disparities are the higher Al_2O_3 (14.55-14.68 mass%) and P_2O_5 (0.23-0.26 mass%) concentrations in the Granatspitz gneiss, whereas Nb (16-18 ppm), U (4.0-6.5 ppm) and Th (6.9-11.7 ppm) are lower. Tantalum (2.3-3.5 ppm) is slightly higher compared to other Zentralgneise and matches the concentrations obtained from the Felbertauern augengneiss to some extent. Sample ST-03/30 is unique in the data record of the Zentralgneis samples in terms of its high W concentration of 76.9 ppm and visible scheelite mineralization (blueish fluorescent in short-waved UV light) in the hand specimen.

SiO_2 concentrations in the Knorrkogel gneiss range from 65.76 to 71.68 mass% SiO_2. The samples display a well-defined trend in major and trace element composition with increasing SiO_2 content. Characteristic for the Knorrkogel gneiss are elevated concentrations of Fe_2O_3 (1.80-3.48 mass%), CaO (1.62-3.07 mass%), TiO_2 (0.25-0.52 mass%), MgO (0.58-1.39 mass%), Ba (563-1163 ppm), and Sr (266-720 ppm), elements that are most compatible in micas and feldspars.

The highest concentrations of Al_2O_3 (14.49-18.15 mass%), Fe_2O_3 (4.22-6.67 mass%), CaO (1.76-5.98 mass%), TiO_2 (0.56-1.19 mass%), P_2O_5 (0.13-0.50 mass%), MnO (0.06-0.12 mass%), Zr (175-356 ppm), and REE (135-331 ppm) in Zentralgneise were detected in the Hochweißenfeld gneiss. Also Sr (177-736 ppm) and Ba (510-2068 ppm) concentrations are remarkably elevated. SiO_2 contents scatter from 55.67 to 72.47 mass%. Additionally, a compositional spread was detected in Na_2O (2.86-4.74 mass%) and K_2O (2.11-4.39 mass%).

The Weißeneck-Dichtensee gneiss represents a high SiO_2-orthogneiss with concentrations between 70.53 and 75.42 mass% SiO_2. According to the major elemental composition, the respective gneiss is similar to the Felbertauern augengneiss and Granatspitz gneiss. However, the trace element composition differs with respect to its constantly high Ba concentrations (1096-1870 ppm) and significantly low Cs contents (0.9-1.8 ppm). A notable feature of the Weißeneck-Dichtensee gneiss is the elevated U concentration of 7.5-16.4 ppm, similar to the Felbertauern augengneiss.

5.1.4 Multi-element major and trace element distribution diagrams

Normalized spider diagrams of compatible and incompatible elements depict the chemical composition of the orthogneisses and its deviation from a primitive undifferentiated reference composition. Normalization values of the upper continental crust (Taylor and McLennan 1995) and chondritic meteorites (Boynton 1984) were used.

Felbertal scheelite deposit

The multi-element plots in figure 5.5 further emphasize the chemical relationship among the two K1-K3 orthogneiss varieties and the aplite gneiss. As will be outlined in chapter 6.1 these are mostly reflecting effects of magmatic differentiation. The compositional variation within each orthogneiss variety is limited. Only Cs and Rb show more scatter (Fig. 5.5). Sample A-K1h (dark-colored K1-K3 orthogneiss) is exceptional with respect to low Rb and very high Ba contents. Moreover, sample K1-76.28 from the group of the dark-colored K1-K3 orthogneiss is remarkable due to highly elevated Nb, Ta and heavy rare earth elements (HREE) contents (Appendix D). The concentration of U in the K1-K3 orthogneisses and the aplite is up to 15 times higher than the respective concentration of the upper continental crust. The spider diagrams further highlight the depletion in the compatible elements Ba, K, Sr, P, Zr, Ti and the light rare earth elements (LREE) and enrichment of Nb, Ta, Hf, and the HREE with increasing differentiation from the light-colored K1-K3 orthogneiss to the aplite gneiss. Cesium shows a pronounced scatter in both K1-K3 gneiss varieties, though it generally decreases from the dark-colored to the light-colored K1-K3 orthogneiss. The high field strength elements (HFSE) and HREE remain similar in both K1-K3 varieties; higher concentrations occur in the aplite gneiss.

Differences among the orthogneiss varieties and the aplite gneiss are also to be seen in the chondrite-normalized REE-distribution plots (Fig. 5.5). There is a progressive decrease in LREE concentrations with the evolution of the orthogneiss as expressed in the La_N/Yb_N ratios of the dark-colored K1-K3 orthogneiss (1.91-3.08), light-colored orthogneiss (0.94-1.75) and the aplitic gneiss (0.33-0.40). Furthermore, all K1-K3 orthogneiss samples are characterized by a distinct negative Eu-anomaly [$Eu/Eu^* = Eu_N/\sqrt{(Sm_N \cdot Gd_N)}$]. The negative Eu-anomaly becomes more pronounced with increasing evolution from the dark-colored K1-K3 orthogneiss (Eu/Eu*= 0.30-0.48) to the light-colored K1-K3 orthogneiss (Eu/Eu*= 0.24-0.35) and aplite gneiss (Eu/Eu*= 0.07-0.15). A peculiar feature of the K1-K3 orthogneiss are constantly

decreasing normalized concentrations from La to Ho (excluding Eu) but increasing concentrations of the HREE (Er, Tm, Yb, Lu). Elevated Lu_N/Ho_N ratios in the K1-K3 orthogneiss (1.93-2.42 in the dark-colored variety; 1.96-2.81 in the light-colored variety) and in the aplite gneiss (2.12-2.39) reflect this remarkable trend. The REE-pattern of the aplite gneiss shows a flat LREE distribution and, a pronounced negative Eu-anomaly and increasing concentrations of the HREE with increasing atomic weight.

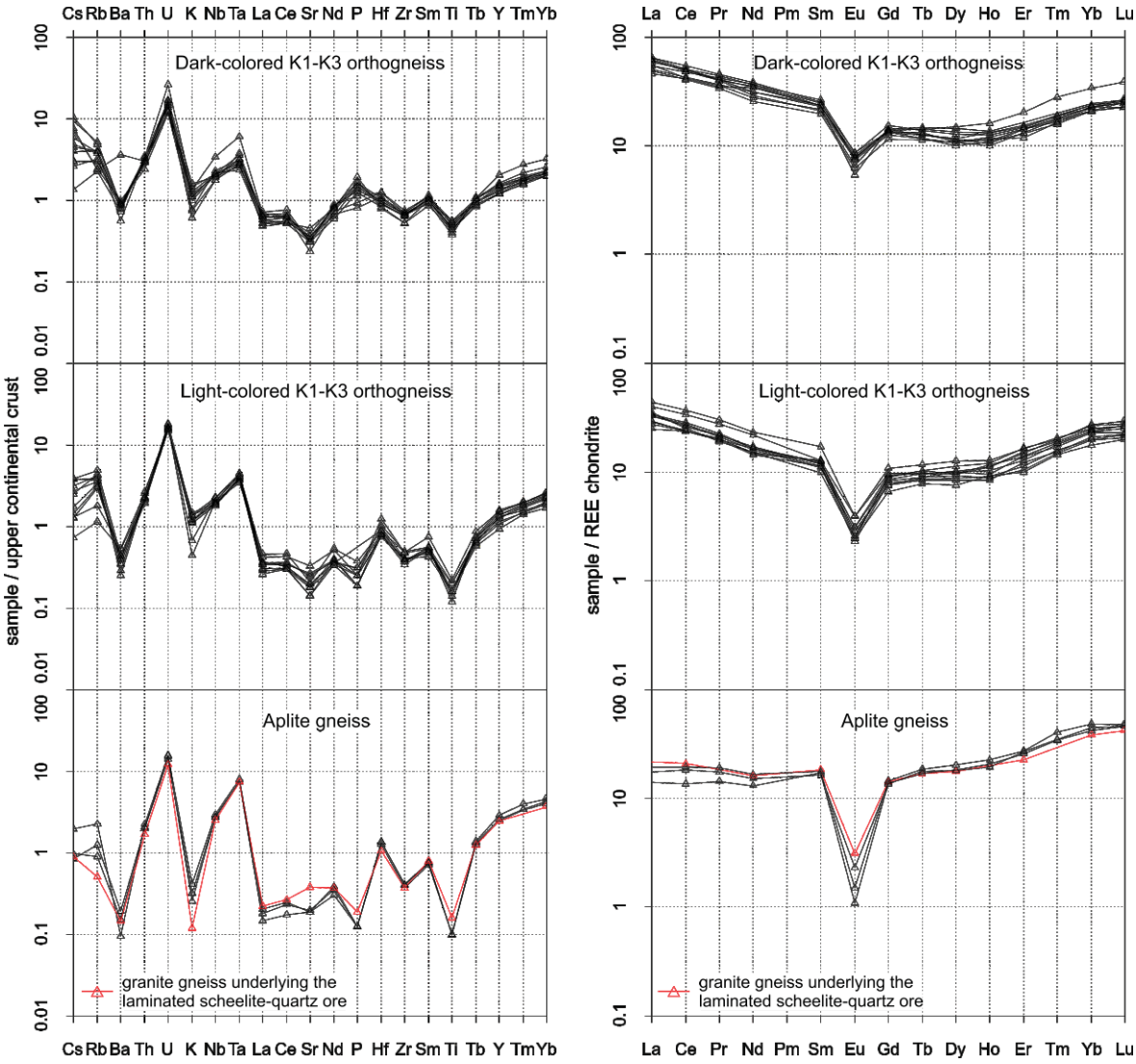

Fig. 5.5 Spidergrams of the K1-K3 orthogneiss and the aplite gneiss plus the granite gneiss underlying the laminated scheelite-quartz ores (red). Left: trace element concentrations normalized to values for the upper continental crust (Taylor and McLennan 1995). Right: rare earth element patterns of the respective orthogneisses normalized to chondritic values reported by Boynton (1984).

The spider diagrams furthermore reveal the unambiguous correlation of the granite gneiss underlying the laminated scheelite-quartz ore in the eastern ore field with the aplite gneiss occurring in the western ore field (Fig. 5.5 bottom).

The younger K2 orthogneiss samples taken in this study are compared to the younger K2 orthogneiss data published by Höll and Eichhorn (2000) (Fig. 5.6). Thereby, the orthogneisses could clearly be identified as younger K2 orthogneiss. There are only minor differences between the new and the published data, e.g. in Ta.

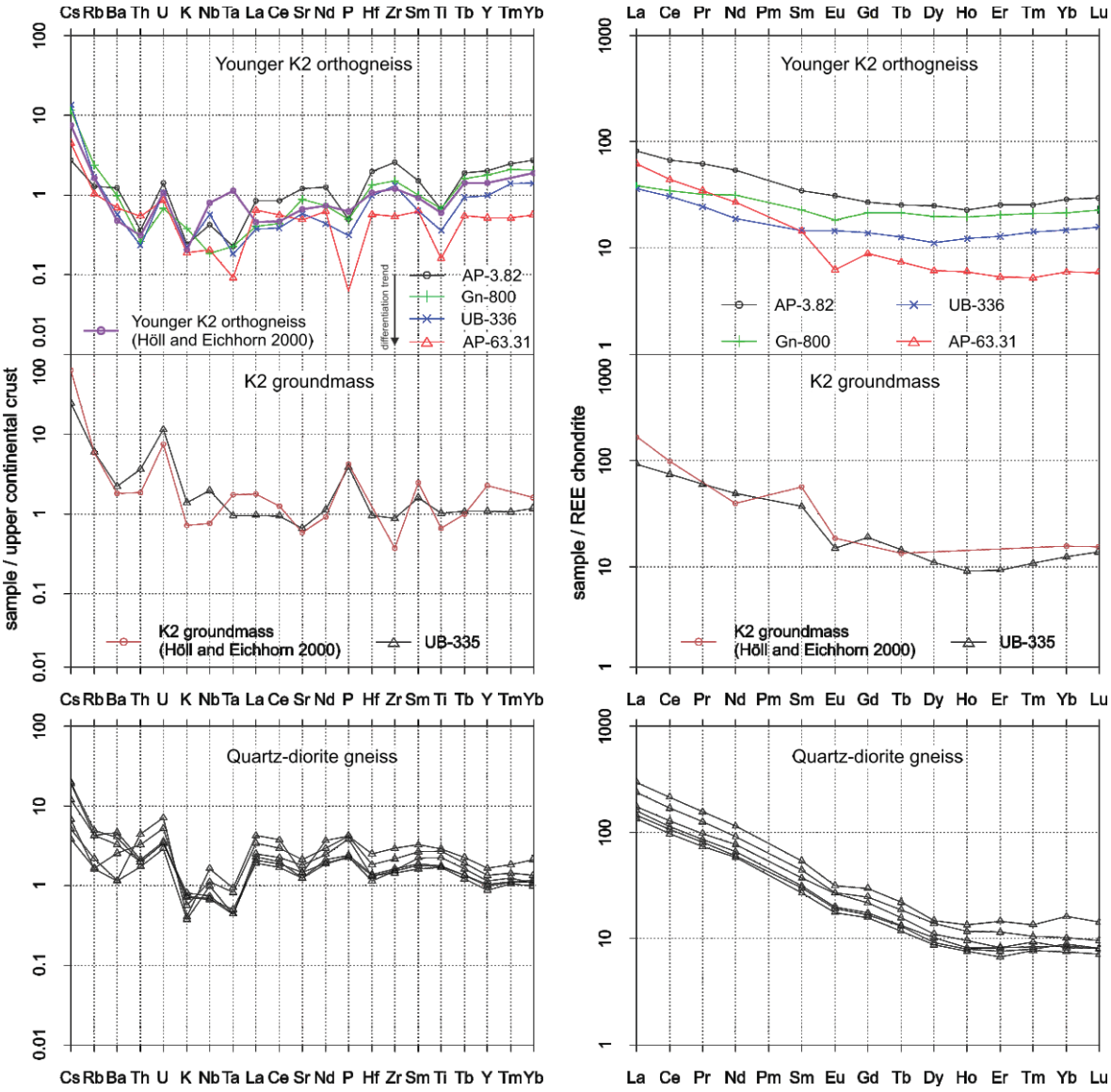

Fig. 5.6 Spidergrams of the younger K2 orthogneiss, K2 groundmass and quartz-diorite gneiss. Left: trace element concentrations normalized to values for the upper continental crust (Taylor and McLennan 1995). Right: rare earth element patterns of the respective orthogneisses normalized to chondritic values reported by Boynton (1984).

The higher Ta content of the Höll and Eichhorn (2000) reference sample is most likely attributed to analytical uncertainties. With progressive differentiation from sample AP-3.82 to AP-63.31 (cf. black arrow), a pronounced decrease in P, Ta, Hf, Zr, Ti, and HREE abundances becomes obvious. Cesium and U are enriched in the younger K2 orthogneiss, comparable to the dark-colored K1-K3 orthogneiss. With respect to the REE-patterns, no Eu-anomaly with the exception of the highest differentiated sample AP-63.31 (Eu/Eu*= 0.55) is developed in the younger K2 orthogneiss. Generally, the REE patterns are characterized by high and decreasing concentrations of LREE with atomic weight (La_N/Yb_N= 1.80-10.49) and flat to slightly increasing HREE (Lu_N/Ho_N= 0.98-1.29).

Samples of the K2 groundmass (UB-335) and samples from Höll and Eichhorn (2000) are compared in figure 5.6. Striking similarities are the positive peaks of Cs, U, P, and Sm. Uranium concentrations are similar to the K1-K3 orthogneiss. The same applies to the REE-pattern of UB-335 that mirrors the trend observed in the K1-K3 orthogneiss with respect to decreasing concentrations from La to Dy and increasing HREE (Lu_N/Ho_N= 1.52). However, the La_N/Yb_N ratio with values of 7.52 and 10.82 is higher in the K2 groundmass. Moreover, only a weak negative Eu-anomaly is developed in UB-335 (Eu/Eu*= 0.56).

The multi-element plots in figure 5.6 reveals slight differences in the chemical composition of the quartz-diorite gneiss. One subgroup is enriched in Cs, Rb and Ba but has lower concentrations of Nb and Ta compared to the second one. The first subgroup of quartz-diorite gneisses shows the highest SiO_2 concentrations (61.06-63.19 mass%). Common features of all quartz-diorite gneisses are their elevated U concentrations and negative Sr- and positive P-anomalies. The REE-plots show enrichment of the LREE compared to the HREE (La_N/Yb_N= 16.19-23.49). Eu/Eu* is between 0.78 and 0.94 denoting a weak negative Eu-anomaly. In contrast to the K1-K3 orthogneiss and the K2 orthogneisses, the quartz-diorite gneisses do not show the increase in HREE (Lu_N/Ho_N= 0.83-1.06).

Zentralgneise

Spidergrams of the various Zentralgneise are shown in figure 5.7. There the compositional range of the dark-colored K1-K3 orthogneiss (grey colored) is additionally shown for better comparison. Striking similarities between the two orthogneisses are their elevated concentrations of U, Nb and Ta, and negative anomalies in Sr and Ti contents. However, the degree of enrichment in U, Nb and Ta is less pronounced in the Felbertauern

augengneiss. The negative Eu-anomaly (Eu/Eu*= 0.27-0.45) is comparable to that of the dark-colored K1-K3 orthogneiss, whereas the HREE display a flatter distribution in the Felbertauern augengneiss (Lu_N/Ho_N= 0.71-1.42).

The multi-element diagram in figure 5.7 reveals some compositional differences between the Granatspitz gneiss and the dark-colored K1-K3 orthogneiss as reflected by lower normalized U, Th, Nb, and HREE values. Contrary, normalized Ba, K, LREE, Sr, P, Ti, and Tb values are in the same range as in the dark-colored K1-K3 orthogneiss. The REE continuously decline from La to Lu and feature a negative Eu-anomaly (Eu/Eu*= 0.40-0.48). The Granatspitz gneiss pattern in figure 5.7 lacks the significant positive peaks in U, Nb and Ta which are characteristic for the K1-K3 orthogneiss. The REE-pattern of the Granatspitz gneiss is in respect of the LREE similar to the dark-colored K1-K3 orthogneiss, but differs significantly in HREE as displayed by low Lu_N/Ho_N (0.78-0.82) and high La_N/Yb_N (9.16-9.55).

The lithological heterogeneity of the Hochweißenfeld gneiss is the cause to subdivide two subgroups (Fig. 5.7). The melanocratic low-SiO_2 gneisses (FB-10/30, FB-11/30M, IG-18/34, IG-19/34) show a uniform distribution with slightly enriched normalized concentrations of P and Ti but depleted Nb and Ta contents. Rare earth element concentrations are relatively high and the corresponding patterns decline towards the HREE with only a minor negative Eu-anomaly (Eu/Eu*= 0.75-0.90). Contrary, the leucucratic gneiss samples (IG-16/34, IG-17/34, FB-34/37, FB-35/37) have distinct negative anomalies in Sr and P compared to the first subgroup and have developed a significant negative Eu-anomaly (Eu/Eu*= 0.48-0.70).

The Knorrkogel gneiss has like the Hochweißenfeld gneiss similar compositions to the upper continental crust with small positive spikes for U and Sr and negative ones for Nb and Ta. Chondritic normalized REE patterns display a strong enrichment of the LREE (La_N/Yb_N= 16.58-37.59) without a significant Eu-anomaly (Eu/Eu*= 0.82-1.11) and low HREE contents.

Indicative of the Weißeneck-Dichtensee gneiss is the depletion in Cs contents and the negative spikes of P and Ti (Fig 5.7). Sample FH-43/47 shows the least negative anomalies of respective elements but displays elevated Ta concentrations. The REE-distribution is comparable to the Felbertauern augengneiss with steep declining LREE and flat HREE (La_N/Yb_N= 8.89-19.05), although the Eu-anomaly is less pronounced in the Weißeneck-Dichtensee gneiss (Eu/Eu*= 0.42-0.71).

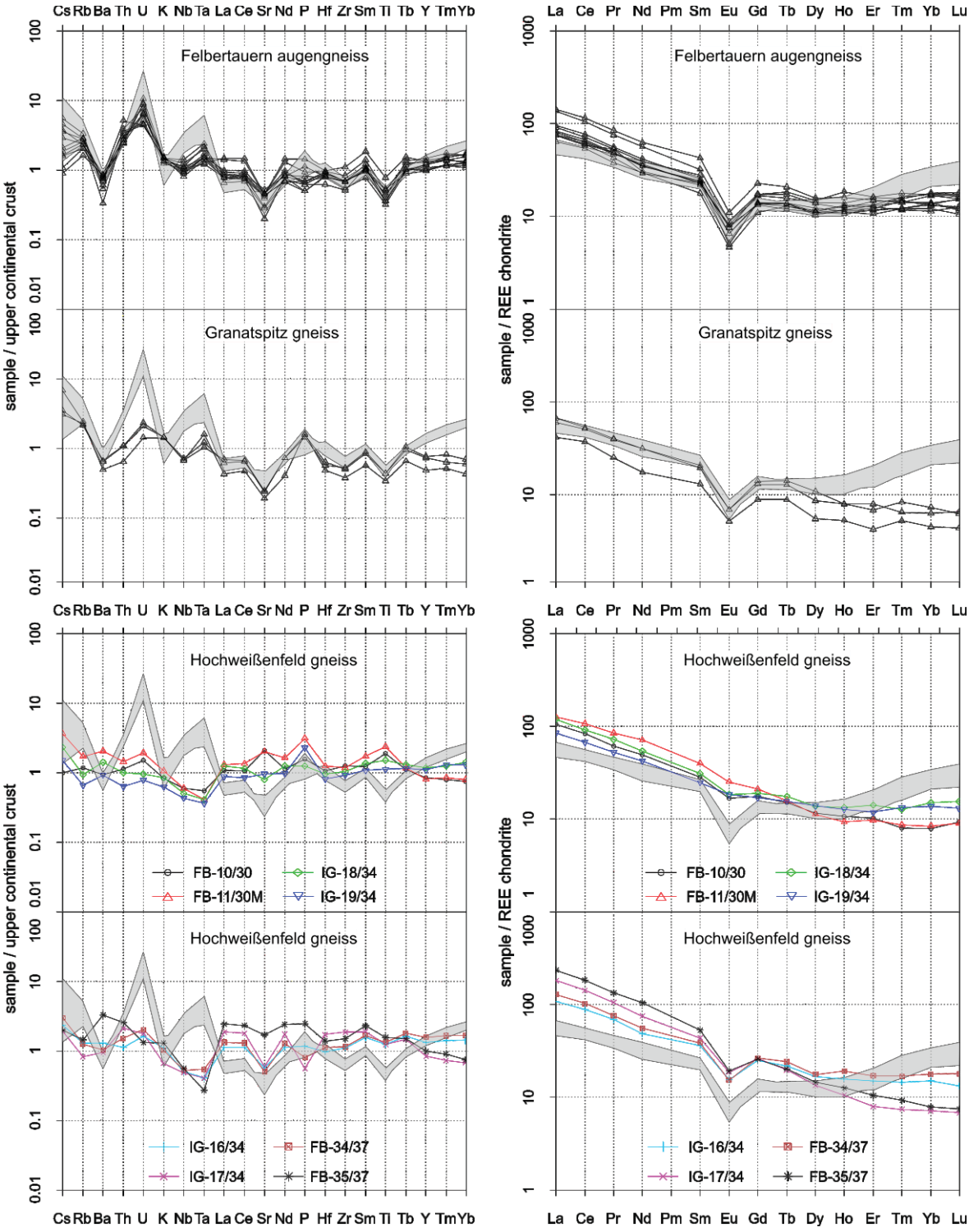

Figure is continued on the next page

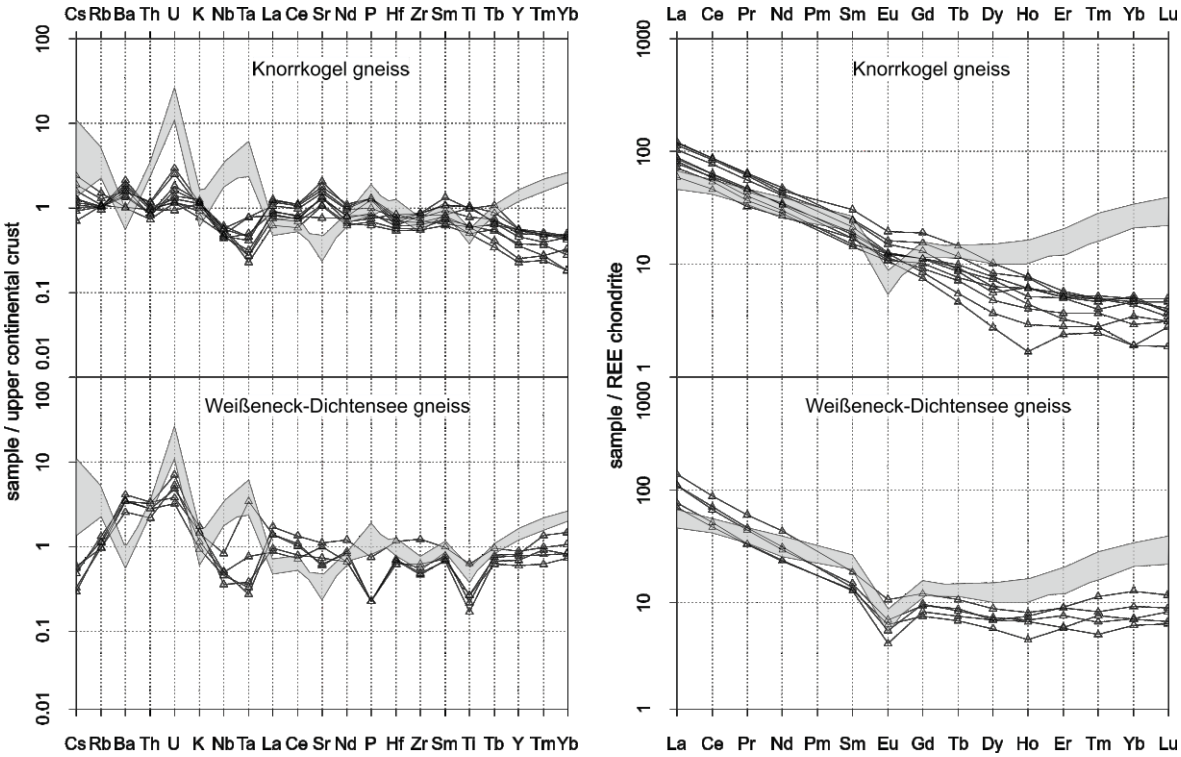

Fig. 5.7 Spidergrams of the Felbertauern augengneiss, Granatspitz gneiss, Hochweißenfeld gneiss, Knorrkogel gneiss, and Weißeneck-Dichtensee gneiss. Left: trace element concentrations normalized to values for the upper continental crust (Taylor and McLennan 1995). Right: rare earth element patterns of the respective orthogneisses normalized to chondritic values reported by Boynton (1984). The grey shaded pattern represents the compositional range of the dark-colored K1-K3 orthogneiss, which is shown for better comparison in all diagrams.

5.2 Mineral chemical analyses

5.2.1 Allanite $(Ca,Mn,LREE,Y,Th)_2(Fe^{2+},Fe^{3+},Ti)(Al,Fe^{3+})_2Si_3O_{12}$ (OH)

Major and trace element concentrations of allanite and surrounding epidote group minerals were measured by EPMA in samples from the dark-colored K1-K3 orthogneiss (Gn-1152a, K1-1100), light-colored K1-K3 orthogneiss (K1-1152), Felbertauern augengneiss (SP-07/30, FB-12/30) and Hochweißenfeld gneiss (FB-35/37). High-contrast BSE photomicrographs reveal complex zoning patterns in allanite, whereby BSE-darker patchy zones generally replace BSE-bright structure-less allanite (Fig. 5.8a-d). Allanite displays tabular to short prismatic euhedral crystals that are always mantled by a corona of epidote-clinozoisite if allanite occurs in the matrix of the orthogneisses (Fig. 5.8c). Allanite occurs as small inclusions without epidote-rims in apatite, zircon and titanite. Conversely, allanite occasionally contains apatite, zircon and thorite inclusions. As a result of elevated contents of Th and U, metamictization of allanite is common. It can be identified by dark-brown colors of the allanite under crossed polarizers in the optical microscope. Recalculation of the mineral formulae was performed following the suggestions of Ercit (2002) and the outline in Spürgin et al. (2009). The A(1) position of the allanite structure is completely filled with Ca^{2+}; excess Ca^{2+} and REE^{3+}, Th^{4+}, Mn^{2+}, Na^{+}, and K^{+} occupies the A(2) position. The M(2) position contains only Al^{3+}, while excess Al^{3+} fills the M(1) position together with Ti^{4+} and Mg^{2+}. The M(3) position accommodates ferrous and ferric iron and the T position contains Si^{4+} and P^{5+}.

	K1-K3 orthogneiss			Felbertauern augengneiss			Hochweißenfeld gneiss		
	core n=11	rim n=5	ep n=3	core n=7	rim n=5	ep n=2	core n=6	rim n=11	ep
SiO_2	32.14	34.69	37.79	33.05	35.19	38.15	33.10	34.00	-
Al_2O_3	15.41	20.56	25.10	14.86	20.37	26.61	17.22	19.50	-
CaO	11.75	16.29	23.79	14.10	19.92	24.83	13.94	15.16	-
REE_2O_3	19.82	6.71	0.51	15.69	7.00	0.28	16.68	15.60	-
FeO_{tot}	14.64	10.36	8.65	13.95	10.96	7.38	11.37	9.88	-
ThO_2	1.38	1.28	nd	1.84	3.71	0.04	2.02	1.66	-
MnO	1.11	0.77	0.11	0.22	0.20	0.09	0.24	0.25	-
MgO	0.34	0.15	0.03	0.42	0.18	0.03	1.41	0.84	-
TiO_2	0.29	0.04	bdl	0.67	0.06	0.08	0.64	0.40	-
Y_2O_3	0.16	0.12	0.07	0.13	0.10	0.02	0.14	0.05	-
UO_2	0.04	0.28	0.22	0.08	0.16	0.08	0.04	0.06	-

Tab. 5.2 Median elemental concentrations in mass% of allanite-(Ce) cores and rims and surrounding epidote (ep); n= number; nd= not detected, bdl= below detection limit; FeO_{tot}= $FeO+Fe_2O_3$.

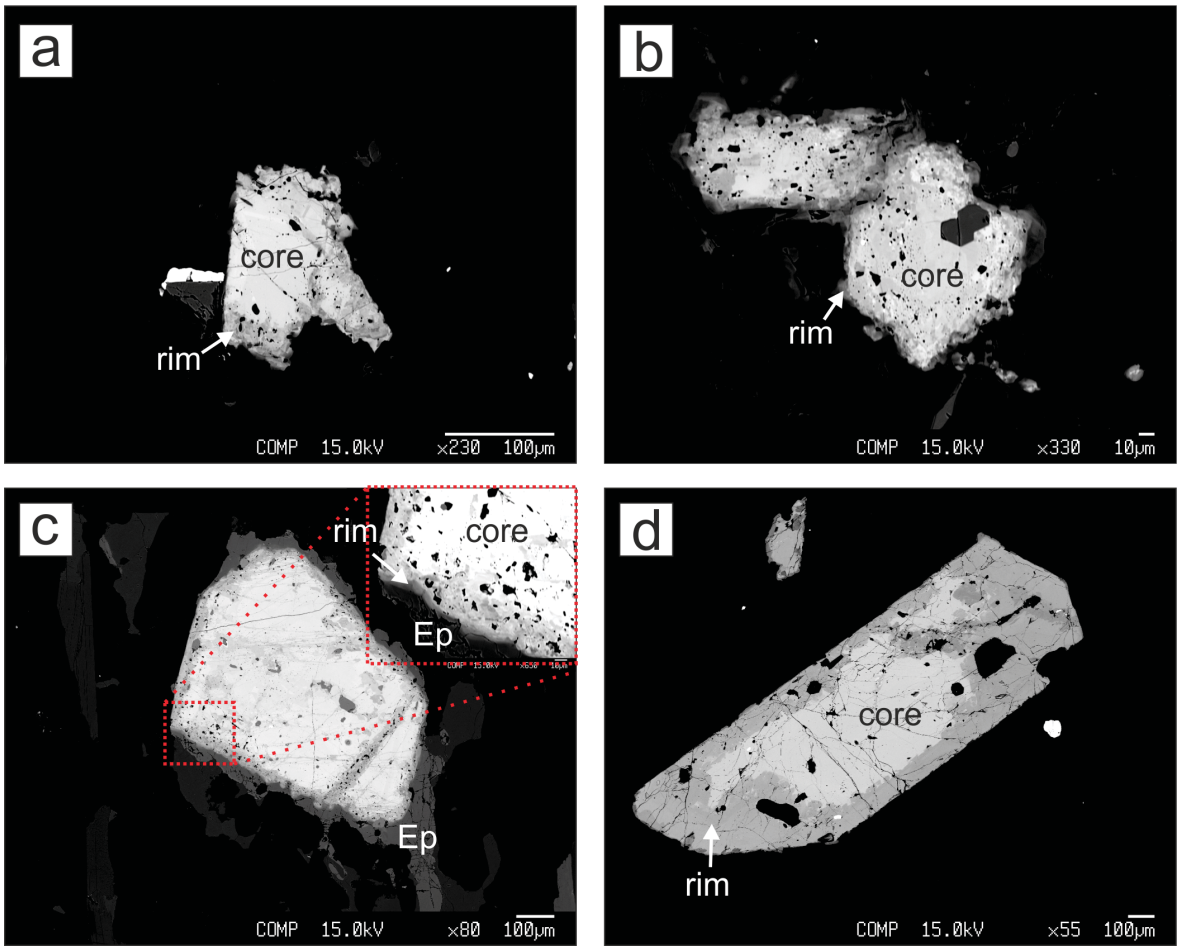

Fig. 5.8 BSE photomicrographs of zoned allanite; Ep= epidote. **a)** Dark-colored K1-K3 orthogneiss (K1-1100). **b)** Light-colored K1-K3 orthogneiss (K1-1152). **c)** Felbertauern augengneiss (SP-07/30). **d)** Hochweißenfeld gneiss (FB-35/37).

Overall, 28 elements including selected REE (La, Ce, Pr, Nd, Sm, Gd, Tb, Yb) were analyzed in allanite. The complete data set is available in Appendix E.1; median compositions according to textural criteria and lithologies are reported in Table 5.2. No chemical differences in allanite from the dark-colored and the light-colored K1-K3 orthogneiss varieties exist; therefore analyses are pooled together in the tabular presentation. Cerium is the dominant LREE in allanite with concentrations <12.5 mass% Ce_2O_3 (≡ 0.46 Ce apfu), by what allanite is classified as allanite-(Ce). Analytical totals are low and range between 95.74 and 98.62 mass% (median 97.35 mass%), either due to the appearance of vacancies or incorporation of OH^-groups in allanite (Poitrasson 2002).

Generally, REE concentrations decrease in all samples from the allanite-(Ce) core domains towards the rims; surrounding epidotes are virtually free of REE. Simultaneously, MgO, FeO_{tot}, TiO_2, and MnO decrease, whereas Al_2O_3, CaO and SiO_2 contents increase, occupying the vacant M(2), A(2) and T positions. Uranium concentrations tend to increase

from core to rim domains, while ThO_2 shows no clear trend. With respect to the various lithologies, allanite-(Ce) cores from the K1-K3 orthogneiss feature the highest REE_2O_3 concentrations and consequently the lowest CaO contents. Furthermore, MnO in allanite-(Ce) is significantly higher in the K1-K3 orthogneiss compared to the Felbertauern augengneiss and Hochweißenfeld gneiss. On the contrary, allanite-(Ce) cores from the Zentralgneise are slightly enriched in TiO_2. Cores of allanite-(Ce) from the Hochweißenfeld gneiss are significantly different from the K1-K3 orthogneiss and Felbertauern augengneiss due to their higher MgO and lower FeO_{tot} concentrations.

Figure 5.9a displays the chemical variation of allanite-(Ce) on the M(1) and M(3) positions. Most analyses scatter between Fe^{2+} and the trivalent Al^{3+} and Fe^{3+} cation endmembers, illustrating their close chemical affinity with allanite and epidote endmembers. Analyses of allanite-(Ce) from the Hochweißenfeld gneiss are clearly more magnesian and shifted towards the Mg-equivalent of allanite (dissakisite).

The chemical variation of allanite-(Ce) in the studied samples can be summarized by the chemical exchange vector (Fig. 5.9b):

(1) $Ca^{2+} + Al^{3+} + Fe^{3+} \leftrightarrow Fe^{2+} + Mg^{2+} + Ti^{4+} + REE^{3+} + Y^{3+} + Mn^{2+} + U^{4+} + Th^{4+}$

(Peterson and MacFarlane 1993).

Accordingly, allanite-(Ce) shows a progressive transition into a more epidote-like composition towards the rims, replacing primary allanite-(Ce). Analyses of the surrounding epidote-corona plot in the lower right corner close to the epidote endmember in figure 5.9b.

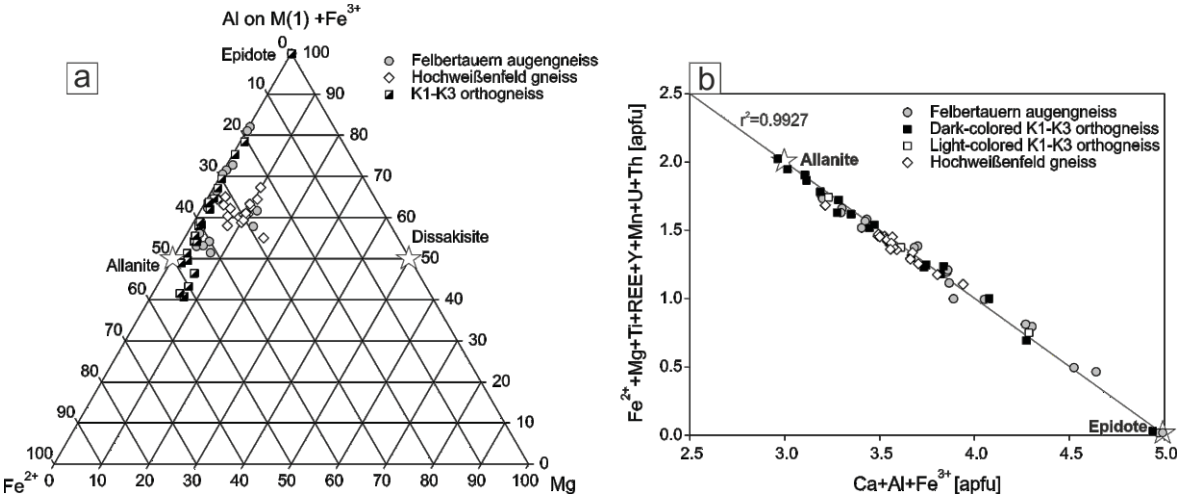

Fig. 5.9 Chemical variation of epidote-group minerals. **a)** Variation in M(1) and M(3) sites. **b)** Cationic plot showing the substitution mechanism (1) occurring in allanite-(Ce).

5.2.2 Apatite $Ca_5(PO_4)_3$ (OH,F,Cl)

Apatites from the K1-K3 orthogneiss were analyzed in samples K1-725, K1-1152, K1-1234, Gn-1152a, and Gn-1065b. Apatite analyses from the Felbertauern augengneiss are from FB-12/30; SP-28/34 and FB-33/34. The complete data record is available in Appendix E.2. The major and trace element composition of apatite was determined by EPMA at Montanuniversität Leoben. Mineral formulae were recalculated on the basis of 10 cations according to Ulmer (1993). Additionally, a comprehensive suite of trace elements including the REE was analyzed by LA-ICP-MS at Johann Wolfgang von Goethe University Frankfurt.

As high-contrast BSE photomicrographs reveal, apatites from the K1-K3 orthogneiss (Fig. 5.10a) and the Felbertauern augengneiss (Fig. 5.10b-c) show typical core-rim textures, indicative of multi-stage growth of apatite. Generally, a euhedral to subhedral core domain is overgrown by a BSE-dark anhedral apatite rim, whereby two distinct core domains can be distinguished according to the intensity of the BSE signal. The inner core zone (core 1) displaying a similar shade of grey as the apatite rim is overgrown by a second, BSE-brighter core domain (core 2; Fig. 5.10a-c). Occasionally, the core 2 zones reveal oscillatory zoning and irregular boundaries towards the core 1 domains (Fig. 5.10a). Usually, the core 2 domain likewise features partly indented boundaries towards the anhedral rim. Moreover, BSE-dark anhedral and unzoned apatites occur in both the K1-K3 orthogneiss and the Felbertauern augengneiss. Apatite frequently appears as small (~10 µm) unzoned euhedral prismatic inclusions in zircon, titanite and allanite (Fig. 5.10d). Usually, apatite occurs associated with metamorphic muscovite, biotite, albite, calcite, fluorite or epidote.

EPMA analyses

According to the EPMA analyses (see Appendix E.2.1), apatites from the K1-K3 orthogneiss and the Felbertauern augengneiss belong to the group of fluor-hydroxy apatites, with F as the dominant anion (XF=F/(F+OH+Cl)= 0.50-1.00); chlorine contents were constantly below the detection limit. Fluorine concentrations generally range between 2.16 mass% and 4.26 mass% F in the K1-K3 orthogneiss. A systematic variation between F contents of core domains and apatite rims was not observed, also not between apatites from the dark-colored and the light-colored K1-K3 orthogneiss variety. Thus, no systematic increase in F concentrations with increasing magmatic differentiation is to be seen in apatite.

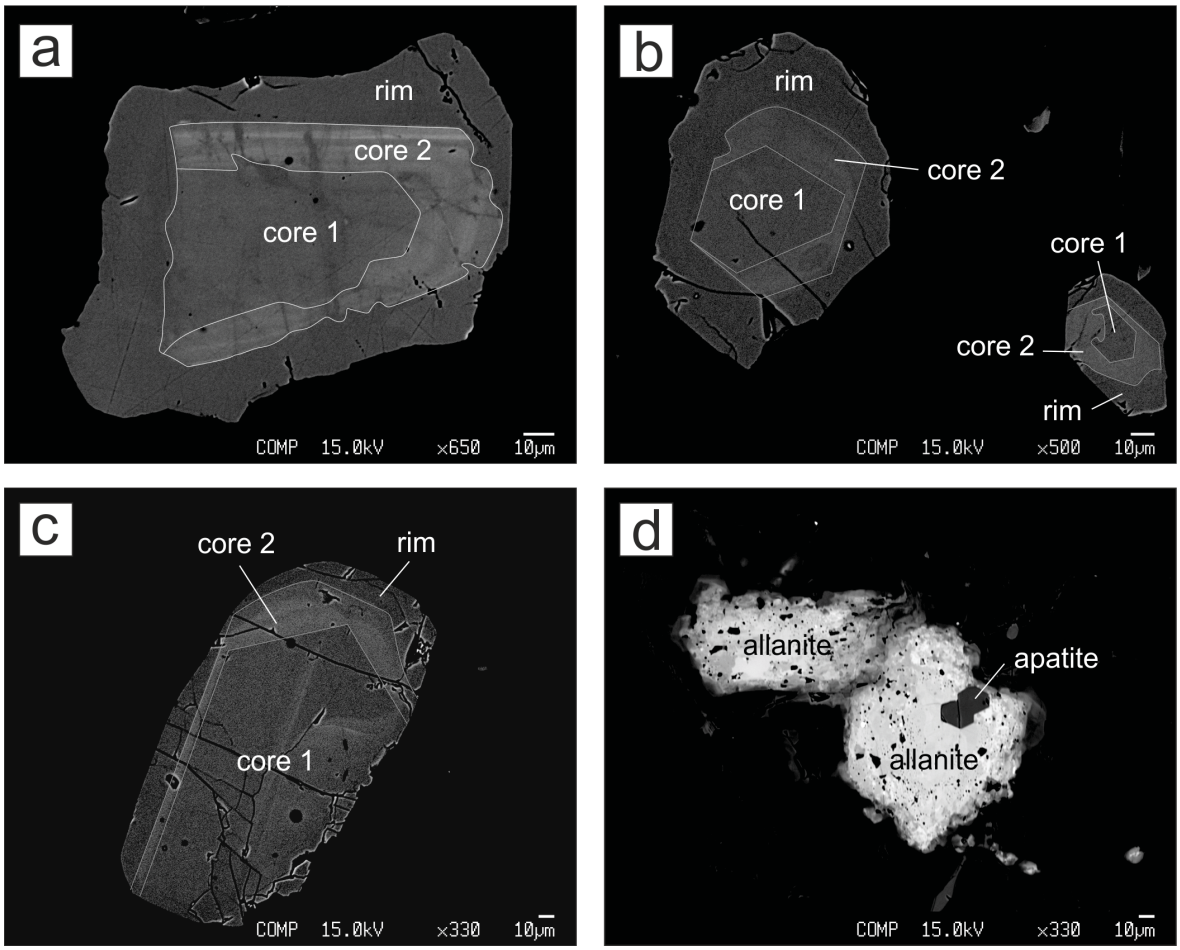

Fig. 5.10 BSE photomicrographs of apatites from the K1-K3 orthogneiss and Felbertauern augengneiss. Thin white lines emphasize the individual apatite domains. **a)** Two core generations overgrown by an anhedral rim can be clearly distinguished in apatites from the light-colored K1-K3 orthogneiss sample K1-1234. A BSE-dark inner core domain (core 1) is overgrown by an oscillatory zoned BSE-bright outer core domain (core 2). Both core zones feature partly indented boundaries. Note the BSE-darker healed cracks crosscutting the cores. **b-c)** Similar apatite domains occur in the Felbertauern augengneiss sample FB-12/30. Both apatites show partly intended boundaries between growth zones, yet less pronounced as in the K1-K3 orthogneisses. **d)** Unzoned hexagonal apatite inclusions in allanite; light-colored K1-K3 orthogneiss sample K1-1152.

The analytical results show little variation in the major structural components CaO and P_2O_5, ranging from 54.7 to 56.5 mass% CaO and from 40.3 to 41.7 mass% P_2O_5, respectively. Concentrations of S, Fe, Mg, and Mn were generally not detected or below/near the EPMA detection limit, not giving any reliable information on the petrogenetic evolution of apatite.

Apatite from the Felbertauern augengneiss has F concentrations similar to the K1-K3 orthogneiss scattering between 1.84 mass% and 4.40 mass% F, whereby again no systematic trend was detected in F abundances. The concentrations of CaO (40.6-42.3 mass% CaO) and P_2O_5 (54.3-56.5 mass% P_2O_5) in apatite from the Felbertauern augengneiss are also comparable to the K1-K3 orthogneiss.

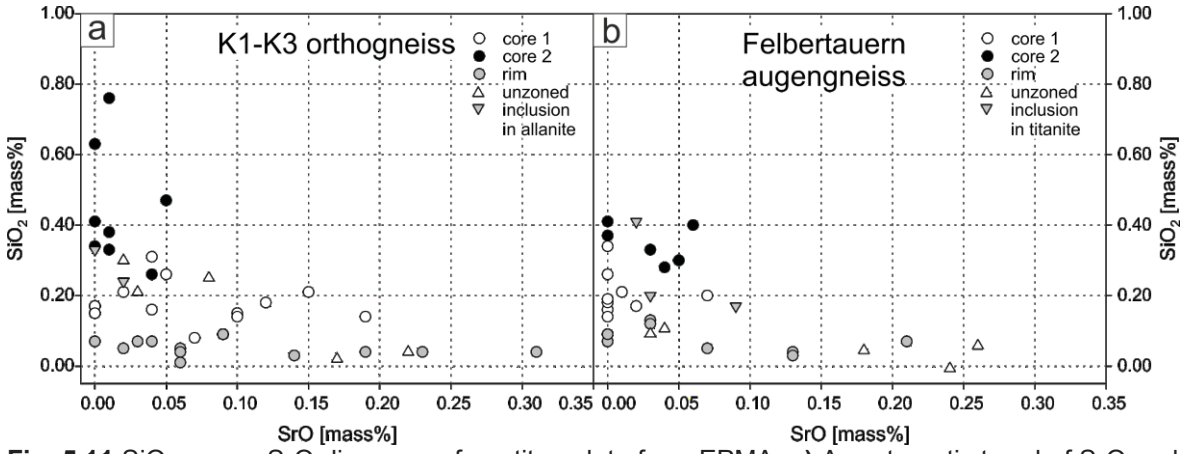

Fig. 5.11 SiO_2 versus SrO diagrams of apatites; data from EPMA. **a)** A systematic trend of SrO and SiO_2 occurs in apatites from the K1-K3 orthogneiss. The core 2 domains display high SiO_2 concentrations but low SrO, while apatite rims yield higher SrO concentrations and low SiO_2 contents. The inner core 1 zones show intermediate chemical compositions. **b)** The same systematics is found in apatites from the Felbertauern augengneiss.

A systematic trend is observed in the SiO_2 and SrO concentrations of apatite domains in the K1-K3 orthogneiss and the Felbertauern augengneiss (Fig. 5.11a-b). In the K1-K3 orthogneiss, the BSE-bright second core domain (core 2) shows the highest SiO_2 contents ranging from 0.26 to 0.76 mass% SiO_2 at constantly low SrO concentrations <0.05 mass% SrO, usually below the detection limit of EPMA (Fig. 5.11a). On the contrary, the anhedral apatite rims yield more variable chemical compositions with generally elevated SrO concentrations between 0.04 mass% and 0.31 mass% SrO and low SiO_2 concentrations (<0.09 mass% SiO_2). Analyses of the internal apatite zones (core 1) give intermediate element compositions (0.04-0.19 mass% SrO; 0.08-0.21 mass% SiO_2). The chemical analyses reveal that most unzoned apatites correspond to the apatite rims with respect to the abundances of SiO_2 and SrO, whereby few apatites show chemical characteristics comparable to the core 1 domains. Apatite inclusions in allanite match rather apatite core 1 than core 2 domains according to their SiO_2 and SrO concentrations. Apatites from the Felbertauern augengneiss show the same clustering of the data though in numerous analyses SrO was below the detection limit (Fig. 5.11b).

LA-ICP-MS analyses

Based on the spatial resolution of LA-ICP-MS trace element analyses it was not possible to separately analyze the two apatite core domains. The apatite core 2 zone is only 10 µm thick while the laser beam used for ablation was 33 µm in diameter. Consequently, only core and rim domains could be distinguished. However, the results similarly reveal two distinct types of cores and one rim type in the K1-K3 orthogneiss that cannot be discerned in BSE and CL images. Interestingly, both types of apatite cores occur in the dark-colored as well as in the light-colored K1-K3 orthogneiss variety and may be found within the same sample (e.g. K1-1152).

The trace element analyses show that there are chemical differences between apatite cores from the dark-colored and the light-colored K1-K3 orthogneiss as well as between apatites from individual samples (Fig. 5.12a-b). Apatites reveal a systematic trend in the concentration of actinides. Higher concentrations in the range of 24-40 ppm U and 40-70 ppm Th were analyzed in the core domains of the light-colored K1-K3 orthogneiss (Fig. 5.12a). Uranium and Th contents of apatite cores in the dark-colored variety are lower (16-20 ppm U, 25-36 ppm Th; one outlier with 53 ppm U and 111 ppm Th). The apatite rims in the K1-K3 orthogneisses generally yield the lowest concentrations in the range of 0.8-7.9 ppm U and 0.8-13 ppm Th. A similar pattern was observed in apatites from the Felbertauern augengneiss with U concentrations in apatite cores corresponding to the range observed in the dark-colored K1-K3 orthogneiss apatites. One single apatite rim analysis gives concentrations of 12 ppm U and 13 ppm Th.

The two apatite core types can be best identified by their distinct Sr concentrations and negative Eu-anomalies (Eu/Eu*), whereby values for Eu/Eu* range between 0.1 and 0.5 (Fig. 5.12b). Higher Sr concentrations in apatite cores, ranging between 1050 ppm and 1480 ppm Sr, correlate with less pronounced negative Eu-anomalies (Eu/Eu*= 0.44-0.52). On the contrary, apatite cores with significant negative Eu-anomalies and low Eu/Eu* (0.16-0.30) show low Sr concentrations (238-604 ppm Sr). In addition, apatite rims can be analogously subdivided in a group with high Sr concentrations (1126-1498 ppm Sr) and high Eu/Eu* (0.29-0.42) and in apatite rims showing low Sr concentrations ranging between 217 ppm and 414 ppm Sr and low Eu/Eu* values between 0.09 and 0.21.

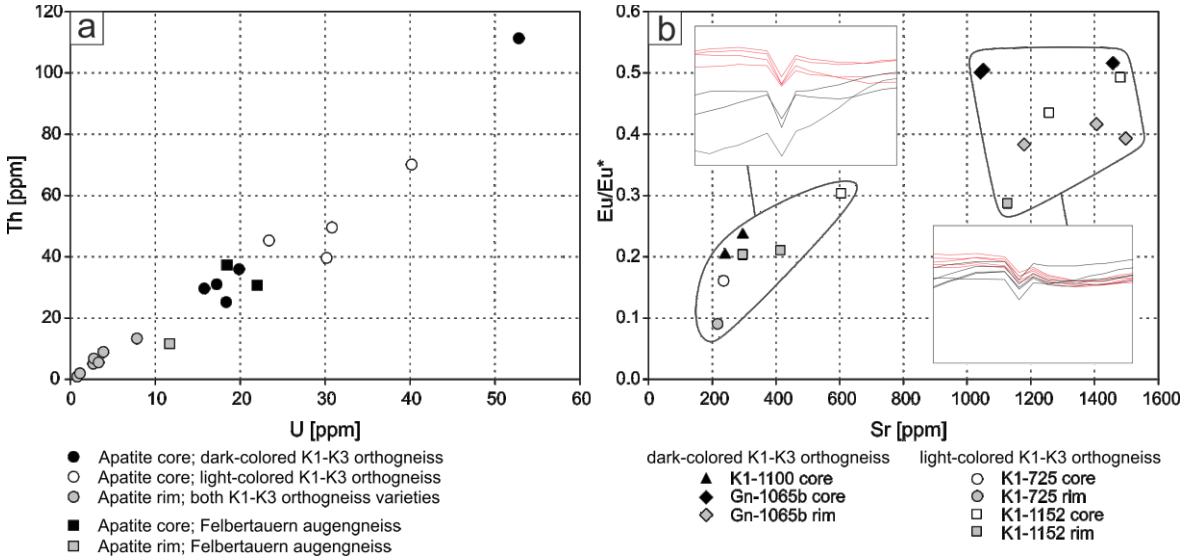

Fig. 5.12 a) U versus Th diagram for apatites from the K1-K3 orthogneiss and the Felbertauern augengneiss. Apatite cores from the light-colored K1-K3 orthogneiss show higher U and Th concentrations compared to the dark-colored variety (apart from one outlier). Apatite rims have low actinide contents. Uranium concentrations of apatites from the Felbertauern augengneiss correspond to apatites from the dark-colored K1-K3 orthogneiss. **b)** Two apatite types can be distinguished in the K1-K3 orthogneiss.

The chondrite-normalized REE-patterns of apatite cores from the K1-K3 orthogneiss show a flat to sometimes slightly upward-convex distribution of the LREE (Fig. 5.13a). All apatites with high Sr concentrations and high Eu/Eu* values obviously display significantly low MREE (Gd-Dy) concentrations and slightly positively inclined HREE concentrations. A similar pattern for the MREE and HREE is observed in apatite cores with low Sr concentrations and Eu/Eu* values, although two analyses yield significant elevated MREE and HREE contents.

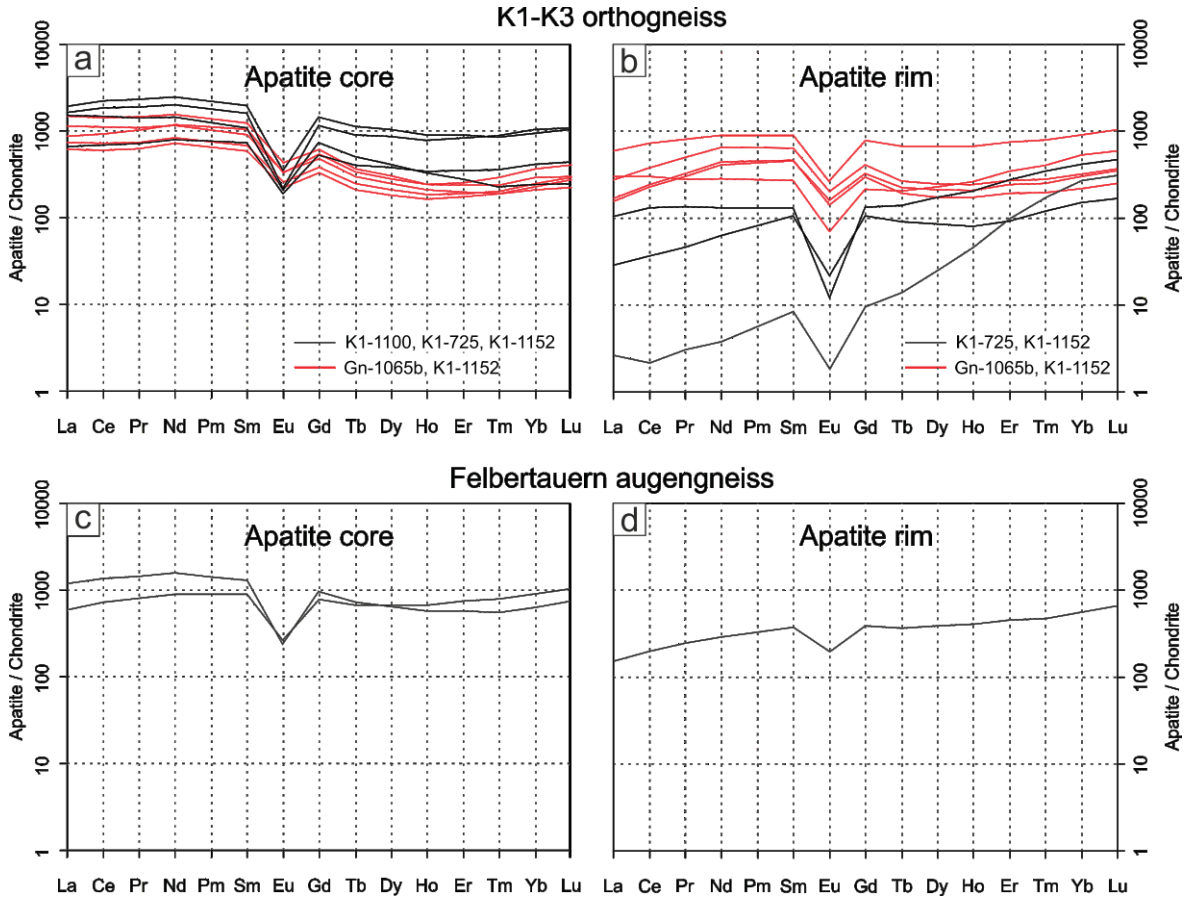

Fig. 5.13 REE-patterns of apatites from the Felbertal scheelite deposit and the Felbertauern augengneiss. **a)** Apatite cores, K1-K3 orthogneiss. Black lines correspond to low Sr-apatites and red lines high Sr-apatite; dark-colored K1-K3 orthogneiss samples K1-1100, Gn-1065b and light-colored K1-K3 orthogneiss samples K1-725 and K1-1152. **b)** Apatite rims (color coding equally to Fig. 5.13a). Rims generally have lower LREE contents; samples K1-725, K1-1152, Gn-1065b. **c)** Two apatite cores from the Felbertauern augengneiss sample SP-25/34 showing a similar REE distribution as the K1-K3 orthogneiss. **d)** Depletion of LREE in apatite rim of sample SP-25/34 is similar to that shown in b.

Generally, total REE concentrations are relatively low in both apatite core domains, while REE abundances in the apatite type with the more pronounced Eu-anomaly are slightly higher (median REE= 4170 ppm) compared to the group of apatite cores with higher Eu/Eu* (median REE= 2500 ppm; Appendix E.2.2). The normalized REE-patterns of the apatite rims from the K1-K3 orthogneiss are quite variable (Fig. 5.13b), although there is no evidence for mineral inclusions (e.g. zircon, titanite) which could affect the analyses. The chondritic-normalized REE patterns of apatite rims generally show a significant depletion of LREE from La to Nd and similar MREE plus HREE patterns compared to the cores. Total REE concentrations of the rims are considerably lower and range between 85 ppm and 1363 ppm REE. Both analyses of apatite cores from the Felbertauern augengneiss show a flat chondrite-normalized REE-pattern with negative

Eu-anomaly (Fig. 5.13c). The corresponding apatite rim clearly shows the same depletion in the LREE as observed in the K1-K3 orthogneiss apatite rims (Fig. 5.13d).

5.2.3 Biotite $K(Mg,Fe^{2+})_3AlSi_3O_{10}(OH,F)_2$

Biotite compositions were measured in the dark-colored K1-K3 orthogneiss (Gn-1152a, Gn-1065b, B-K1d-a, C-K1d-b, K1-1100), light-colored K1-K3 orthogneiss (K1-1152, K1-1234, B-K1h, C-K1h-a), younger K2 orthogneiss (K2-1005b), fine-grained amphibolite (K2-1005M, SE-1050a), Felbertauern augengneiss (FB-12/30, SP-07/30, FB-33/34), Granatspitz gneiss (FB-08/30), Knorrkogel gneiss (FB-09/30), Hochweißenfeld gneiss (FB-10/30, FB-11/30L), and Weißeneck-Dichtensee gneiss (FH-47/37). Analyses were recalculated on the basis of 10 oxygens, 8 cations and 2 OH groups according to Ulmer (1993). The complete data set is available in Appendix E.3. A classification of biotite conferring to the annite-phlogopite-siderophyllite-eastonite quadrilateral is shown in figure 5.14 in which atoms per formula units (apfu) of total aluminum ($^{IV}Al+^{VI}Al$) are plotted versus *X*Fe [Fe/(Fe+Mg)].

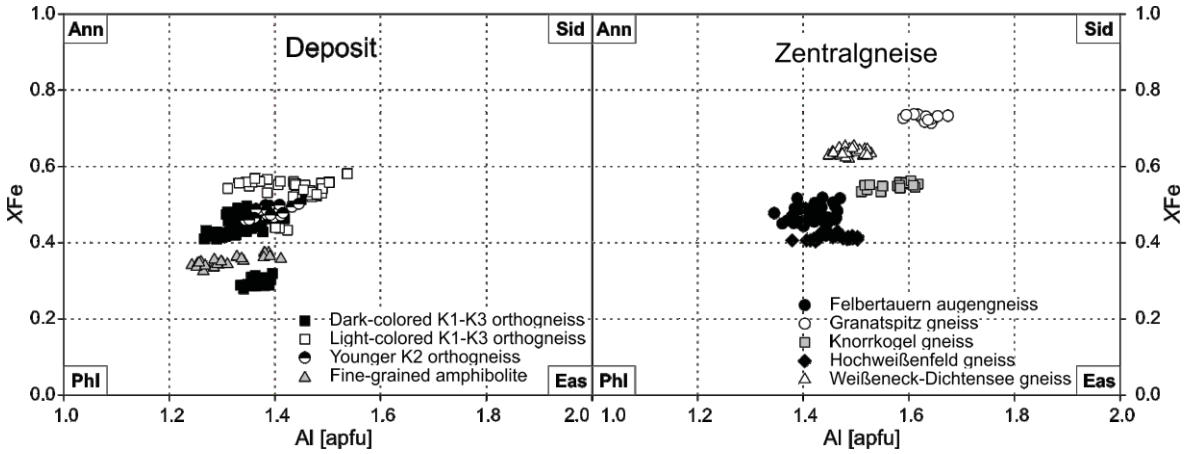

Fig. 5.14 Total Al [apfu] vs. XFe [Fe/(Fe+Mg)] diagram showing the composition of biotite; biotite end-members: Ann= annite, Phl= phlogopite, Sid= siderophyllite, Eas= eastonite.

Biotite from the K1-K3 orthogneiss and the younger K2 orthogneiss has *X*Fe values in the range of 0.40-0.58. The quadrilateral portrays a significant natural variation in biotite compositions of the distinct lithologies at Felbertal. Biotite from the younger K2 orthogneiss is similar to the dark-colored K1-K3 orthogneiss, whereas biotite from the fine-grained amphibolites has lower *X*Fe. Biotite from the dark-colored K1-K3 orthogneiss and the younger K2 orthogneiss follow a slightly positive inclined linear trend from phlogopite towards the siderophyllite endmember, characteristic for biotite of calc-alkaline plutonic rocks (Mason 1978; Rasmussen and Mortensen 2013). On the contrary, biotite from the

light-colored K1-K3 orthogneiss variety defines a horizontal trend of variable Al but at constant *X*Fe, similar to biotite from barren Zentralgneise. Two outlying compositional populations (C-K1d-b, dark-colored K1-K3 orthogneiss; B-K1h, light-colored K1-K3 orthogneiss) yield significantly lower *X*Fe compared to their corresponding cluster.

Similar values were observed in biotite from the Felbertauern augengneiss, Hochweißenfeld gneiss and Knorrkogel gneiss; however, biotite from the Zentralgneise generally tends to have higher Al-contents (1.35-1.67 Al apfu) what is consistent with the peraluminous character of the Zentralgneise (chapter 5.1.2). Biotite from the Weißeneck-Dichtensee gneiss and the Granatspitz gneiss is characterized by the highest *X*Fe ranging between 0.62 and 0.74. The chemical composition of syn-tectonic biotite (grown parallel to the schistosity) is identical to that of post-tectonically grown biotite (overgrowing the existent foliation).

Figure 5.15 shows biotite compositions for individual samples and lithologies. Regarding biotite from the Felbertal scheelite deposit, it is possible to specify some differences. Generally, biotite from the dark-colored K1-K3 orthogneiss shows higher values of *X*Mg [Mg/(Fe+Mg)] ranging between 0.49 and 0.59 compared to the light-colored K1-K3 variety with *X*Mg between 0.43 and 0.48. The dark-colored K1-K3 orthogneiss C-K1d-b shows even higher *X*Mg ranging between 0.68 and 0.72. Additionally, sample B-K1h displays higher *X*Mg (0.54-0.56) than biotite from other light-colored K1-K3 orthogneiss samples.

Generally, biotite from the K1-K3 orthogneiss shows low Na_2O abundances <0.10 mass%, analogous to biotite from the younger K2 orthogneiss. The higher concentrations of Na_2O in biotite from sample C-K1d-b are comparable to the fine-grained amphibolites. A significant difference between biotite from the K1-K3 and younger K2 orthogneiss exists in the BaO contents. Biotite from the younger K2 orthogneiss and the fine-grained amphibolite is characterized by higher amounts of BaO ranging between 0.07 mass% and 0.60 mass%, while biotite from the K1-K3 orthogneiss consistently has BaO concentrations <0.18 mass%. The most obvious chemical differences between the considered lithologies exist in the F concentration of biotite.

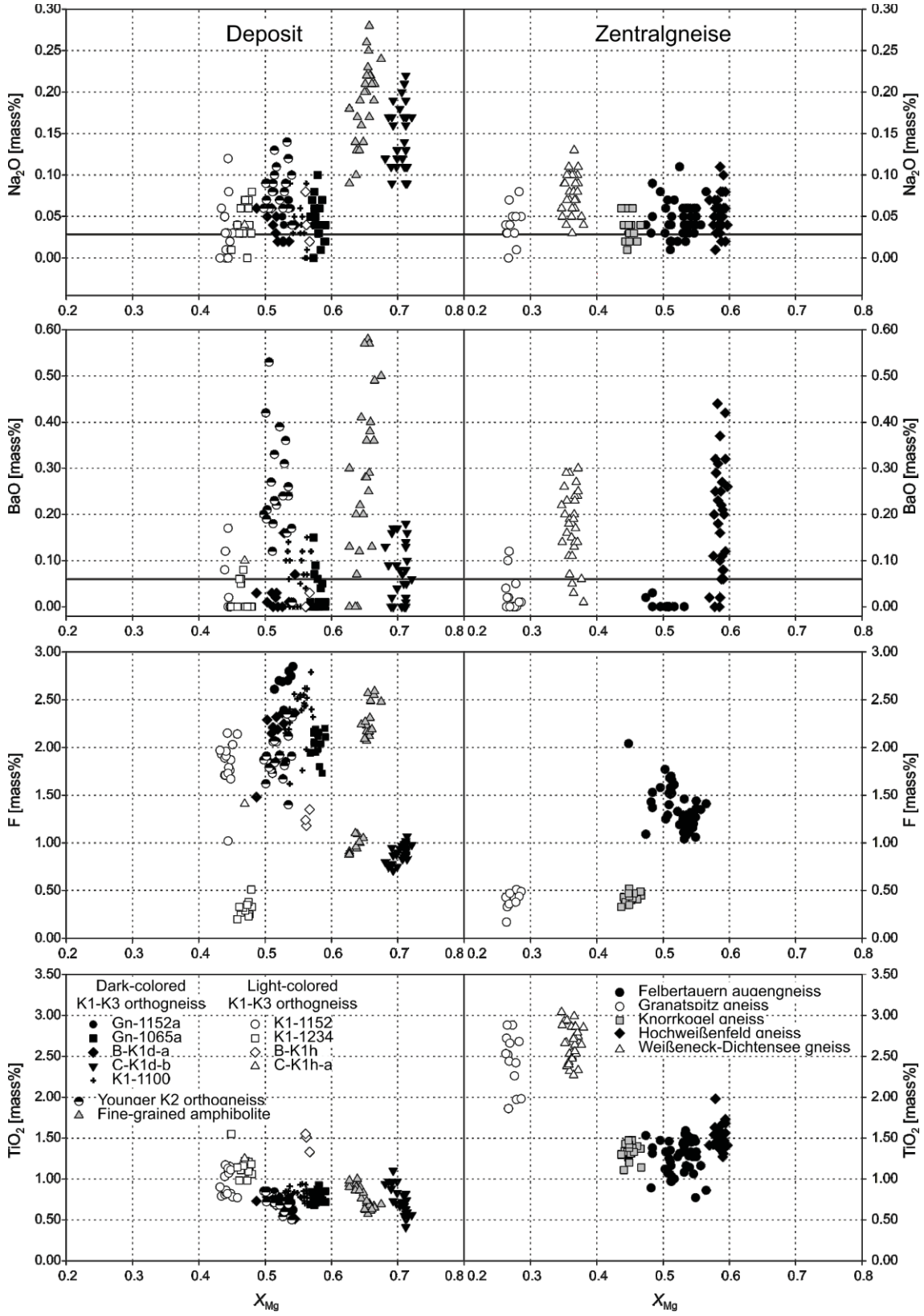

Fig. 5.15 Chemical composition of biotites from various lithologies of the Felbertal scheelite deposit and Zentralgneise shown in x-y diagrams with XMg [Mg/(Fe+Mg)] on the x-axis. The heavy horizontal lines correspond to the detection limit of EPMA.

High F concentrations were analyzed in the dark-colored K1-K3 orthogneiss variety ranging between 1.48 and 2.85 mass% F; again, sample C-K1d-b is outstanding due to low F contents <1.10 mass%. Biotite from the light-colored K1-K3 orthogneiss variety shows generally lower F concentrations <2.15 mass%, though clusters with varying F contents are discernible. The lowest F contents were measured in the light-colored K1-K3 gneiss sample K1-1234 with concentrations below 0.50 mass% F. A positive linear correlation between the F content and *X*Mg is observed in all low-F biotite clusters (<1.10 mass% F); however, most biotites with F concentrations >1.10 mass% show no significant correlation. An exception is sample Gn-1152a, showing the highest observed F concentrations that increase with increasing *X*Mg. Equal high F concentrations as observed in the dark-colored K1-K3 orthogneiss occur in biotite from the fine-grained amphibolite sample K2-1005M (2.07-2.59 mass% F). On the contrary, biotite from sample SE-1038a features generally low F concentrations <1.10 mass%, analogous to the dark-colored K1-K3 orthogneiss sample C-K1d-b. The F contents of biotite from the younger K2 orthogneiss are within the range of the light-colored K1-K3 orthogneiss.

Concentrations of TiO_2 are commonly low in biotite from the Felbertal scheelite deposit (<1.50 mass% TiO_2). A distinct negative correlation between TiO_2 and *X*Mg exists in biotite from both the dark-colored K1-K3 orthogneiss variety and the fine-grained amphibolites, which is not evident in biotite from the light-colored K1-K3 orthogneiss.

Biotite from the Zentralgneise shows significant variations in *X*Mg, BaO, F, and TiO_2 (Fig. 5.15). Biotite from the Weißeneck-Dichtensee gneiss features slightly elevated Na_2O contents of up to 0.13 mass%; apart from that, Na_2O abundances are generally low. A large scatter in BaO concentrations exists in the Weißeneck-Dichtensee gneiss (0.06-0.30 mass% BaO) and in the Hochweißenfeld gneiss (0.06-0.44 mass% BaO), whereas Ba contents in biotite from the Felbertauern augengneiss and Granatspitz gneiss are below the detection limit; Ba was not detected in biotites from the Knorrkogel gneiss.

Biotite from the Felbertauern augengneiss shows the highest F concentrations of the Zentralgneise (0.53-2.04 mass% F). The F concentrations in biotite from the Knorrkogel gneiss and Granatspitz gneiss are below 0.55 mass% F, while no F was detected in biotite from the Hochweißenfeld gneiss and Weißeneck-Dichtensee gneiss. According to the TiO_2 contents, the Granatspitz gneiss and the Weißeneck-Dichtensee gneiss yield elevated concentrations between 1.86 and 3.04 mass% TiO_2. Biotites from the Felbertauern augengneiss, Knorrkogel gneiss and Hochweißenfeld gneiss show lower contents ranging from 0.77 to 1.98 mass% TiO_2.

5.2.4 Pyrochlore supergroup $A_{2-m}B_2X_{6-w}Y_{1-n}$

The general formula of the pyrochlore supergroup is $A_{2-m}B_2X_{6-w}Y_{1-n}$ (Atencio et al. 2010). The A-position is mainly occupied by Na^{+}; Ca^{2+}, Pb^{2+}, Y^{3+}, U^{4+}, Th^{4+}, or H_2O-molecules. The B-position accommodates the high field strength elements Nb^{5+}, Ta^{5+}, Zr^{4+}, Hf^{4+} but also Ti^{4+}, Sn^{4+} and W^{6+}. Oxygen is mainly hosted by the X-position, but also F^{-} and subordinate OH^{-} may be incorporated. The occupancy of the Y-position is variable with OH^{-}, O^{2-}, F^{-}, or large monovalent cations such as K or Rb. The symbols *m*, *w* and *n* indicate possible vacancies at the A-, X- and Y-positions, while the B-site is permanently fully occupied (Borodin and Nazarenko 1957).

The occurrence of (Y,REE,U,Th)-(Nb,Ta,Ti) oxide minerals (pyrochlore) in the Felbertal scheelite deposit is, to the state of knowledge, restricted to quartz-scheelite veins. EPMA analyses of these minerals were performed on respective grains of sample A-K1q-c. The complete data set is available in Appendix E.4. Microscopic investigation and BSE photomicrographs reveal two stages of Nb-Ta-Ti oxide growth, indicated by core-rim textures with inclusion rich internal domains and inclusion-free rims (Fig. 5.16a-b). The Nb-Ta-Ti oxides are associated with scheelite, molybdenite, muscovite, pyrrhotite, bismuthinite and bismuth (Fig. 5.16a). Quartz, feldspar, fluorite, and scheelite occur as inclusions in the core domains of the Nb-Ta minerals (Fig. 5.16b). Cracks and fissures crosscutting both core and rim are partially filled with bismuth formed from bismuthinite during regional metamorphism (Topa et al. 2002).

Thirteen elements were analyzed by EPMA in the core and rim zone of these (Y,REE,U,Th)-(Nb,Ta,Ti) oxides; however, Y an important constituent was omitted due to analytical problems. Although Y was not analyzed in wave-length dispersive mode, element mappings corroborate its presence in the crystal structure (Fig. 5.17a).

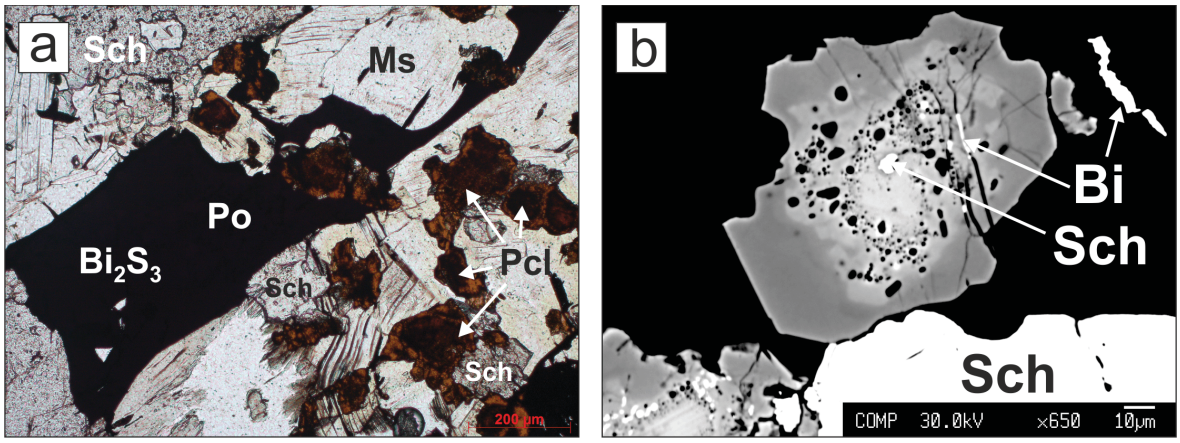

Fig. 5.16 (Y,REE,U,Th)-(Nb,Ta,Ti) oxide minerals of the pyrochlore group in quartz-scheelite vein sample A-K1q-c. **a)** Zoned pyrochlore group minerals (Pcl), under the transmitted light microscope, accompanied by scheelite (Sch), muscovite (Ms), pyrrhotite (Po) and bismuthinite (Bi_2S_3) plus bismuth. Zonation of Pcl is indicated by dark-brown semiopaque cores and orange-brown rims; plane polarized light. **b)** BSE image of a zoned pyrochlore group mineral with minute inclusion of scheelite in its centre. Fissures in minerals are partially filled with bismuth (Bi). BSE-dark inclusions in the core are quartz, feldspar and fluorite. The same grain is shown in the element map on Fig. 5.17a.

Analyses show that the major constituents are CaO, TiO_2, UO_2, and Nb_2O_5. Concentrations of CaO range in cores and rims between 17.7 mass% and 19.2 mass% CaO. Large systematic chemical differences between core and rim are observed for TiO_2, MnO, FeO, Nb_2O_5, SnO_2, Ta_2O_5, WO_3, and UO_2 (Table 5.3; Fig. 5.17a). According to the classification scheme for (Y,REE,U,Th)-(Nb,Ta,Ti) oxide minerals proposed by Ercit (2005), the analyzed Nb-Ta-Ti oxides observed belong the pyrochlore group (Fig. 5.17b).

	Pyrochlore	
	core n=4	rim n=4
CaO	17.96	18.70
TiO_2	16.77	8.69
UO_2	27.22	17.05
Nb_2O_5	28.86	46.79
Ta_2O_5	4.08	2.00
WO_3	4.20	1.63
MnO	0.31	0.24
FeO	0.35	0.66
SnO_2	0.15	1.00
SiO_2	0.06	bdl
Total	100.03	96.75

Tab. 5.3 Median oxide concentrations (in mass%) of zoned pyrochlore-group minerals in sample A-K1q-c; bdl= below detection limit.

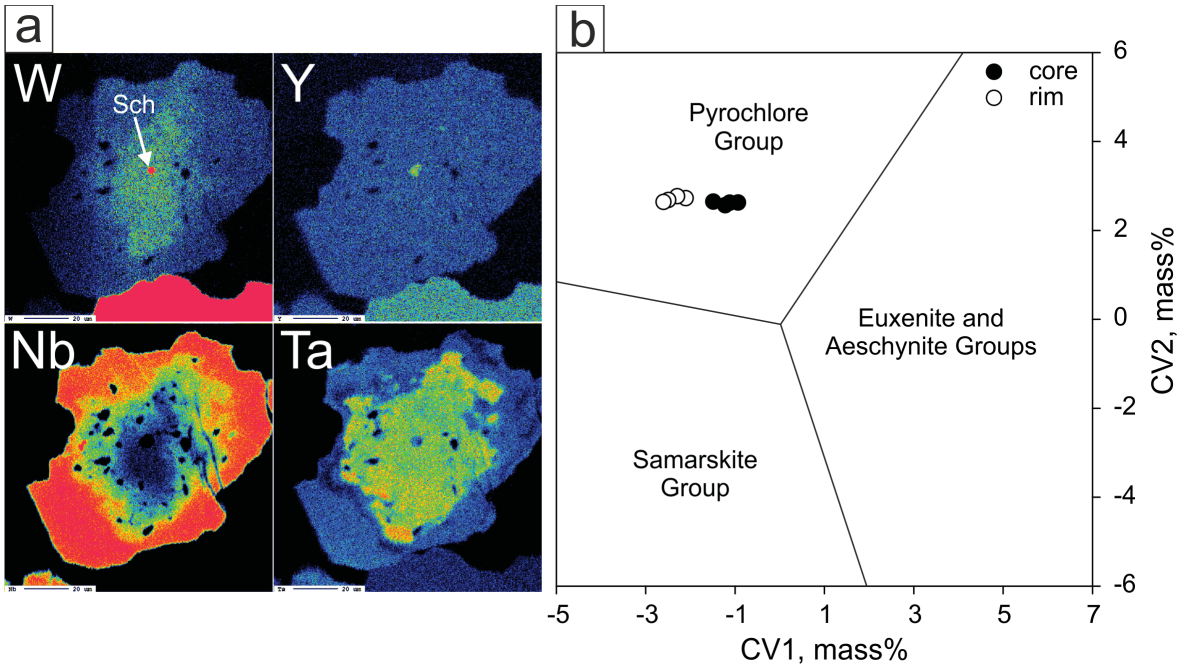

Fig. 5.17 Chemical characteristics of pyrochlore group minerals in the quartz-scheelite vein sample A-K1q-c. **a)** Element distribution maps of W, Y, Nb, and Ta of grain shown in Fig. 5.16b. The small inclusion and the adjacent mineral is scheelite. Dark blueish colors represent low concentrations; bright reddish colors represent high concentrations. **b)** Three-group model for canonical variables 1 and 2 according to Ercit (2005) to distinguish the pyrochlore-, samarskite-, euxenite- and aeschynite-groups. The analyses of this study plot in the pyrochlore group field.

EPMA analyses seem to be in good agreement for core domains, yielding high analytical totals between 100.02 mass% and 100.58 mass%. Thus, the Y-position of the cores is fully occupied by oxygen. On the contrary, analytical totals are low in rims, ranging between 96.41 mass% and 97.09 mass% indicating the presence of OH-groups or structural vacancies (Appendix E.4). Because of the high CaO, TiO_2 and UO_2 concentrations, mineral formulae were calculated on the basis of 7 O according to the chemical formula of titan-uranoan oxycalciopyrochlore $[(Ca,U,Na)_2(Nb,Ta,Ti)_2(O,OH)_7]$. The dominant cation on the A-position in both pyrochlore core and rim is Ca^{2+}. Despite analytical totals close to 100 mass% obtained for the cores, the sum of cations on the A-position is below 2.00 apfu, indicating the presence of vacancies (1.83-1.88 apfu). Thus, it is likely that analytical problems were encountered during EPMA measurements. The low totals of the pyrochlore rims and the partially vacant A-position (1.70-1.72 apfu) are ambiguous and could indicate the presence of H_2O on the A-site or site-vacancies (Atencio et al. 2010). Consequently, pyrochlore rims should be termed zero-valence-dominant pyrochlore. Although the analytical results and the classification of these phases as members of the pyrochlore group should be considered with caution, the presence of Nb-Ta minerals in the two hydrothermal quartz-scheelite

veins is an important observation for the following discussion of the magmatic-hydrothermal evolution of the K1-K3 orthogneiss and related W mineralization.

5.2.5 Scheelite $CaWO_4$

The trace element concentrations of Scheelite 2 and Scheelite 3 were analyzed by LA-ICP-MS from samples of the dark-colored K1-K3 orthogneiss (K1-1100, Gn-1065b), light-colored K1-K3 orthogneiss (K1-1152, K1-725), Granatspitz gneiss (ST-03/30), and Felbertauern augengneiss (SP-25/34). The complete data set is available in Appendix E.5. The analytical results show compositional differences between Scheelite 2 and Scheelite 3 but also subtle differences in REE distribution in Scheelite 2; subsequently, the sub-types Scheelite 2a and Scheelite 2b are distinguished.

Scheelite 2a occurs in samples of the dark-colored and light-colored varieties of the K1-K3 orthogneiss and is slightly darker in CL photomicrographs compared to Scheelite 2b. The latter was so far only observed in samples from the light-colored K1-K3 orthogneiss, where both Scheelite 2 types may occur within the same sample (e.g. K1-1152). Scheelite 2a shows a flat chondrite-normalized, wing-shaped REE pattern (Fig. 5.18a) with a pronounced negative Eu-anomaly (Eu/Eu*= 0.15-0.36) and slightly increased HREE contents (Lu_N/Ho_N= 1.22-2.23). Scheelite 2b shows concave-downward REE patterns with a strong depletion in MREE and a slightly less significant negative Eu-anomaly (Eu/Eu*= 0.23-0.51); consequently, the enrichment of the HREE expressed by Lu_N/Ho_N= 1.81-7.96 is most pronounced in Scheelite 2b. Figure 5.18b illustrates that Scheelite 3 is characterized by a strong depletion in LREE, negative Eu-anomalies (Eu/Eu*= 0.22-0.43) and either faintly decreasing or increasing normalized HREE contents (Lu_N/Ho_N= 0.72-1.69).

Only few scheelites were analyzed from the Felbertauern augengneiss (Fig. 5.19a). The data correspond, according to their chondrite-normalized REE patterns and CL-intensities, with Scheelite 2a and Scheelite 3 from the Felbertal scheelite deposit. The CL-darker scheelite (cf. Scheelite 2a) shows a flat REE distribution pattern with a pronounced negative Eu-anomaly (Eu/Eu*= 0.16) and a slight increase in HREE (Lu_N/Ho_N= 1.25). The CL-brighter scheelites (cf. Scheelite 3) feature a strong depletion in LREE and a less pronounced negative Eu-anomaly (Eu/Eu*= 0.36-0.39). The trend in HREE is variable; there is either a decline or rise with atomic weight (Lu_N/Ho_N= 0.73-1.71).

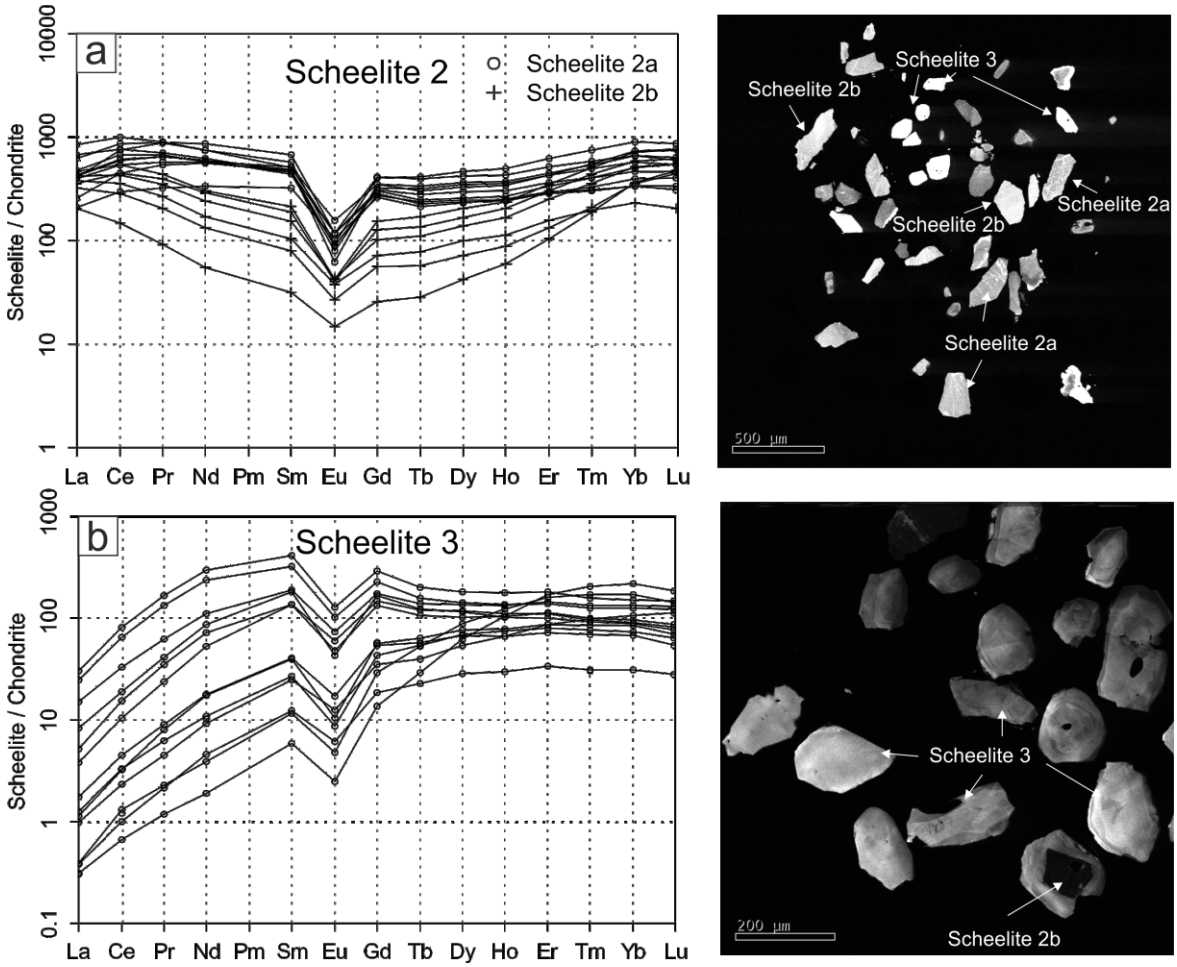

Fig. 5.18 Chondrite-normalized REE distribution of scheelite from the K1-K3 orthogneiss. **a)** Based on the REE pattern it is possible to distinguish two groups of Scheelite 2, namely Scheelite 2a (samples K1-1100, K1-1152, Gn-1065b) and Scheelite 2b (K1-725, K1-1152). Both scheelite generations are relatively CL-dark compared to Scheelite 3; however Scheelite 2b is slightly CL-brighter than Scheelite 2a to be best seen in CL-images of sample K1-1152. **b)** Scheelite 3 shows a strong depletion in LREE and has lower total ∑REE (samples K1-1100, K1-1152, K1-725, Gn-1065b). Sometimes, a weak zoning is evident in CL photomicrographs.

Scheelite from the Granatspitz gneiss exhibits vague internal structures (Fig. 5.19b). They have a bell-shaped REE pattern with the maximum enrichment between Dy and Ho except for the single analysis with the highest LREE concentrations. Scheelites from the Granatspitz gneiss are characterized by negative Eu-anomalies (Eu/Eu*= 0.33-0.48) and decreasing normalized HREE concentrations (Lu_N/Ho_N= 0.29-0.97), comparable to Scheelite 3 and the CL-bright scheelite generation from the Felbertauern augengneiss.

Scheelite 2a and 2b have higher Mo (4158-7895 ppm), Nb (476-3716 ppm) and lower Sr contents (38-152 ppm) compared to Scheelite 3 (Fig. 5.20a-b). With respect to the total REE concentrations (Fig. 5.20c), Scheelite 2a shows higher concentrations ranging between 940 ppm and 2249 ppm ∑REE compared to Scheelite 2b (378-1257 ppm REE).

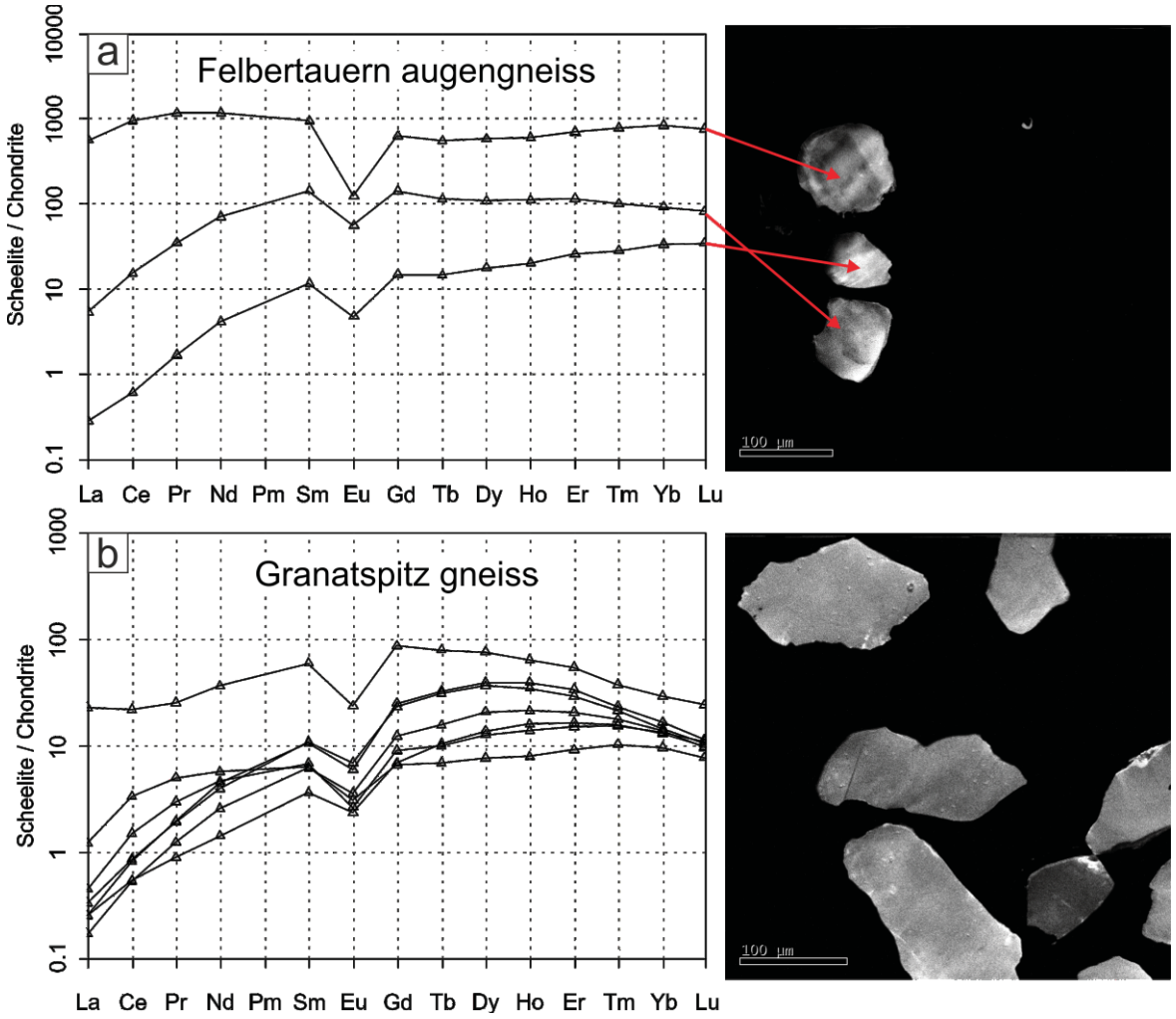

Fig. 5.19 Chondritic-normalized REE distribution of scheelites from the Zentralgneise. **a)** Scheelite from the Felbertauern augengneiss (SP-25/34). The red arrows connect the REE pattern with the respective analyzed scheelite. **b)** Scheelite from the Granatspitz gneiss (ST-03/30).

Scheelite 3 has low concentrations of Mo (4.8-230 ppm), Nb (18-331 ppm), ∑REE (39-601 ppm) but relatively high contents of Sr (235-1342 ppm). The analysis of CL-dark scheelite from the Felbertauern augengneiss perfectly matches the chemical composition of Scheelite 2a (6397 ppm Mo; 2681 ppm Nb; 2749 ppm REE; 153 ppm Sr). The CL-bright scheelites from the Felbertauern augengneiss correspond to Scheelite 3 concerning their Mo, Nb, REE, and Sr composition.

Scheelite from the Granatspitz gneiss is chemically similar to Scheelite 3 with respect to Mo (14-65 ppm), REE (17-137 ppm) and Sr (182-453 ppm) concentrations; however, it yields significantly lower concentrations of Nb (11-25 ppm). Figure 5.20d illustrates that the majority of Scheelite 2a, Scheelite 3 and scheelite from the Felbertauern augengneiss plot within the CHARAC (charge-and-radius-controlled) range defined by Bau (1996),

meaning that these scheelite generations have close-to-chondritic Y/Ho ratios between 24 and 34. However, a strong deviation from the CHARAC range towards more elevated ratios is observed in Scheelite 2b with values ranging between 47 and 110. In addition, scheelites from the Felbertauern augengneiss yield lower non-CHARAC values between 20 and 25.

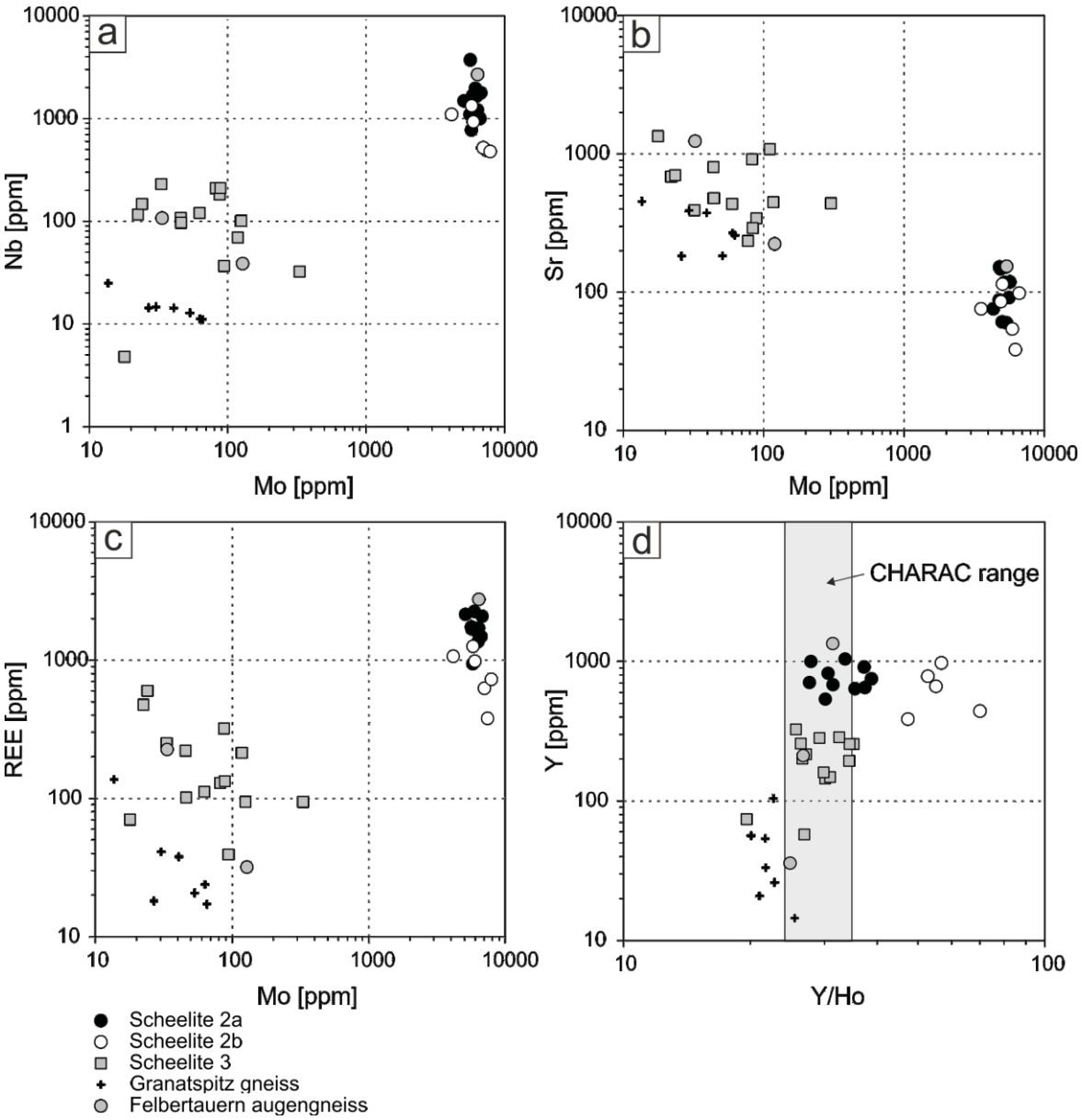

Fig. 5.20 Variation of trace elements in scheelite from the K1-K3 orthogneiss (Scheelite 2a, 2b, 3,), Felbertauern augengneiss and Granatspitz gneiss. **a-c)** Compositional x-y diagrams. **d)** Y/Ho vs. Y diagram. The CHARAC (charge-and-radius-controlled) range is the close-to-chondritic range between 24 and 34 defined by Bau (1996).

5.2.6 Titanite $CaTiSiO_4$ (O,OH,F)

Titanite was analyzed in samples of the dark-colored K1-K3 orthogneiss (Gn-1152a, K1-1100, B-K1d-a, C-K1d-b), light-colored K1-K3 orthogneiss (K1-43.57, K1-26.80, K1-1152), quartz-scheelite vein (A-K1q-c), younger K2 orthogneiss (AP-3.82), Felbertauern augengneiss (SP-07/30), Hochweißenfeld gneiss (FB-35/37), and Knorrkogel gneiss (FB-37/37). Mineral formulae were recalculated according to Ulmer (1993) on the basis of 3 cations and 5 O; all Fe is assumed to be Fe^{3+} and OH was calculated in apfu via (OH) = (Al + Fe^{3+}) - F. The complete data set is available in Appendix E.6. Titanites were analyzed by EPMA from core to rim to chemically characterize the individual zones that are distinguishable by BSE photomicrographs (Fig. 5.21a-d; Fig-5.22a-d). Generally, titanite occurs either as euhedral sphenoidal shaped crystals with oscillatory zoning evident in BSE images or as granular textured anhedral grains with poorly defined grain boundaries, displaying a chaotic patchy zoning (Fig. 5.21a-b; Fig. 5.22a-b). Occasionally, inclusions of apatite, allanite, rutile (<3.5 mass% Nb_2O_5), and zircon occur in the sphenoidal titanites, whereas patchy zoned titanites contain niobian rutile (<12.5 mass% Nb_2O_5), scheelite, and Fe-Ni sulfide inclusions. Oscillatory zoned titanite commonly shows recrystallized domains associated with reaction fronts in the exterior rims that are free of micro-inclusions. Reaction fronts have sharp boundaries and progressively migrate from the rim towards the central domains of titanite, thereby blurring existent primary zoning patterns (Fig. 5.21a). Euhedral to subhedral, oscillatory zoned titanites occur in the mineralized metagranitoids from the Felbertal scheelite deposit and in the barren Zentralgneise. The anhedral, patchy zoned titanite generation is frequently associated with biotite and (clino-) zoisite and dominantly occurs in lithologies from the Felbertal scheelite deposit and in biotite-rich parts of the Hochweißenfeld gneiss. The analytical results (Appendix E.6) show Ca contents in the titanite structure ranging between 0.87 apfu and 1.05 apfu. Silica completely occupies the tetrahedral position with concentrations ranging from 0.96 apfu to 1.00 apfu Si. The octahedral site is filled with Ti (0.61-0.93 apfu), Al (0.05-0.39 apfu) and Fe^{3+} (0.00-0.10 apfu). Concentrations of F considerably vary, with the highest concentrations of 3.65 mass% F (≡ 0.37 apfu) measured in an anhedral granular textured titanite from sample K1-43.57 (light-colored K1-K3 orthogneiss). The most important substitution mechanisms in titanite are:

(2) $(Al,Fe)^{3+} + (F,OH)^{-} \leftrightarrow Ti^{4+} + O^{2-}$ (Sahama 1946; Ribbe 1982)

(3) $2\ Ti^{4+} \leftrightarrow (Nb,Ta)^{5+} + (Al,Fe)^{3+}$ (Clark 1974)

(4) $Ca^{2+} + Ti^{4+} \leftrightarrow REE^{3+} + (Al,Fe)^{3+}$ (Green and Pearson 1986)

Substitution mechanism (2) accounts for the commonly observed chemical variations in natural titanite, whereby the incorporation of Al^{3+} is thermodynamically and structurally limited (Oberti et al. 1991; Troitzsch and Ellis 1999, 2002). Incorporation of Nb^{5+} occurs according to the coupled substitution mechanism (3). It must have been operative in titanites from the K1-K3 orthogneiss, which have Nb_2O_5 concentrations up to 3.68 mass% Nb_2O_5. Titanites from the Felbertauern augengneiss show slightly lower concentrations (<1.62 mass% Nb_2O_5). Concentrations of Nb_2O_5 are insignificant in the younger K2 orthogneiss (<0.40 mass% Nb_2O_5), Knorrkogel gneiss (<0.77 mass% Nb_2O_5) and Hochweißenfeld gneiss (<0.30 mass% Nb_2O_5).

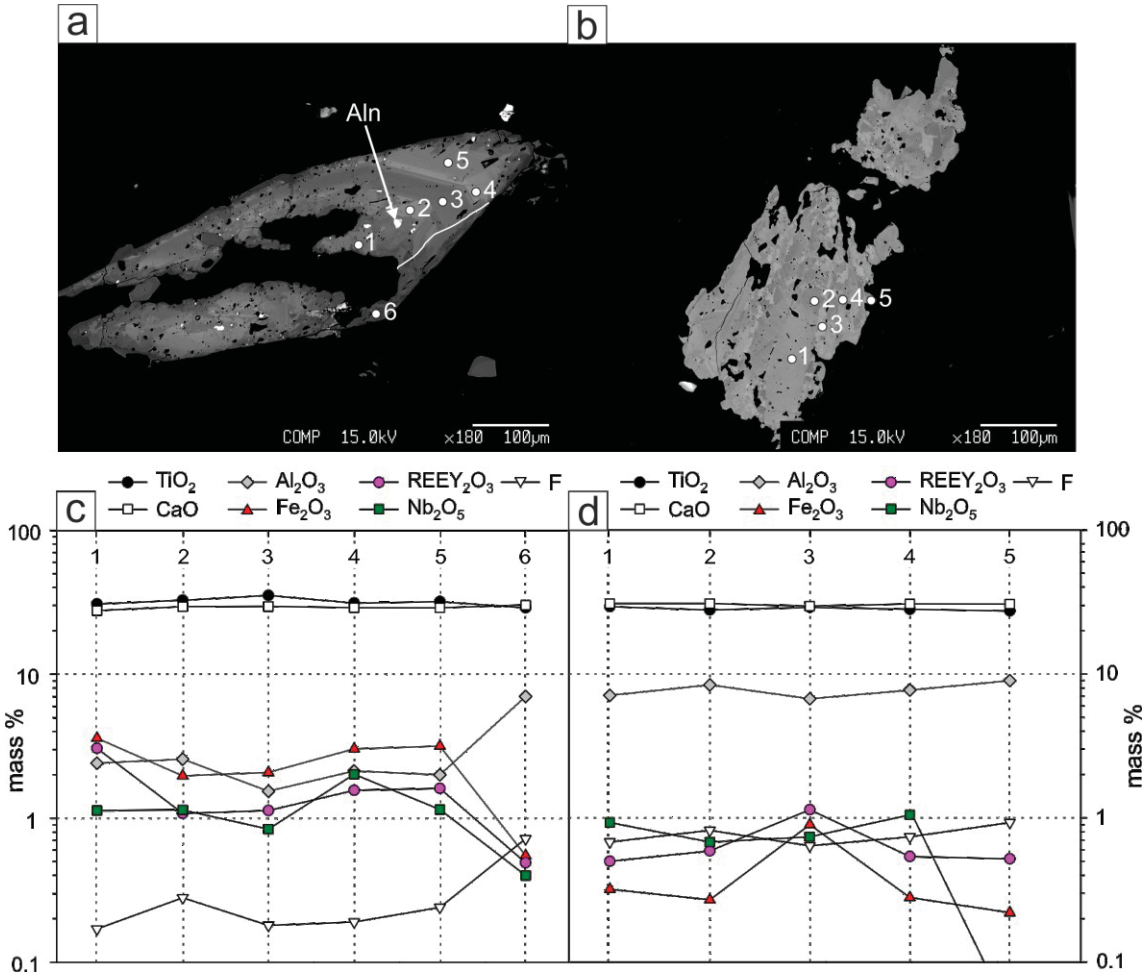

Fig. 5.21 Texturally and chemically different titanite generations in samples from the dark-colored K1-K3 orthogneiss. **a)** BSE images of oscillatory zoned titanite showing recrystallized domains, blurring the primary zoning patterns (reaction front is indicated by white line); analytical spots that correspond to chemical analyses in Fig. 5.21c are indicated with numbers 1-6; inclusions of allanite (Aln) are restricted to the BSE-dark zones; sample Gn-1152a. **b)** BSE photomicrograph of anhedral titanite with chaotic internal structures as seen by BSE-bright and BSE-dark patchy zones. Analytical spots that correspond to mineral chemical analyses in Fig. 5.21d are indicated with numbers 1-5; sample K1-1100. **c)** Chemical composition of the oscillatory zoned titanite with internal zones (1-5) and recrystallized rim (6). **d)** Chemical composition of the patchy zoned titanite.

Tantalum was detectable in nearly all titanites but does not exceed 0.62 mass% Ta_2O_5. High rare earth elements concentrations occur both in the BSE-bright patchy zones and in the inner core domains of oscillatory zoned titanites, attaining REE+Y concentrations of up to 7.50 mass% $REEY_2O_3$ in the K1-K3 orthogneiss, whereby Y_2O_3 is the dominant cation. The incorporation of REE+Y follows substitution mechanism (4) in which $REE+Y^{3+}$ enters the titanite structure for the divalent Ca cation. Uranium, thorium and tungsten contents were below the detection limit in all analyses.

Titanite analyses reveal high concentrations of Nb_2O_5 (0.84-2.02 mass%), Fe_2O_3 (1.97-3.60 mass%) and $REEY_2O_3$ (1.08-3.06 mass%) in the oscillatory zoned cores (dark-colored K1-K3 orthogneiss sample Gn-1152a; Fig. 5.21a and 5.21c). Concentrations of TiO_2 (30.8-35.3 mass%) are permanently higher compared to CaO (27.7-29.6 mass%). Aluminum (1.54-2.57 mass%) and F (0.17-0.28 mass%) contents were generally detected only in small quantities. The chemical composition of titanite remarkably changes in the recrystallized rim domain, which shows lower Nb_2O_5 (0.40 mass%), Fe_2O_3 (0.55 mass%) and $REEY_2O_3$ (0.49 mass%) concentrations compared to the core domains. Contrary, the abundances of Al_2O_3 (7.0 mass%) and F (0.72 mass%) strongly increase. Simultaneously, CaO (30.2 mass%) increases and TiO_2 (28.9 mass%) decreases with the result that CaO exceeds TiO_2 contents.

The patchy-zoned anhedral titanites display identical chemical composition as the recrystallized rims (Fig. 5.21b and 5.21d). The Al_2O_3 concentration of the respective titanite is remarkably high (<9.50 mass% Al_2O_3), corresponding to *X*Al [Al/(Fe^{3+}+Ti+Al)] ranging from 0.17 to 0.36 (median *X*Al= 0.27). The enrichment of Al_2O_3 is always accompanied by elevated F concentrations (0.68-0.93 mass%) in these titanites. Concentrations of Fe_2O_3, $REEY_2O_3$ and Nb_2O_5 are consistently below 1.0 mass%; for Nb_2O_5 even below the detection limit in the exterior rim domains. The high Al_2O_3 concentrations cause a decline in TiO_2 contents (27.4-29.4 mass%) following substitution mechanism (1); thus, CaO (29.6-30.9 mass%) is permanently present in higher amounts than TiO_2 in the patchy zoned titanites.

A similar distribution of TiO_2, CaO, Fe_2O_3, Nb_2O_5, $REEY_2O_3$, Al_2O_3, and F as described from titanites in the K1-K3 orthogneiss is documented for the Felbertauern augengneiss (Fig. 5.22a and 5.22c). The sphenoidal habitus of titanite is dominant, whereby both oscillatory and patchy chemical zoning patterns occur. Figure 5.22a shows a patchy zoned titanite characterized by a BSE-bright internal zone with different irregular shaped, grey-shaded domains in the exterior zones. The titanite is partly overgrown by a

small (<10 µm thick) BSE-dark rim. The analytical results (Fig. 5.22c) indicate low concentrations of F and Al_2O_3 in the BSE-bright core, which constantly increase towards the titanite rim. The reverse trend was detected for TiO_2 and $REEY_2O_3$, which systematically decrease towards the rim. Niobium is fairly constant, whereas Fe_2O_3 concentrations significantly drop in the BSE-dark overgrowth.

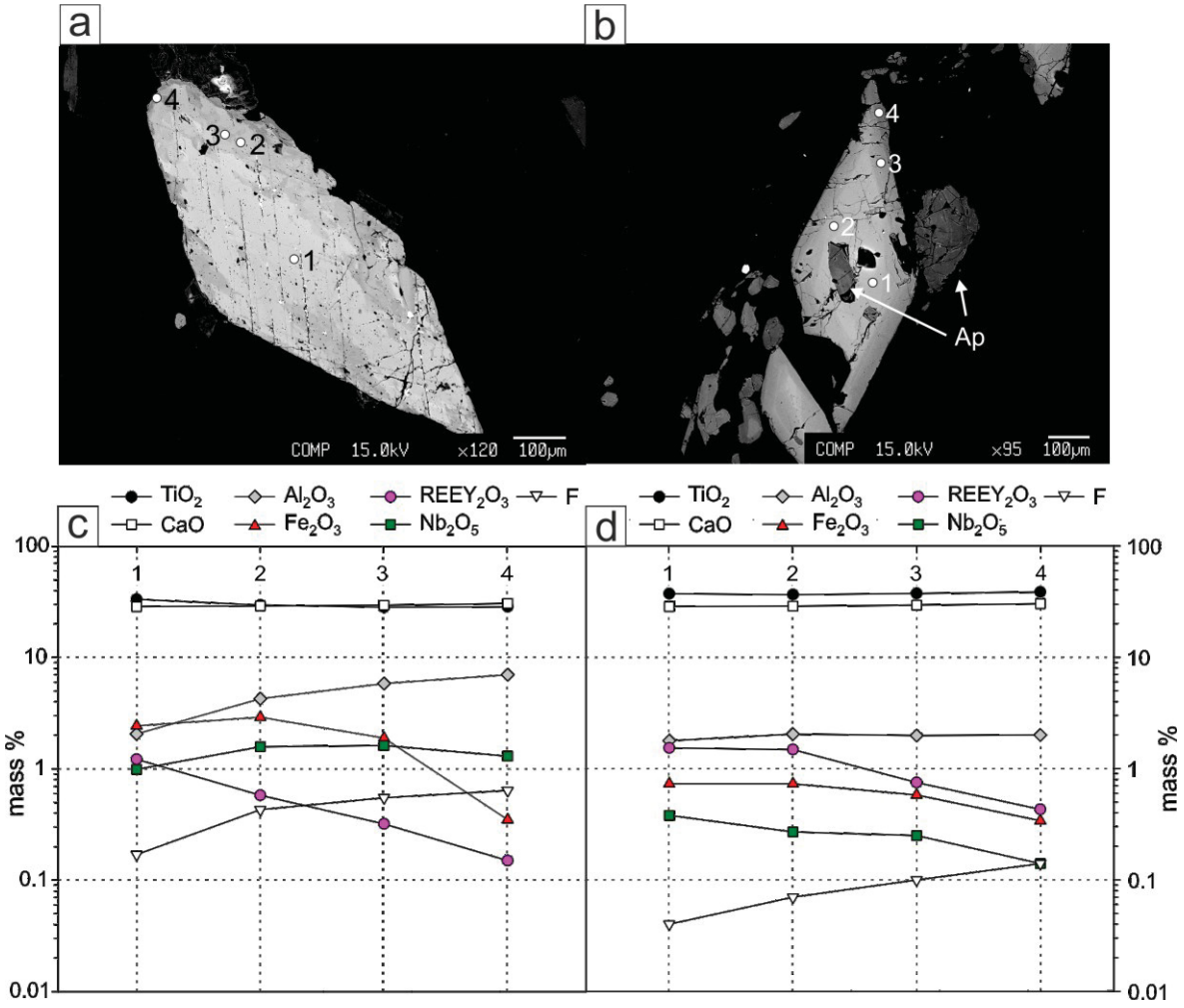

Fig. 5.22 Sphenoidal, zoned titanites from the Zentralgneise. **a)** BSE image of a patchy zoned crystal with internal BSE-bright domains and BSE-darker recrystallized domains. Analytical spots corresponding to mineral chemical analyses in Fig. 5.22c are indicated with numbers 1-4; Felbertauern augengneiss samples SP-07/30. **b)** Sphenoidal, oscillatory zoned titanite with apatite (Ap) inclusion. Analytical spots corresponding to mineral chemical analyses in Fig. 5.22d are indicated with numbers 1-4; Hochweißenfeld gneiss sample FB-35/37. **c)** Chemical composition of the patchy zoned titanite from the Felbertauern augengneiss. **d)** Chemical composition of the oscillatory zoned titanite from the Hochweißenfeld gneiss.

Sphenoidal titanites from the Hochweißenfeld gneiss chemically differ from the previously described titanites with respect to their TiO_2, CaO and Al_2O_3 concentrations (Fig. 5.22b and 5.22d, Appendix E.6). Titanites are characterized by simple oscillatory zoning with BSE-bright growth zones and sharp internal boundaries (Fig. 5.22b). A small (<50 µm thick) dark titanite rim can be distinguished in the BSE images. As in the previously described titanite crystals, Nb_2O_5, Fe_2O_3 and $REEY_2O_3$ concentrations continuously decrease from core to rim, while F increases (Fig. 5.22d); however, F contents were detected only in insignificant amounts (<0.15 mass% F). Moreover, Al_2O_3 occurs in much lower concentrations (*X*Al= 0.05-0.08) as compared to the Felbertauern augengneiss titanite rims or patchy zoned titanites from the Felbertal scheelite deposit. Consequently, titanites from the Hochweißenfeld gneiss are characterized by high TiO_2 and considerably lower CaO concentrations. Identical chemical characteristics were detected in titanites from the Knorrkogel gneiss (not graphically presented).

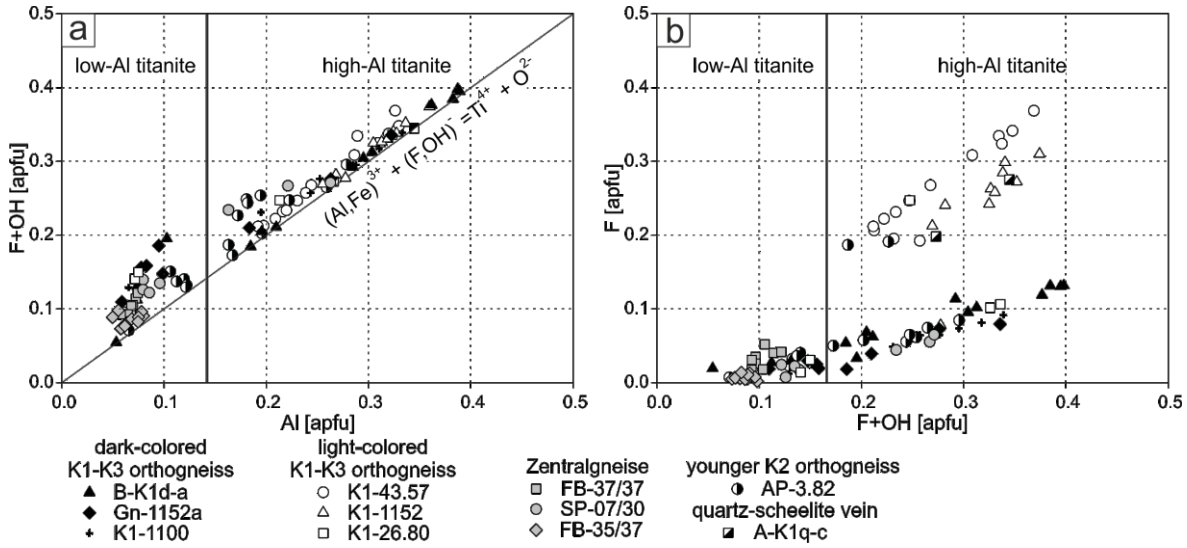

Fig. 5.23 Cationic plots showing low-Al and secondary high-Al titanites from the Felbertal scheelite deposit and Zentralgneise (Knorrkogel gneiss FB-37/37; Felbertauern augengneiss SP-07/30; Hochweißenfeld gneiss FB-35/37). **a)** Al vs. (F+OH) plot indicating that low-Al titanite contains additional Fe^{3+}, since the analyses scatter to the left of the $(Al,Fe)^{3+} + (F,OH)^{-} = Ti^{4+} + O^{2-}$ substitution line. Titanites with Al >0.25 apfu plot along the substitution line indicating minor influence of Fe^{3+} in the high-Al titanite generation. **b)** (F+OH) vs. F plot showing different trends of F and OH in the high-Al titanites.

According to Oberti et al. (1991), titanites with *X*Al >0.25 are classified as high-aluminous titanites; thus, patchy zoned titanites can be considered as high-Al titanites, whereas oscillatory zoned titanites (*X*Al <0.12) belong to the group of low-Al titanites. The low-Al titanites show an excess of F+OH over Al, indicating that Fe^{3+} is involved in the substitution mechanism (1) (Fig. 5.23a). Calculated *X*F [F/(F+OH)] values scatter between

0.17 and 0.93 in the high-Al titanites, demonstrating that Al substitution is additionally coupled to substitution of O^{2-} by OH^{-} (cf. Castelli and Rubatto 2002). This is supported by the F vs. (F+OH) diagram (Fig. 5.23b) in which high-Al titanites follow different trends. High-Al titanite from the dark-colored and the light-colored K1-K3 orthogneiss can be subdivided into two sub-groups based on the F content; namely high-Al high-F titanite and high-Al low-F titanite. High-Al titanites from the light-colored K1-K3 orthogneiss (K1-43.57, K1-1152) have consistently higher F concentrations than titanites from the dark-colored K1-K3 orthogneiss (and the younger K2 orthogneiss). Titanites from the quartz-scheelite vein and two analyses of titanites from the younger K2 orthogneiss plot close to these high-Al high-F titanites. Sample K1-26.80 is the only sample from the light-colored K1-K3 orthogneiss variety in which low-Al titanites were observed in addition to high-Al ones. The respective high-Al titanites correspond to the group defined by the dark-colored K1-K3 orthogneiss plus the younger K2 orthogneiss (high-Al low-F titanites) and to the light-colored K1-K3 orthogneiss (high-Al high-F titanites). Titanites from the Zentralgneise are characterized as low-Al titanites, except the patchy zoned titanite domains from the Felbertauern augengneiss (Fig. 5.22a) which are comparable to the high-Al low-F titanites from the Felbertal scheelite deposit.

5.2.7 Zircon $(Zr,Hf)SiO_4$

Sample material and zircon textures

Zircons were analyzed from four W-mineralized samples of the K1-K3 orthogneiss, two of the dark-colored (K1-1100, Gn-1065b) and two of the light-colored K1-K3 variety (K1-1152, K1-725). In addition one sample of aplite gneiss (AP-1124) was analyzed. The complete data set is available in Appendix E.7. CL-imaging revealed multiple stages of zircon growth (Fig. 5.24a). A CL-bright oscillatory zoned core domain (zone a) is usually overgrown by a CL-dark domain / rim, either displaying weakly developed oscillatory zoning (zone b) or no internal structure at all (zone b'). Inclusions of apatite are frequent in zones a and b; rarely quartz, potassium feldspar and titanite occur. Occasionally, apatite is oriented parallel to the crystal faces of zircon (zircon 6, Fig. 5.24a). Uraninite inclusions are exclusively found in the CL-dark domains. In one grain a ~100 µm large zircon showing oscillatory zoning is encased in the CL-dark growth domain b' (zircon 5, Fig. 5.24a). It is to be noted that in all K1-K3 orthogneiss samples, zircons with CL-bright cores are always overgrown by CL-dark rims.

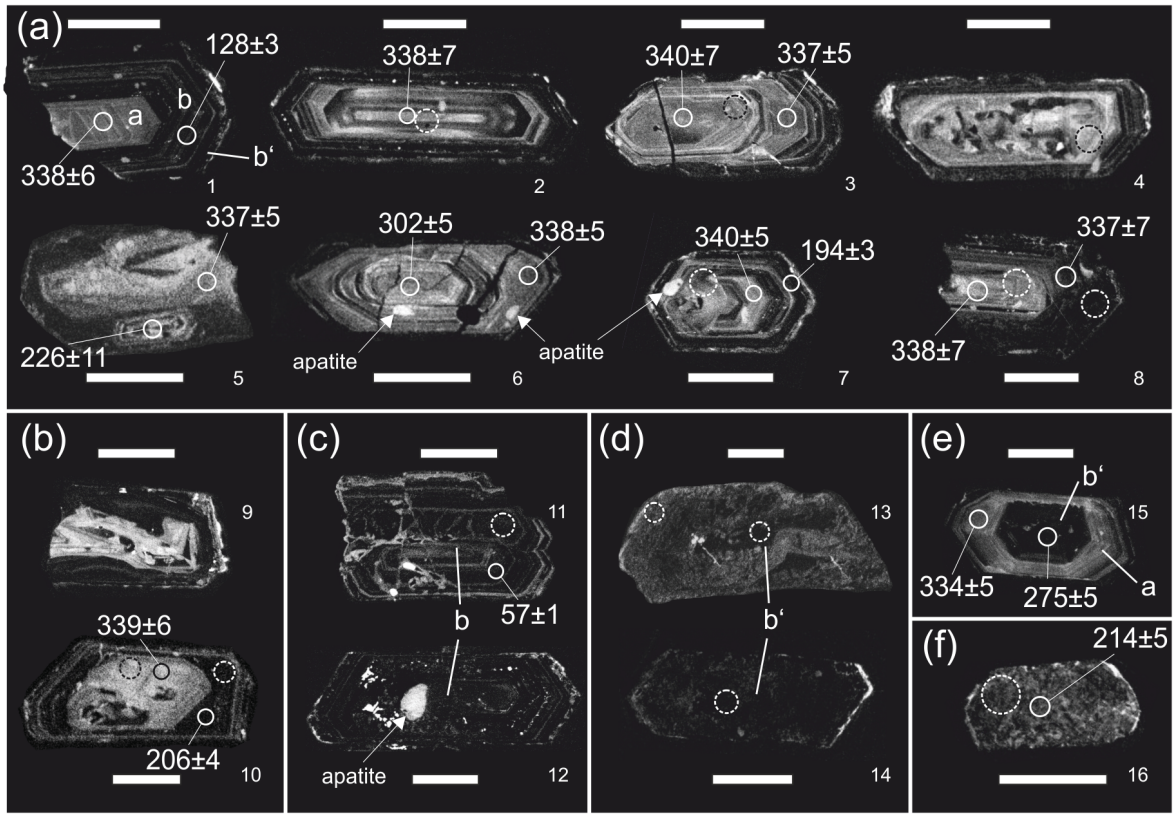

Fig. 5.24 Cathodoluminescence (CL) images of zircon grains from the K1-K3 orthogneiss and aplite gneiss. Scale bars are 100 µm. Apparent $^{206}Pb/^{238}U$ ages (uncertainties are 2σ) are shown with corresponding analysis spots (full circles; see chapter 5.3.2); dashed circles match pits for trace element analyses. The small CL-brightest inclusions are apatite (e.g. zircons 1, 6, 12). **a)** Zoned zircons with CL-bright oscillatory-zoned cores (zone a), weakly oscillatory-zoned CL-dark rims (zone b) and/or CL-dark rims without visible internal structure (zone b'). The CL-bright cores of zircons 4 and 7 show evidence for local late- to post-magmatic (?) recrystallization; zircons 1-3 dark-colored K1-K3 orthogneiss (sample K1-1100), 4-7 light-colored K1-K3 orthogneiss (K1-725) and 8 aplite gneiss (AP-1124). **b)** Zoned zircons with strongly resorbed CL-bright cores and CL-dark rims; zircon 9 is from the dark-colored K1-K3 orthogneiss (sample Gn-1065b), zircon 10 from the light-colored variety (sample K1-1152). **c)** CL-dark zircon with weak oscillatory zoning (zone b); zircons 11 and 12 are from the dark-colored K1-K3 orthogneiss (sample Gn-1065b and K1-1100, respectively). **d)** Subhedral CL-dark zircons (zone b') with irregular, patchy internal structures; zircons 13 and 14 light-colored K1-K3 orthogneiss (sample K1-725). **e)** Zircon with inverse zoning; a CL-dark core (zone b') is overgrown by a CL-bright oscillatory-zoned zone (zone a) and a thin outer CL-dark rim; zircon 15 dark-colored K1-K3 orthogneiss (sample K1-1100). **f)** Zircon with granular internal structure; aplite gneiss (sample K1-1100).

Occasionally, the CL-bright oscillatory zoning in the core is disrupted by irregular homogeneous CL-bright domains (zircon 7, Fig. 5.24a), suggesting local solid-state surface-bound recrystallization (Corfu et al. 2003; Schaltegger et al. 2009). Additionally, some zircons show irregular patchy core domains (zircon 4, Fig. 5.24a), possibly related to fluid-induced recrystallization (Pidgeon et al. 1998).

A few zircons display pronounced resorption textures in their core domains (Fig. 5.24b). Single-phase CL-dark zircons with weakly developed oscillatory zoning (zone b) occur at times (Fig. 5.24c) as well as eu- to subhedral zircons, which are nearly CL-dark and have irregular patchy and murky internal structure (Fig. 5.24d). The mono-phase grains could also be random sections through the outer zones of poly-phase grains. Zoning-free zircon with a granular internal structure is restricted to the aplite gneiss (zircon 16, Fig. 5.24f).

Zircons from one sample of the Felbertauern augengneiss (SP-25/34), the Granatspitz gneiss (ST-03/30) and an aplite from Achselalm (AA-49/39) were analyzed for comparative purposes. Zircon from the Felbertauern augengneiss shows similar two-stage growth textures as zircon from the K1-K3 orthogneiss (Fig. 5.25a). However, CL-bright oscillatory-zoned zircon lacking any CL-dark rims also occurs (zircon 3, Fig. 5.25a); such zircon type was not observed in the K1-K3 orthogneiss. Zircon from the Granatspitz gneiss exhibits magmatic oscillatory zoning (Fig. 5.25b); some contain rounded xenocrystic cores that are mantled by newly grown zircon material (zircon 4, Fig. 5.25b). Zircon from the Achselalm aplite (Fig. 5.25c) generally has irregular grain shapes and is larger in grain size (<500 µm) compared to other Zentralgneise. Granular textured zircon, similar to the aplite gneiss from the W-deposit, was also observed (zircon 7, Fig. 5.25c). Apart from that, zircon shows oscillatory zoning with alternating 50-100 µm thick CL-bright and CL-dark growth zones (zircon 8) or chaotic internal textures (zircon 9).

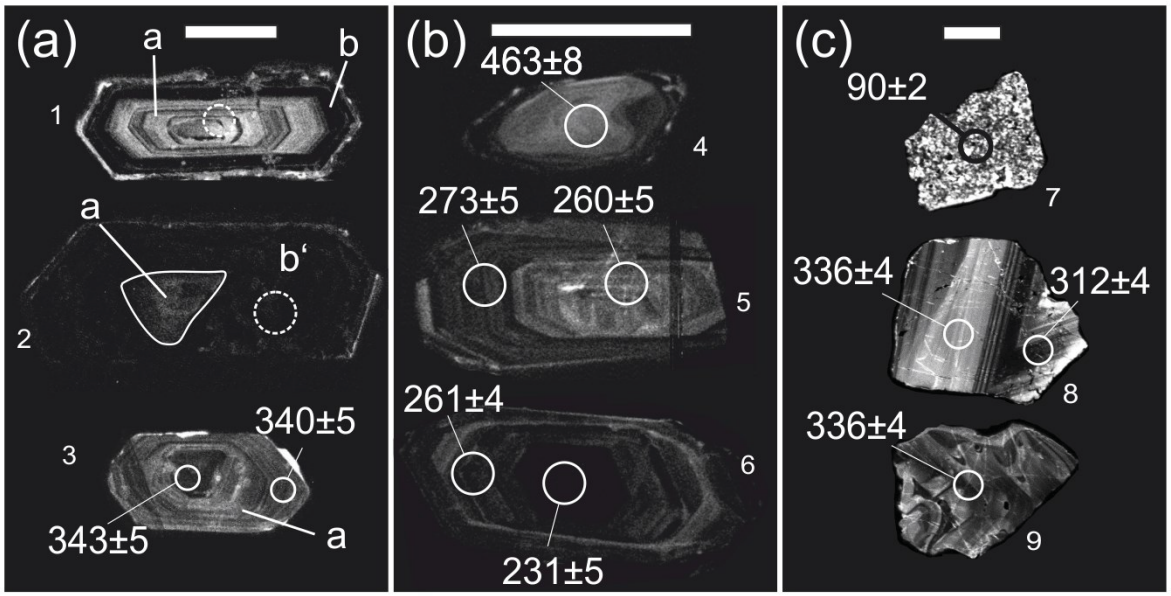

Fig. 5.25 Cathodoluminescence (CL) images of zircon from Zentralgneise and related aplites. Scale bars are 100 µm. Apparent $^{206}Pb/^{238}U$ ages (uncertainties are 2σ) are shown with corresponding analysis spots (full circles; see chapter 5.3.2); dashed circles match pits for trace element analyses. **a**) Felbertauern augengneiss (sample SP-25/34); 1 zoned crystal with CL-bright oscillatory-zoned core (zone a), CL-dark inner rim (zone b) and thin CL-bright outer rim; 2 CL-dark zircon (zone b') with relict slightly CL-brighter core (zone a); 3 oscillatory-zoned CL-bright mono-phase zircon (only zone a). **b**) Granatspitz gneiss (sample ST-03/30); 4 rounded CL-bright xenocrystic zircon core overgrown by CL-dark rim; 5 oscillatory-zoned zircon; 6 zircon with CL-dark core and oscillatory-zoned rim. **c)** Achselalm aplite (sample AA-49/39); 7 granular textured zircon similar to those from the aplite gneiss in the Felbertal W-deposit; 8 large irregular shaped oscillatory zoned zircon with CL-bright and CL-dark zones; 9 irregular shaped zircon with chaotic internal textures.

Rare earth elements

Multi-episodic growth of zircon from the K1-K3 orthogneiss and the aplite gneiss is associated with remarkable chemical variations in some trace elements in zircon analyzed by LA-ICP-MS. All zircon analyses with unreliable high P and Ti concentrations or REE patterns were sorted out due to the likely presence of mineral inclusions (e.g. apatite, titanite) hit during ablation. The full data set is listed in Appendix E.7.

Generally, the chondrite-normalized REE patterns of zircon from the K1-K3 orthogneiss and the aplite gneiss (Fig. 5.26a-c) are enriched in HREE relative to the LREE and show a significant negative Eu-anomaly [$Eu/Eu^* = Eu_N/\sqrt{(Sm_N \cdot Gd_N)}$] and a variable positive Ce-anomaly [$Ce/Ce^* = Ce_N/\sqrt{(La_N \cdot Pr_N)}$]. Regarding the concentrations of REE+Y, the CL bright core zones (zone a; Fig. 5.26a) have lower concentrations of ∑REE+Y (641-4576ppm) than the CL-dark domains (zone b'; 3102-18740 ppm; Fig. 5.26c). However, the major difference between the CL-bright and CL-dark zircon domains is the remarkably higher HREE contents in the CL-dark growth zones. This

results in steeper MREE to HREE patterns in the CL-dark generation and decrease of Gd_N/Lu_N = 0.035 from the CL-bright zone to 0.012 in the CL-dark domain. Moreover, two zircon sub-groups of both CL-bright zone a and CL-dark zone b' can be distinguished based on the Ce-anomalies. One sub-group of CL-bright cores is characterized by pronounced positive Ce-anomalies (Ce/Ce* = 11-84), while the second group contains much higher La and Pr concentrations, resulting in a less significant Ce-anomaly (Ce/Ce* = 1.5-5.5, Fig. 5.26a). The same discrimination holds true for the CL-dark domains, where one sub-group shows significantly higher Ce-anomalies (Ce/Ce* = 2.7-26) compared to the second group (Ce/Ce* = 1.3-2.8, Fig. 5.26c). Most zircons have REE patterns with a concave upward enrichment of the MREE to HREE; only the granular textured zircons from the aplite gneiss (Fig. 5.24f) show a rather linear rise in the MREE to HREE part of the pattern (Gd_N/Lu_N < 0.003; Fig. 5.26b).

Trace element analyses of zircon from the Felbertauern augengneiss yield very similar REE-patterns as observed in the K1-K3 orthogneiss (Fig. 5.26d-f), although the ∑REE+Y concentrations are slightly lower, ranging between 1311 and 3731 ppm in the internal CL-bright zircon domains (zone a) and between 7174 and 12362 ppm in the homogeneous CL-dark domains (zone b'). Again, two sub-groups of CL-bright cores can be distinguished based on the Ce-anomaly. While two samples show very pronounced Ce-anomalies (Ce/Ce* = 28 and 91), most of the CL-bright cores have considerably lower Ce/Ce* ranging from 2.9 to 5.9 (Fig. 5.26d). CL-dark zircons with weak internal oscillatory structure (zone b) are comparable to the respective zircon group of the K1-K3 orthogneiss (Fig. 5.26e). With respect to the CL-dark zircon domains (zone b'), only one sub-group was recognized (Ce/Ce* = 9.8-39), corresponding to the sub-group with the more pronounced positive Ce-anomalies in the K1-K3 orthogneiss (Fig. 5.26f).

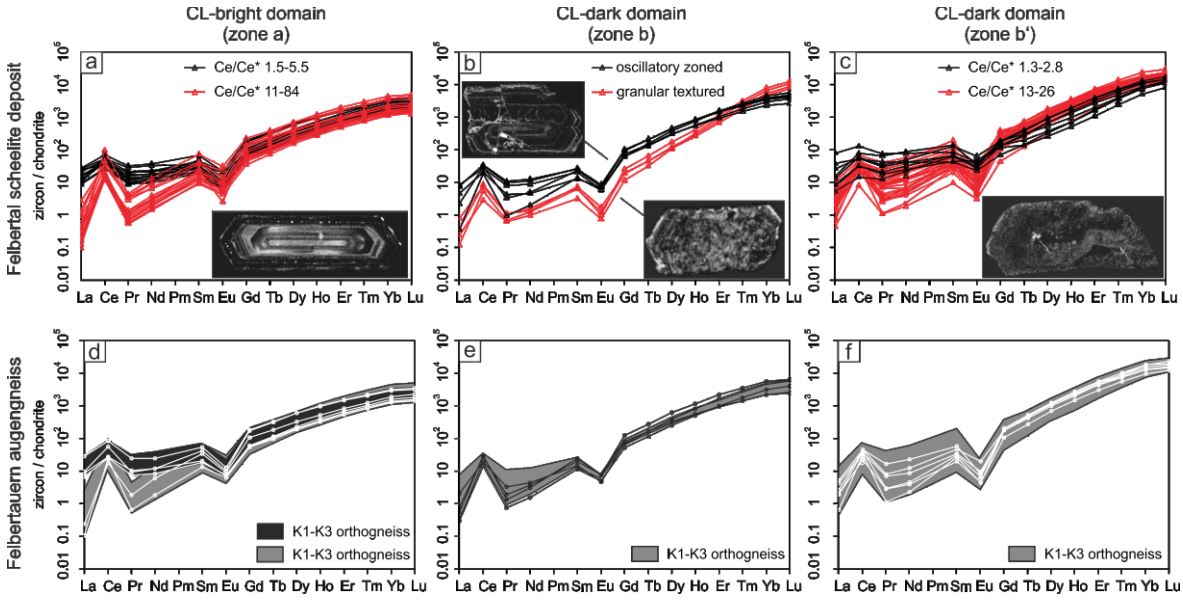

Fig. 5.26 a-f) Chondrite-normalized REE plots of the distinct growth zones of zircons from the K1-K3 orthogneiss, aplite gneiss and Felbertauern augengneiss. Note that the zircon domains observed in the K1-K3 orthogneiss (a-c) are also present in the Felbertauern augengneiss (d-f). K1-K3 orthogneiss data in Fig. 5.26d are shown in grey (high Ce/Ce') and black (low Ce/Ce*) shading for better comparison; the grey shading in Fig. 5.26e represents CL-dark oscillatory zoned zircon (zone b) from the K1-K3 orthogneiss; the grey shading in Fig. 5.26f refers to CL-dark zircons (zone b') from the K1-K3 orthogneiss.

Other trace elements

The trace elements U, W, Ta, Nb, Hf, P, Ca, Y, B, and Li clearly allow the subdivision of the CL-bright oscillatory zircons (zone a), the CL-dark oscillatory rims (zone b) and the structure-less CL-dark zircons (zone b') in the K1-K3 orthogneisses plus aplite gneiss (Fig. 5.27). Based on trace element composition, it is *not* possible to discriminate zircon from the dark-colored and the light-colored K1-K3 orthogneiss variety. The trace element concentrations of CL-dark zircon with weak oscillatory zoning (zone b) and the granular textured zircon from the aplite gneiss are higher compared to CL-bright (zone a) zircon but lower than in structure-less CL-dark zircon (zone b'). The most prominent difference is the dramatic increase in U from the CL-bright cores (691-3079 ppm U; median = 1200 ppm U) to the structure-less CL-dark domains (1.23-5.56 mass% U; median = 2.41 mass% U). The majority of CL-bright zircon has Th/U between 0.20 and 0.40, while 80 % of CL-dark domains yield Th/U values below 0.15.

There is a positive correlation of U with W, Ta, Nb, and Hf concentrations in zircon (Fig. 5.27). Tungsten is generally low in the CL-bright cores (0.18-3.77 ppm W; median = 0.45 ppm W) but increases towards the CL-dark domains, ranging between 4.30 and 11.39 ppm W (median = 5.98 ppm W; one outlier at 2.06 ppm W). Both Ta and Nb

increase towards the CL-dark zircon, attaining maximum concentrations of 367 ppm Ta and 431 ppm Nb. Similar high Nb-Ta concentrations are observed in the granular textured zircon from the aplite gneiss. These zircons additionally have the highest Hf concentrations of up to 4.60 mass% Hf. The Hf concentrations vary from 0.88 to 1.59 mass% Hf in the CL-bright domains and from 1.15 to 3.97 mass% Hf in the CL-dark zircon in the K1-K3 orthogneiss. The increase in Hf concentrations is expressed by the simultaneous decrease in Zr/Hf. CL-bright cores are characterized by nearly chondritic Zr/Hf values (38; Anders and Grevesse, 1989) ranging between 32.2 and 41.7 (one outlier at 50.5), while CL-dark zones generally have smaller values (Zr/Hf = 15.0-26.5; two outliers at 34.1 and 40.3). Phosphorus is homogenously distributed within the zircon domains; however the sub-group of CL-bright cores with more pronounced Ce-anomalies shows considerably lower P concentrations (141-590 ppm P, median = 323 ppm P; one outlier at 1780 ppm P). Calcium concentrations in the CL-bright internal domains increase from 174-3780 ppm Ca to 0.15-1.42 mass% Ca in the CL-dark domains. The sub-group with CL-bright cores and higher Ce/Ce*has lower Ca contents (174-977 ppm Ca; median = 258 ppm Ca) compared to CL-bright cores with lower Ce/Ce* (688-3480 ppm Ca, median = 1853 ppm Ca). The Y contents are fairly low in the CL-bright zircon sub-groups (311-2633 ppm Y, median = 1027 ppm Y) but increase in the CL-dark zircons (1113-9941 ppm Y, median = 4787 ppm Y).

A major difference between the CL-bright and CL-dark domains is their Li and B concentration. Boron dramatically increases in the CL-dark zircon, notably in the CL-dark zones with higher Ce/Ce* (15-88 ppm B, one outlier with 136 ppm B); the sub-group with the less pronounced Ce anomaly shows elevated B contents in the range of 7.30-44.0 ppm; the CL-bright cores are generally lower in B (0.26-6.57 ppm B). Lithium concentrations are high in the CL-bright cores (1.41-42.0 ppm Li), whereas the sub-group with low Ce/Ce* has relatively higher Li contents (median = 31.32 ppm Li) compared to CL-bright zircon with high Ce/Ce* (median = 14.75 ppm Li). Generally lower concentrations were observed in the CL-dark zircon (4.71-17.2 ppm Li, one outlier at 47 ppm Li).

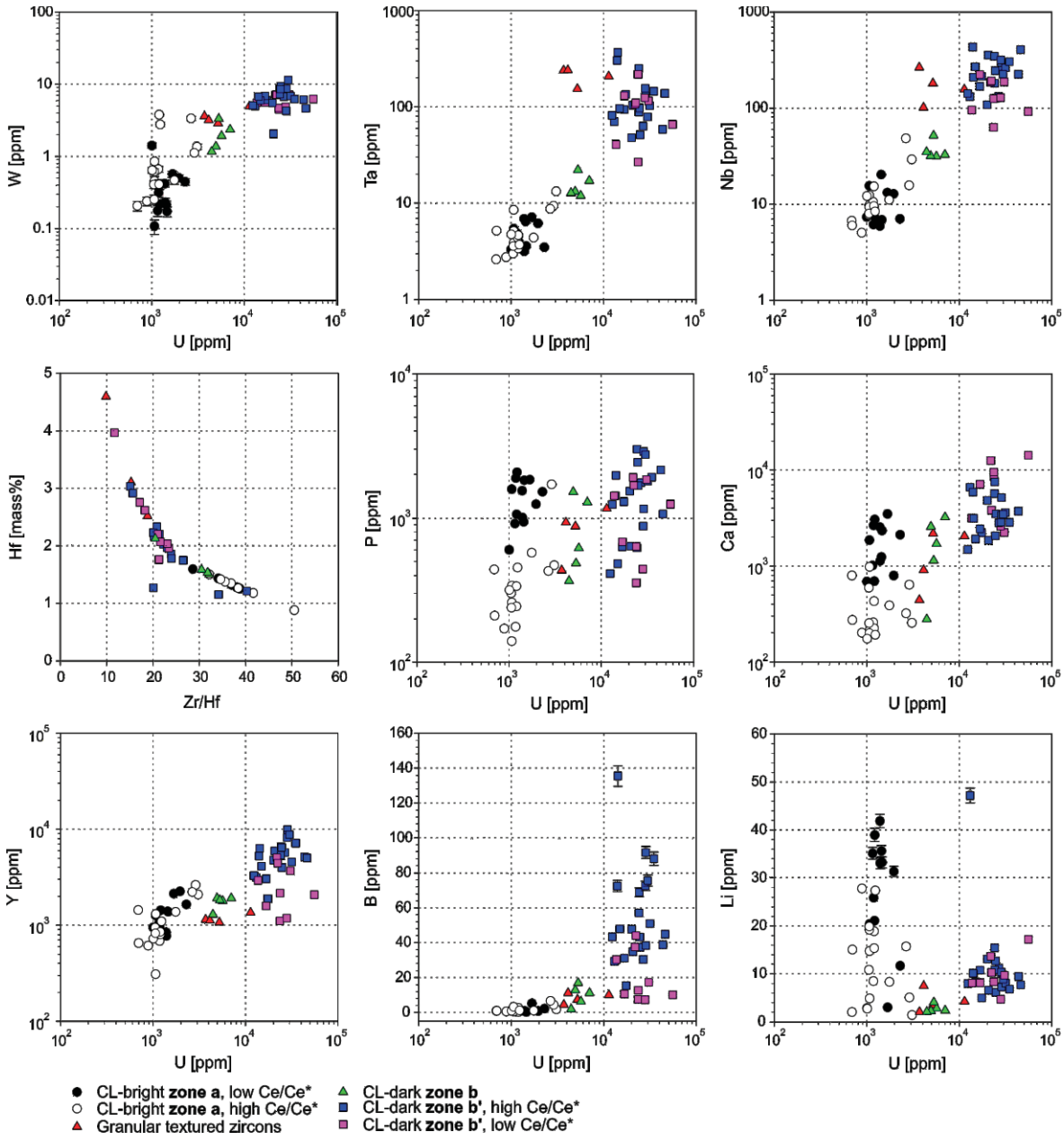

Fig. 5.27 Compositional x-y diagrams showing trace element distribution in the different zircon domains from the K1-K3 orthogneiss and the aplite gneiss. Uncertainties (1σ) are either smaller than the symbol size or are shown as error bars.

Zircon from the Felbertauern augengneiss exhibits nearly identical trace element distribution as those from the K1-K3 orthogneiss (Fig. 5.28). There is a systematic increase of W, Ta and Nb with increasing U from CL-bright cores to CL-dark zircon domains. However, the total concentrations of W are lower (< 3.90 ppm W) compared to the respective zircon domains from the K1-K3 orthogneiss. Additionally, zircon from the Felbertauern augengneiss shows lower Ca concentrations in the CL-dark domains (<2300 ppm Ca).

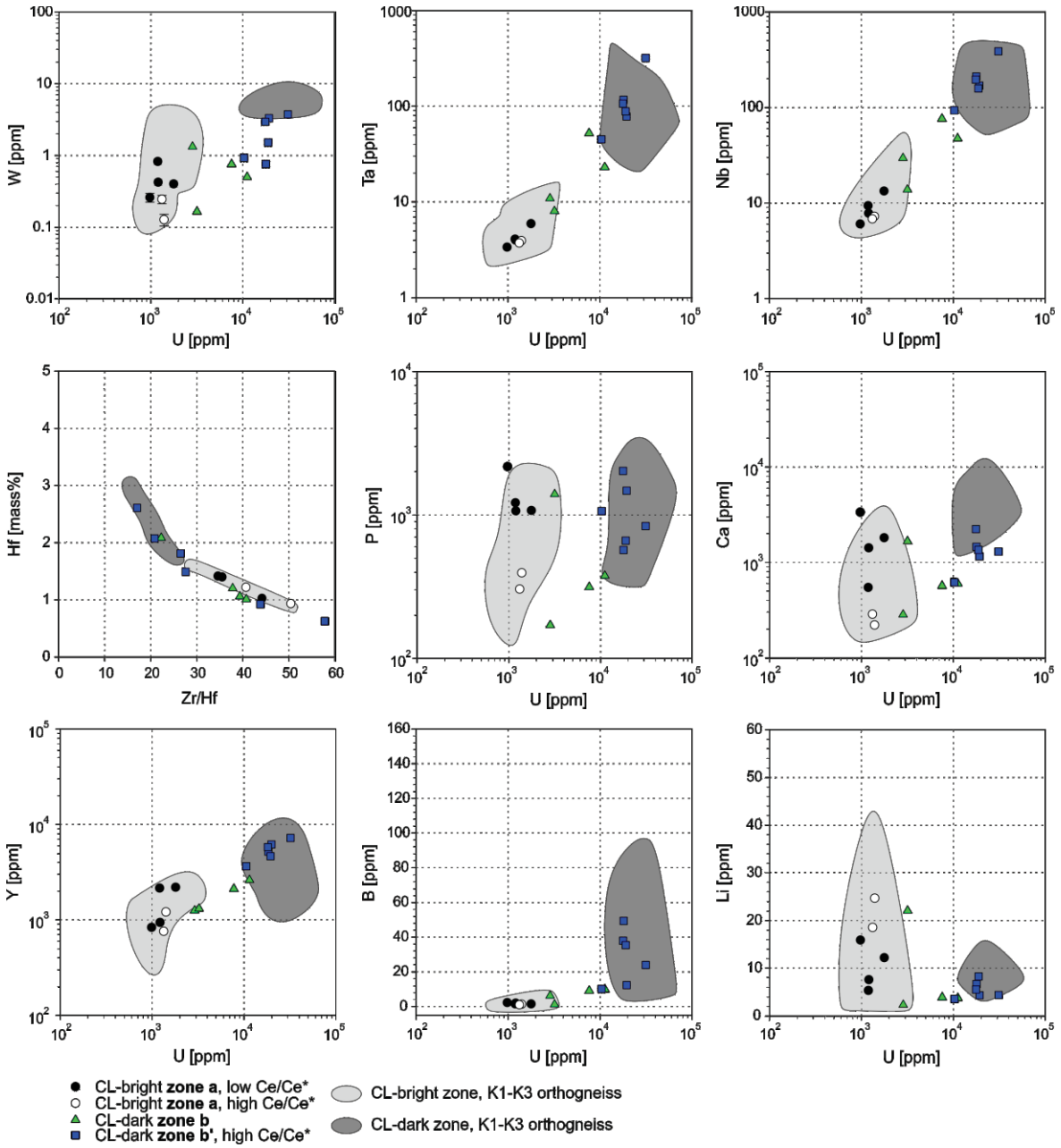

Fig. 5.28 Compositional x-y diagrams showing the trace element distribution in the different zircon domains from the Felbertauern augengneiss compared to the K1-K3 orthogneiss (grey shaded fields; Fig. 5.27). Uncertainties (1σ) are smaller than the symbol size.

The Zr/Hf ratios generally tend to decrease with increasing Hf concentrations from CL-bright to CL-dark zircon, although some scatter exists in the CL-dark domains. Boron concentrations are very low in the CL-bright cores (< 2.00 ppm) and higher in the CL-dark zircon domains (< 50 ppm B).

5.3 Isotope geochemistry

5.3.1 Strontium isotope systematics of scheelite and apatite

Sample description

Laminated scheelite-quartz ore and gneiss (eastern ore field)

Scheelite 1 was analyzed in two sub-samples of sample FT-74, one polished thin section and one polished section. The sample is a laminated scheelite-quartz ore ("quarzitisches Scheelitreicherz") from the former open pit mine in the eastern ore field. Scheelite 1 is very fine-grained (<0.4 mm) and strongly aligned, causing a prominent foliation in this high-grade ore. Saccharoidal quartz, the major mineral, is completely recrystallized. In contrast, scheelite shows incomplete recrystallization. Stringers of very fine-grained scheelite aggregates are composed of recrystallized blue-fluorescent Scheelite 3 plus slightly larger elongated relicts of blueish-white fluorescent scheelite. The Scheelite 1 relicts preserve fine oscillatory growth zoning (Figs. 2.2a, 5.29a). White mica occurs as an accessory mineral.

Additionally, Scheelite 1 and apatite were analyzed from a leucocratic, laminated, scheelite-rich gneiss that comes from the eastern ore field (sample FS-1). FS-1 differs from the laminated scheelite-quartz ore in that it contains more plagioclase, muscovite, epidote, apatite and zircon but less quartz than sample FT-74. However, FS-1 features an elevated grade of the fine-grained first scheelite generation.

K1-K3 orthogneiss (western ore field)

The K1-K3 orthogneiss samples studied are from the levels 1152, 1100, 1065, and 725 m in the underground mine. Additionally, a weakly mineralized aplitic gneiss sample from level 1124 m was analyzed. Scheelite 2 and 3 occurs either in mm to cm thick quartz veinlets or disseminated throughout the orthogneiss. Quartz and varying amounts of plagioclase, potassium feldspar, biotite, and phengitic muscovite constitute the main mineral assemblage. Zircon, titanite, allanite, clinozoisite, epidote, calcite, and apatite are common accessory phases. Usually, apatite occurs associated with metamorphic muscovite, biotite, plagioclase, calcite, fluorite or epidote in the groundmass of the orthogneisses. Apatite crystals are <150 µm and display a pronounced zoning in BSE- and CL images, allowing distinction of cores and rims (chapter 5.2.2). The cores are characterized by brighter CL signal and they tend to be euhedral. They sometimes reveal oscillatory growth zoning and usually show evidence for intense brittle deformation as

indicated by a crosscutting network of micro-fractures. The rims are darker in CL, are anhedral and do not display the same intensity of brittle deformation as the cores. Frequently, apatite rims are less than 20 µm thick, consequently aggravating measurements by laser ablation.

Quartz-scheelite vein (western ore field)

Sample B-K1q-A (thin section) is from a quartz-scheelite vein from level 1164 m where it crosscuts the K1-K3 orthogneiss. It contains both larger grains of Scheelite 2 overgrown / replaced by Scheelite 3 (Fig. 5.29b, c). Scheelite is associated with calcite, titanite, phenakite and blue beryl (aquamarine); the latter partly replaces phenakite or occurs as poikiloblastic crystals with inclusions of phenakite (cf. Franz et al. 1986). Occasionally, titanite is completely replaced by rutile, calcite, fluorite, and quartz. A 1 to 3 mm thick potassium feldspar veinlet containing minor albite, calcite, Nb-bearing rutile, zircon, and pyrrhotite crosscuts the quartz-scheelite vein.

Quartz-diorite gneiss (western ore field)

Scheelite 2 and 3 were analyzed from the coarse-grained quartz diorite gneiss on level 1038 m (sample Gn-1038a). The mineral assemblage is characterized by pale-brown biotite, albite, quartz, zoisite and subordinate amounts of anhedral to euhedral titanite, apatite, calcite, amphibole, and garnet. Quartz is aligned in lenticular clusters and shows significant evidence of recrystallization. Scheelite 2 forms porphyroclasts (<5 mm), occasionally with well-developed growth zoning. This larger grain was used to determine the $^{87}Sr/^{86}Sr$ distribution within a single scheelite crystal (see below).

Sample Gn-1262 was taken on level 1262 m. Compared to Gn-1038a it is more fine-grained with a more pronounced schistosity. In thin section biotite displays a gradual transition from fresh, dark brown biotite to chloritized biotite and finally to chlorite. Zoisite is common and forms prismatic crystals parallel to the foliation of the rock. Scheelite has not been observed, although the whole rock W concentration of 26 ppm suggests minor scheelite mineralization. Subhedral, prismatic apatites are <150 µm and display similar pronounced core-rim textures in CL images as observed in the K1-K3 orthogneiss.

Younger K2 gneiss (western ore field)

In the course of a drilling campaign on the 1175 m level that aimed to drill through the K1-K3 orthogneiss body, a four meter thick leucocratic, biotite-poor gneiss was intersected. Sample AP-3.82 is from the drill core UB-343 (meter 3.82-7.53) and is characterized by

the mineral assemblage plagioclase, potassium feldspar, zoisite, quartz, and biotite. Biotite is irregularly distributed indicating post-tectonic crystallization. Common accessory minerals are muscovite, anhedral to sometimes euhedral titanite, allanite, clinozoisite, zircon, and scheelite. The sample shows evidence of potassic alteration in form of a network of thin (<200 µm) potassium feldspar veinlets. Where these small veins crosscut the gneiss, plagioclase is altered to sericite. Scheelite 2 and 3 are mainly restricted to quartz veinlets. Clearly, post-magmatic alteration and mineralization processes affected this orthogneiss.

Zentralgneise

Three orthogneiss samples (2 Zentralgneise and 1 aplitic dike) were included because they contain small amounts of scheelite. A scheelite-bearing specimen of Felbertauern augengneiss (SP-25/34) was sampled on the road to the St. Pöltner Hütte north of the Matreier Tauernhaus at 2052 m above sea level. Scheelite showings in this area have already been reported from Meßelinggraben - Grüner See - Schwarzer See area, where it was found in metabasites of the basal amphibolite member (Höll 1975; Höll 1979; Neinavaie et al. 1983). The orthogneiss is composed of larger potassium feldspar crystals within a fine-grained matrix of quartz, plagioclase and biotite. Calcite, titanite, apatite, allanite, epidote, and clinozoisite can be identified as accessory minerals (chapter 4.2.2).

A Zentralgneis sample with sparse scheelite mineralization is from the Granatspitz gneiss (ST-03/30) 2 km northwest to Enzingerboden in Stubachtal. The mineral assemblage is characterized by fine-grained quartz, biotite, muscovite, and feldspars. Plagioclase commonly contains minute inclusions of muscovite and frequently forms inclusions in potassium feldspar porphyroblasts that have overgrown the existing foliation. The metamorphic assemblage includes garnet, biotite, muscovite, quartz, and plagioclase. In both gneisses disseminated fine-grained scheelite has been detected (chapter 4.2.5). Scheelite is blue fluorescent and does not show any zoning under CL.

Scheelite from the Achselalm aplite (chapter 4.2.7) is fine-grained (<500 µm) and shows whitish-blue fluorescence colors. CL-images reveal the presence of two distinct scheelite types, similar to Scheelite 2 and 3 from the W-deposit (Fig. 5.29d); a CL-dark scheelite type is sometimes overgrown by a CL-bright type.

In addition to scheelite, apatite from the Felbertauern augengneiss (SP-25/34, FB-12/30) and Knorrkogel gneiss (FB-09/30) were analyzed for $^{87}Sr/^{86}Sr$. Apatite in the Felbertauern augengneiss is euhedral to sub-rounded and shows homogeneous cores in

CL with either CL-brighter or CL-darker rims (Fig. 5.29e). Sample FB-09/30 displays a well-developed foliation with larger potassium feldspars (<2 cm) creating an augen gneiss texture. Recrystallized quartz, plagioclase and biotite form the matrix. Biotite is partly chloritized and plagioclase features minute muscovite inclusions. Common accessory minerals are apatite, titanite, allanite, clinozoisite, and calcite. Apatite (<500 µm) has a significant rectangular prismatic habitus and shows weak zoning in CL images (Fig. 5.29f).

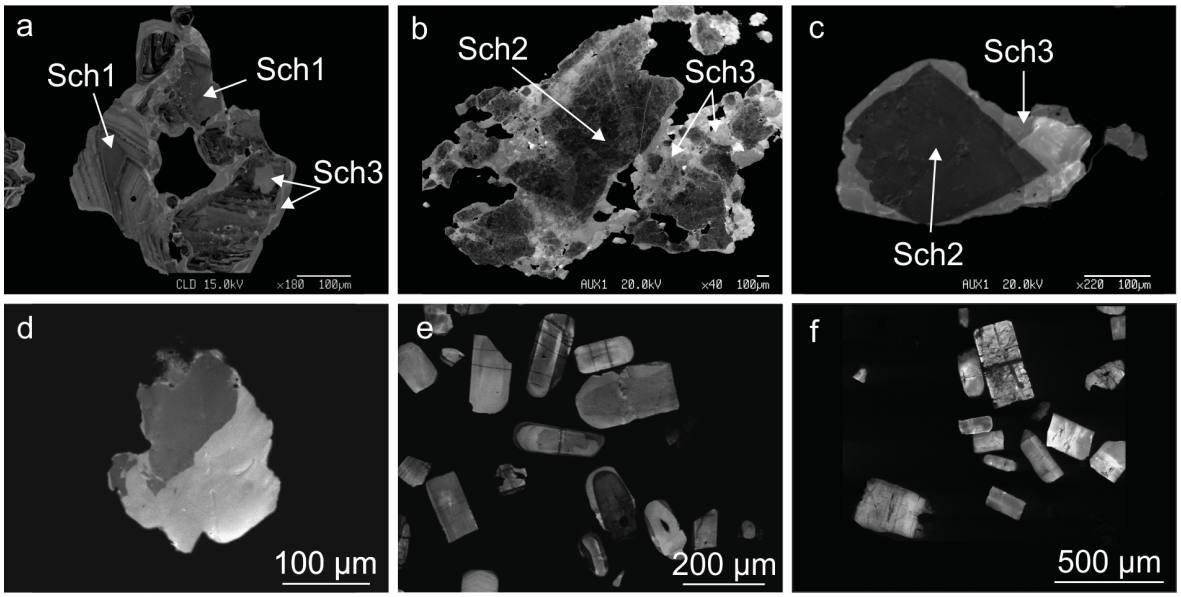

Fig. 5.29 Cathodoluminescence (CL) images of scheelite and apatite. **a)** CL image of Scheelite 1 (Sch1) with fine oscillatory zoning overgrown and partly replaced by CL-brighter metamorphic Scheelite 3 (Sch3); eastern ore field, laminated scheelite-quartz ore, sample FT-74. **b-c)** CL images of Scheelite 2 (Sch2) replaced / overgrown by Scheelite 3 in a quartz-scheelite vein; western ore field level 1164 m, sample B-K1q-A. **d)** Scheelite in the Achselalm aplite showing a CL-dark scheelite type overgrown by CL-bright scheelite; sample AA-49/39. **e)** CL-image of apatite grains from Felbertauern augengneiss; sample FB-12/30. **f)** CL-image of apatite grains from Knorrkogel gneiss; sample FB-09/30.

Rb-Sr data of scheelite

Scheelite and apatite are ideal minerals to record the initial $^{87}Sr/^{86}Sr$ distribution of the respective source because both minerals can incorporate significant amounts of Sr in substitution for Ca, but only contain negligible quantities of Rb (Bell et al. 1989; Creaser and Gray 1992). Scheelite 1, 2, and 3 from the distinct lithologies/ores in the eastern and the western ore field described above were analyzed for their Rb-Sr isotope composition (chapter 3.3.4). 141 analyses were made on 10 samples. Additionally, scheelites from a sample of the Felbertauern augengneiss (SP-25/34) and the Granatspitz gneiss (ST-03/30) were analyzed. The data are summarized in Table 5.4. $^{87}Sr/^{86}Sr$ values are also graphically presented in Figs. 5.30 to 5.33. The complete dataset is available in Appendix

F. In Scheelite 1 and 2 Sr concentrations vary in the range of several hundreds of ppm (Table 5.4). However, both generations usually show low Sr contents with similar median values of 78 and 73 ppm respectively, although Scheelite 2 from the Younger K2 orthogneiss (AP-3.82) yields elevated median concentrations of 191 ppm Sr. The third scheelite generation is characterized by higher Sr concentrations ranging from 27 to 949 ppm (median 206 ppm). The concentrations of Sr in scheelite from the Felbertauern augengneiss are slightly higher (159-901, median 530 ppm) compared to the Granatspitz gneiss (122-311, median 219 ppm). The two distinct scheelite generations in the aplite from the Achselalm are indistinguishable based in their Rb-Sr isotope systematics. The concentration of Sr scatters between 167 and 1469 ppm (median = 588 ppm Sr).

The median $^{87}Rb/^{86}Sr$ ratios are generally below 0.075, although a few analyses yielded more elevated ratios of up to 0.866 (Table 5.4); they are significantly lower in the Zentralgneise (<0.052). From the $^{87}Rb/^{86}Sr$ measurements the initial $^{87}Sr/^{86}Sr$ values were recalculated for 338 Ma, which is the best estimate for the emplacement age of the K1-K3 orthogneiss (cf. chapter 6.5.1). The complete data set of $^{87}Sr/^{86}Sr$ for scheelites, arranged according to their hosting lithologies, is graphically shown in Fig. 5.30. Low values of 0.72078 to 0.73625 are found in Scheelite 1 from the laminated scheelite-quartz ore (FT-74) in the eastern ore field. In contrast, $^{87}Sr/^{86}Sr$ of Scheelite 1 from the scheelite-rich gneiss (FS-1) range between 0.72887 and 0.76417 and match the isotopic composition of Scheelite 2 in the K1-K3 orthogneiss (0.72266-0.76375). Scheelite 2 in the quartz-diorite gneiss shows the strongest variation (0.70724-0.76832), whereas Scheelite 2 from a quartz-scheelite vein is characterized by generally high radiogenic values (0.75392-0.76812). Interestingly, Scheelite 2 (<1 mm) from a network of quartz-scheelite veinlets crosscutting the Younger K2 orthogneiss (AP-3.82) displays the least radiogenic $^{87}Sr/^{86}Sr$ values of 0.70775 to 0.71093 and a smaller variation compared to the other samples. Scheelite 3 in the scheelite-rich gneiss yields $^{87}Sr/^{86}Sr$ between 0.72610 and 0.76320, which is generally lower than ratios in the respective generation from the K1-K3 orthogneiss (0.72383-0.80479), meta-quartz diorite (0.74331-0.80689) and quartz-scheelite vein (0.77079-0.77310). The $^{87}Sr/^{86}Sr$ ratio in scheelite from the Granatspitz gneiss (ST-03/30) is, with exception of one outlier (0.77467), in the range of 0.74387-0.74523 (median 0.74422). The two analyses on scheelite from the Felbertauern augengneiss (SP-25/34) yield radiogenic $^{87}Sr/^{86}Sr$ ratios of 0.77348 and 0.77366. The $^{87}Sr/^{86}Sr$ values of scheelite from the Achselalm aplite are low and less scattering compared to scheelite from the W-deposit, ranging between 0.71029 and 0.71464.

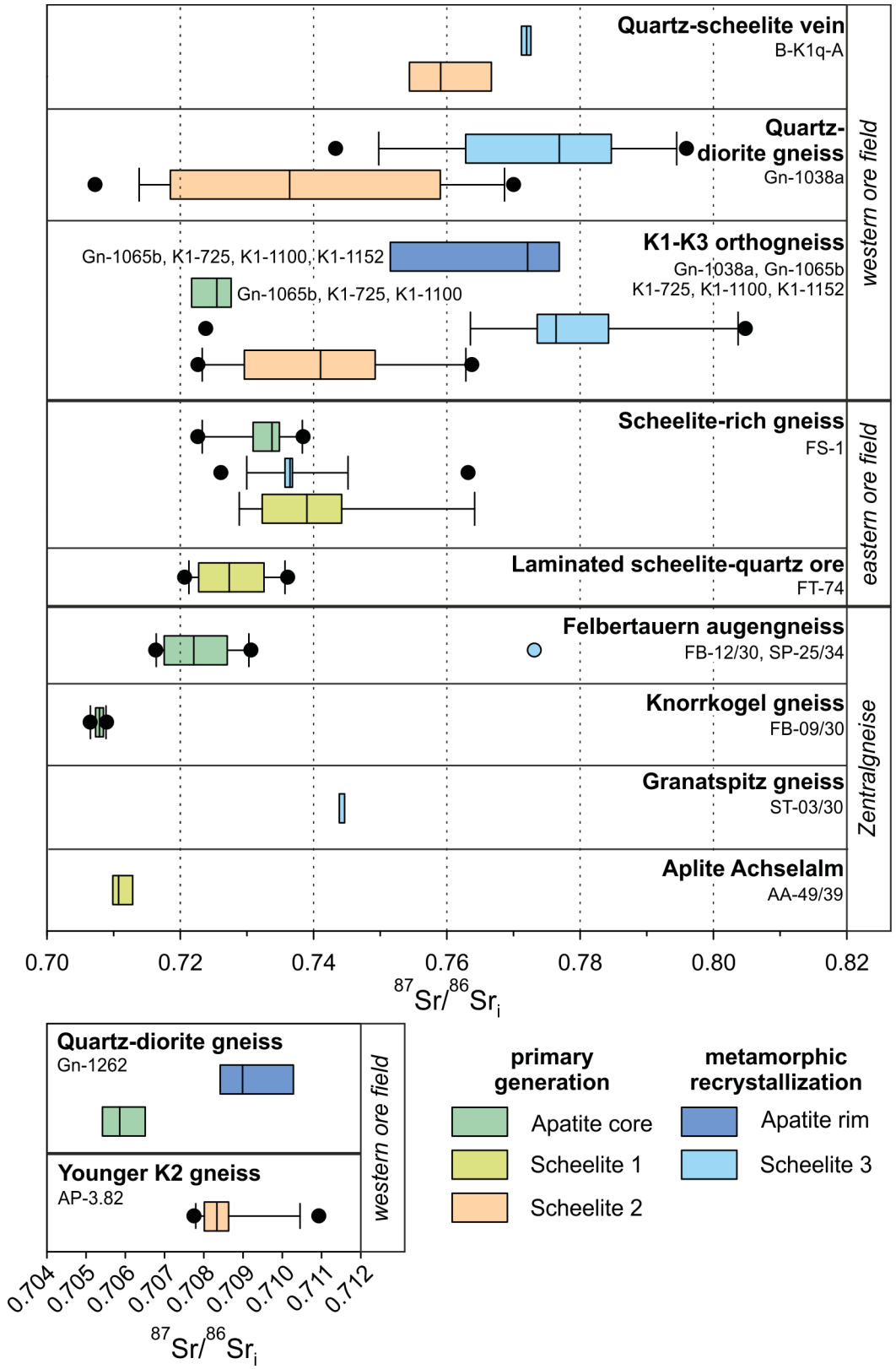

Fig. 5.30 $^{87}Sr/^{86}Sr$ ratios in scheelite and apatite arranged in a box-and-whisker diagram according to their hosting lithologies. The boxes represent the interquartile range between the 25th and 75th percentile with the median shown as vertical line inside the box. The whiskers refer to the 10th and 90th percentile; individual outliers are illustrated as dots.

Mineral	Sample	n	Sr [ppm]			$^{87}Rb/^{86}Sr$			$^{87}Sr/^{86}Sr_I$		
			Min	Max	Median	Min	Max	Median	Min	Max	Median
Scheelite											
Scheelite 1, e	FS-1; FT-74	27	39	234	78	0.00047	0.33191	0.07243	0.72078	0.76417	0.73063
Scheelite 2, w	Gn-1038a Gn-1065b K1-725 K1-1100 K1-1152 AP-1124 B-K1q-A	38	31	342	73	0.00001	0.11080	0.00172	0.70724	0.76832	0.74283
Scheelite 2, w	AP-3.82	13	68	253	191	0.00002	0.02509	0.00037	0.70775	0.71093	0.70833
Scheelite 3, w	Gn-1038a Gn-1065b K1-725 K1-1100 K1-1152 B-K1q-A	46	27	949	206	0.00001	0.86641	0.00124	0.72383	0.80689	0.77532
Scheelite 3, e	FS-1	17	27	465	210	0.00007	0.08010	0.00072	0.72610	0.76320	0.73646
Felbertauern augengneiss	SP-25/34	2	159	901	530	0.00715	0.02109	0.01412	0.77348	0.77366	0.77357
Granatspitz gneiss	ST-03/30	6	122	311	219	0.00003	0.05198	0.00598	0.74387	0.77467	0.74422
Aplite Achselalm	AA-49/39	14	167	1469	588	0.00006	0.14020	0.00197	0.71029	0.71464	0.71161
Apatite core											
K1-K3 orthogneiss, w	Gn-1065b K1-725 K1-1100	7	174	779	427	0.00019	0.00575	0.00256	0.72044	0.74514	0.72549
Scheelite-rich gneiss, e	FS-1	10	82	672	202	0.00191	0.02685	0.00620	0.72264	0.73845	0.73377
Quartz-diorite gneiss, w	Gn-1262	4	892	1274	1173	0	0.00267	0.00042	0.70527	0.70672	0.70586
Felbertauern augengneiss	FB-12/30 SP-25/34	11	53	514	246	0.00053	0.03633	0.00283	0.71634	0.72954	0.72192
Knorrkogel gneiss	FB-09/30	11	392	1094	478	0.00043	0.01732	0.00250	0.70649	0.70896	0.70790
Apatite rim											
K1-K3 orthogneiss, w	Gn-1065b K1-725 K1-1100 K1-1152	8	162	1296	679	0.00016	0.07510	0.00817	0.74535	0.77937	0.77211
Quartz-diorite gneiss, w	Gn-1262	4	944	1248	1105	0.00002	0.00299	0.00005	0.70833	0.71061	0.70899

Tab. 5.4 Summary of Sr isotopic data of the different scheelite stages, apatite cores and apatite rims. Abbreviations: e = eastern ore field, w = western ore field; for results of individual analyses see Appendix F.

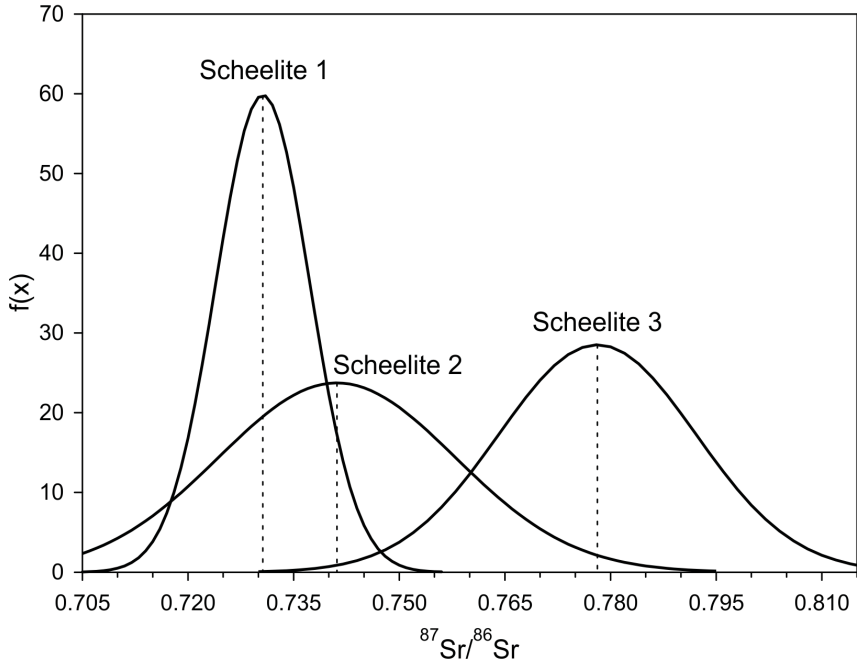

Fig. 5.31 $^{87}Sr/^{86}Sr$ ratios in Scheelite 1, 2 (without AP-3.82), and 3 (without FS-1) fitted with a Gaussian distribution. The difference in the medians between the three sample groups is statistically significant as tested with a Wilcoxon signed-rank test. The dashed lines represent the median value of each generation.

Summarizing the results for the three investigated scheelite generations at Felbertal W-deposit: $^{87}Sr/^{86}Sr$ values range between 0.72078 and 0.76417 in Scheelite 1 (median $^{87}Sr/^{86}Sr = 0.73063$) and between 0.70724 and 0.76832 in Scheelite 2 (median $^{87}Sr/^{86}Sr = 0.74283$). Thus, $^{87}Sr/^{86}Sr$ values of Scheelite 1 and 2 overlap considerably, although higher values are to be found in Scheelite 2; except Scheelite 2 from the Younger K2 orthogneiss (0.70775-0.71093). Values for Scheelite 3 are even higher, they range from 0.72383 to 0.80689 (median $^{87}Sr/^{86}Sr = 0.77532$). Scheelite 3 from the scheelite-rich gneiss is also exceptional because of relatively low and less scattering $^{87}Sr/^{86}Sr$ (median 0.73646).

Applying the Wilcoxon signed-rank test to compare the Sr isotope dataset (Fig. 5.31) indicates that there are statistically significant differences among the median values of the three scheelite generations. The difference between Scheelite 1 and 2, however, is not very pronounced ($P = 0.011214$) and the two datasets overlap to a great extent. Scheelite 2 from sample AP-3.82 and Scheelite 3 from sample FS-1 were not included since their $^{87}Sr/^{86}Sr$ ratios are rather low and these data are regarded as outliers (see discussion). There is also some overlap between Scheelite 2 and 3 but the median values are significantly different ($P \leq 0.000001$).

Because Scheelite 1 had been interpreted as an older generation of Cambrian age (Eichhorn et al. 1997) $^{87}Sr/^{86}Sr$ of Scheelite 1 was also recalculated to 520 Ma. Results yielded variations in the 3rd decimal place, even for analyses having the highest $^{87}Rb/^{86}Sr$. This variation is therefore negligible considering the total variation in $^{87}Sr/^{86}Sr$ of Scheelite 1 data set and our interpretations given below are not biased in this respect.

To evaluate the spatial distribution of the Sr isotopic composition within single scheelite crystals, multiple spot-analyses on larger scheelite grains were carried out. The Scheelite 2 crystal (<5 mm) from the quartz-diorite gneiss (Gn-1038a) reveals a remarkable scatter in its Sr isotopic systematics on a sub-mm scale with $^{87}Sr/^{86}Sr$ ratios ranging from 0.71695 to 0.74740 (Fig. 5.32a). The thin rim of Scheelite 3 overgrowing Scheelite 2 is even more radiogenic with $^{87}Sr/^{86}Sr$ ratios of 0.79712 and 0.79813. Furthermore, a Scheelite 2 porphyroclast from a quartz-scheelite vein (B-K1q-A) with evidence of incomplete recrystallization to Scheelite 3 shows $^{87}Sr/^{86}Sr$ ratios in the range of 0.75392 to 0.76812 (Fig. 5.32b). The Sr isotopic composition of Scheelite 3 in this sample is slightly more radiogenic but exhibits less scattering compared to Scheelite 2; $^{87}Sr/^{86}Sr$ ratios vary between 0.77079 and 0.77310.

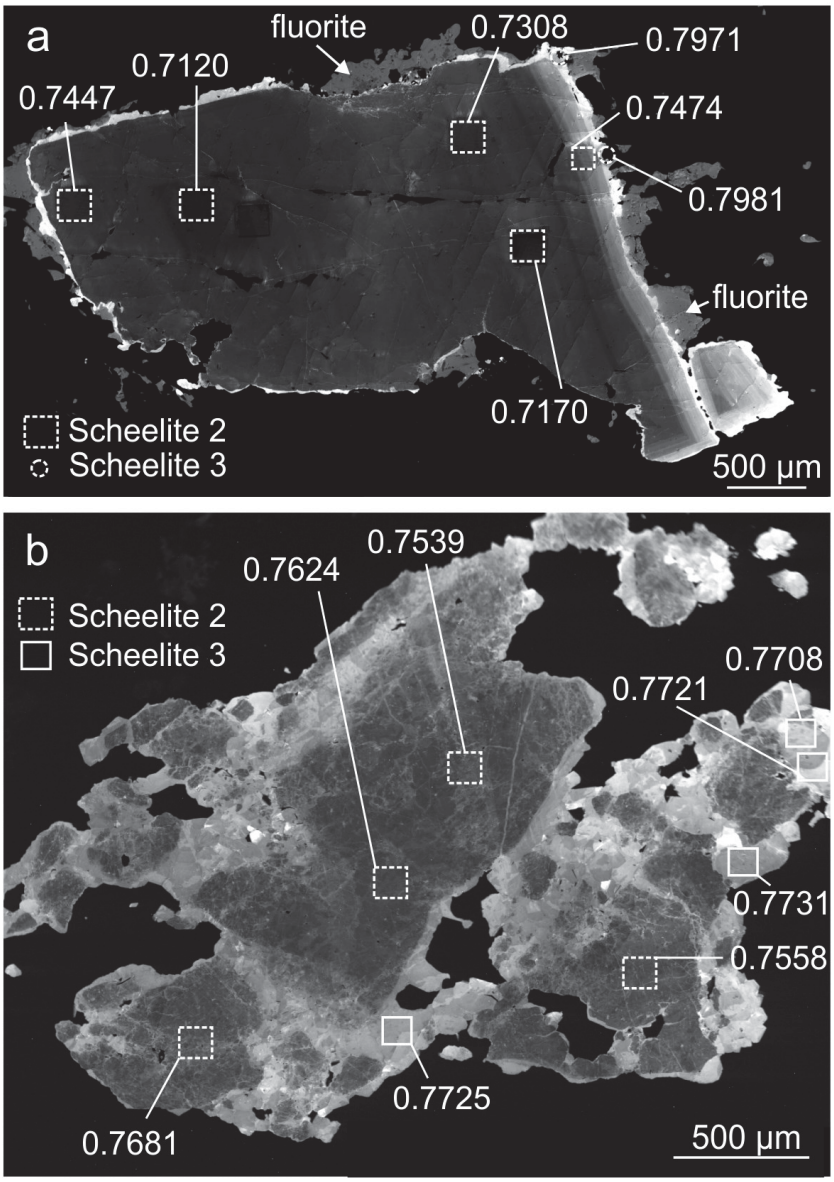

Fig. 5.32 Scheelite 2 crystal overgrown / replaced by Scheelite 3 documenting intra-grain variation of $^{87}Sr/^{86}Sr$ within scheelite. **a)** Cathodoluminescence image of a zoned Scheelite 2 crystal from the quartz-diorite gneiss, sample Gn-1038a, level 1038 m, western ore field. The thin CL-bright outermost rim (white) is Scheelite 3. The outermost medium grey rim is fluorite. Darker square micro-domains are laser ablation pits with a length of 188 µm (inner parts, scheelite 2) and 104 µm (outer rim, Scheelite 3), respectively. **b)** Cathodoluminescence image of CL-dark Scheelite 2 partly recrystallized to CL-bright Scheelite 3 from a scheelite-quartz vein crosscutting the K1-K3 orthogneiss, sample B-K1q-A, level 1164 m, western ore field.

Rb-Sr data of apatite

Data of zoned apatite from the K1-K3 orthogneiss and apatite cores from the scheelite-rich gneiss in the eastern ore field are reported and compared with data from the barren quartz-diorite gneiss (Gn-1262) and two Early Carboniferous Zentralgneise

(Felbertauern augengneiss and Knorrkogel gneiss). Data are summarized in Table 5.4. The complete dataset is in Appendix F.

In general, apatite from the studied samples shows higher Sr concentrations than scheelite, though the Sr contents differ among the samples. Regarding the median Sr concentrations, apatite cores from the K1-K3 orthogneiss (427 ppm Sr) are similar to those from the barren Knorrkogel gneiss (478 ppm Sr). Lower contents were measured in apatite cores from the scheelite-rich gneiss (202 ppm Sr) and the Felbertauern augengneiss (246 ppm Sr). The Sr concentrations in apatite rims of the K1-K3 orthogneiss (Gn-1065b, K1-725, K1-1100, K1-1152) range from 162 to 1296 ppm Sr, with a median value of 679 ppm Sr. Apatite cores from the quartz-diorite gneiss (Gn-1262) have Sr concentrations between 892 and 1274 ppm Sr (median 1173 ppm); the respective rims have similar contents ranging from 944 to 1248 ppm Sr (median 1105 ppm).

Because of the low $^{87}Rb/^{86}Sr$ of all apatite analyses (55 analyses with $^{87}Rb/^{86}Sr$ <0.07510; Table 5.4), a time-correction for calculating the initial $^{87}Sr/^{86}Sr$ ratio is not necessary. The complete data set of apatite $^{87}Sr/^{86}Sr$, arranged according to their hosting lithologies, is also shown in Fig. 5.30. The measured $^{87}Sr/^{86}Sr$ values in apatite cores from the K1-K3 orthogneiss are highly radiogenic and range from 0.72044 to 0.74514 (median $^{87}Sr/^{86}Sr$ = 0.72549). Apatite cores in the scheelite-rich gneiss also show a large variation, with initial $^{87}Sr/^{86}Sr$ ratios ranging from 0.72264 to 0.73845 (median $^{87}Sr/^{86}Sr$ = 0.73377). Apatite cores from the quartz-diorite gneiss (Gn-1262) from the western ore field have lower initial $^{87}Sr/^{86}Sr$ values of 0.70527 to 0.70672 (median $^{87}Sr/^{86}Sr$ = 0.70586), similar to apatite from the Knorrkogel gneiss with values of 0.70649 to 0.70896 (median $^{87}Sr/^{86}Sr$ = 0.70790). The $^{87}Sr/^{86}Sr$ ratios in apatite from the Felbertauern augengneiss scatter and are more radiogenic with ratios ranging between 0.71634 and 0.72954 (median $^{87}Sr/^{86}Sr$ = 0.72192). Compositions of apatite cores in the scheelite-rich gneiss and in the K1-K3 orthogneiss overlap with Scheelite 1 and 2, although isotopic composition of apatite is less variable and commonly lower than in the corresponding scheelite.

Apatite rims from the K1-K3 orthogneiss (sample Gn-1065b, K1-725, K1-1100, K1-1152) have $^{87}Sr/^{86}Sr$ between 0.74535 and 0.77937 (median $^{87}Sr/^{86}Sr$ = 0.77211), those from the quartz-diorite gneiss also show more radiogenic $^{87}Sr/^{86}Sr$ values of 0.70833 to 0.71061 (median $^{87}Sr/^{86}Sr$ = 0.70899). In summary, apatite rims are consistently more radiogenic than the cores.

5.3.2 U-Pb analyses of zircon

Dark-colored K1-K3 orthogneiss (samples Gn-1065b, K1-1100)

A total of 78 analyses were performed (25 zircons each) from samples K1-1100 and Gn-1065b (Fig. 5.33a, b). All analyses are reported in Appendix G. The discordia, for which both CL-bright cores and CL-dark rims (Fig. 5.24a-d) were considered, yields an upper intercept age of 340.1 ± 7.7 Ma for sample K1-1100 (MSWD = 0.54) and 336.1 ± 7.5 Ma (MSWD = 0.98) for sample Gn-1065b. The lower intercept ages are 41 ± 14 Ma and 38.8 ± 6.5 Ma, respectively. Forty-seven analyses of CL-bright cores with magmatic oscillatory zoning (Fig. 5.24a) being nearly concordant (95-106 %) yield concordia ages of 339.6 ± 1.2 Ma (MSWD = 0.96) for sample K1-1100 and 337.3 ± 1.1 Ma (MSWD = 0.80) for sample Gn-1065b. Uranium concentrations are generally low in the CL-bright cores (median 638 and 661 ppm U, respectively), thus the median Th/U ratio is ~0.25. The CL-dark rims have higher U concentrations (median 3514 and 4130 ppm U) and Th/U of 0.41 and 0.18, respectively.

Light-colored K1-K3 orthogneiss (samples K1-725, K1-1152)

Eighteen zircons were considered for U-Pb dating from sample K1-725 and 22 from sample K1-1152 (Fig. 5.33c, d). The discordia yields upper and lower intercept ages of 334.2 ± 9.1 Ma and 28.1 ± 4.4 Ma, respectively for sample K1-725 (MSWD= 1.00). Sample K1-1152 has an upper intercept age of 338.7 ± 8.2 Ma and a lower one of 37.8 ± 4.9 Ma (MSWD = 1.16). A concordia age of 339.4 ± 1.6 Ma (MSWD = 0.59; n = 10) is calculated for near concordant CL-bright cores (95-105 % concordance) of sample K1-725. This is in good agreement with the concordia age of 338.4 ± 1.8 Ma (MSWD = 0.74, n = 15) displayed by oscillatory-zoned CL-bright cores of sample K1-1152 (94-103 % concordance). A trend of increasing median U concentrations and decreasing median Th/U ratios from CL-bright core to CL-dark rim is indicated in both samples.

Aplite gneiss (sample AP-1124)

Fifty-two analyses of 32 zircons from the aplite gneiss sample AP-1124 define a discordia with an upper intercept age of 335.5 ± 9.3 Ma (MSWD = 1.9) and a rather imprecise lower intercept age of 44 ± 13 Ma (Fig. 5.33e). The U-Pb concordia age is 338.0 ± 1.4 Ma for 14 near concordant analyses (94-108 % concordance, MSWD= 0.62), which is within error (2σ) of the U-Pb concordia ages obtained for the K1-K3 orthogneisses. The CL-bright cores are characterized by slightly lower median U concentrations of 555 ppm and Th/U of

0.24, while the CL-dark rims are much higher in uranium (median 5230 ppm U, Th/U = 0.08).

Felbertauern augengneiss (sample SP-25/34)

A discordia was regressed from a total of 31 analyses on 25 zircons (Fig. 5.25a) yielding an upper and lower intercept age of 341.7 ± 9.8 Ma and 72 ± 29 Ma, respectively (MSWD = 0.79; Fig. 5.34a). The lower intercept is geologically meaningless since almost all zircons display nearly concordant U-Pb ages between 300 and 340 Ma. The lower intercept is strongly influenced by the position of only a few discordant zircons. The upper intercept age corresponds well with the concordia age of 18 concordant (96-104 %) zircons giving a U-Pb concordia age of 338.5 ± 1.3 Ma (MSWD = 0.98).

Granatspitz gneiss (sample ST-03/30)

From a total of 25 analyzed zircons (31 spots) 9 zircons revealed U-Pb ages >350 Ma. They are interpreted as inherited zircons (graphically presented in Fig. 5.34b as inset diagram). In the CL images, these zircons are easily identified by very bright CL-intensities and the presence of xenocrystic cores (Fig. 5.25b, zircon 4). The apparent $^{206}Pb/^{238}U$ ages of individual spots in these xenocrysts range between 388 and 1037 Ma. Thirteen analyses of magmatic zircons with oscillatory zoning (Fig. 5.25b, zircon 5 and 6) were considered for age determination, yielding upper and lower intercept ages of 314 ± 18 Ma and 31.7 ± 6.3 Ma, respectively (MSWD = 0.75; Fig. 5.34b). The upper intercept age is conform to the magmatic protolith age of 314 ± 1 Ma reported by Kebede et al. (2005). Calculation of a concordia age was not possible because all analyses show discordance (52-93 % concordance). However, the least discordant individual $^{206}Pb/^{238}U$ ages scatter between 250 and 280 Ma (Fig. 5.34b), corresponding to the mean $^{207}Pb/^{235}U$ age of 271 ± 4 Ma reported by Eichhorn et al. (2000). Thus, the age of the Granatspitz gneiss is still highly arguable.

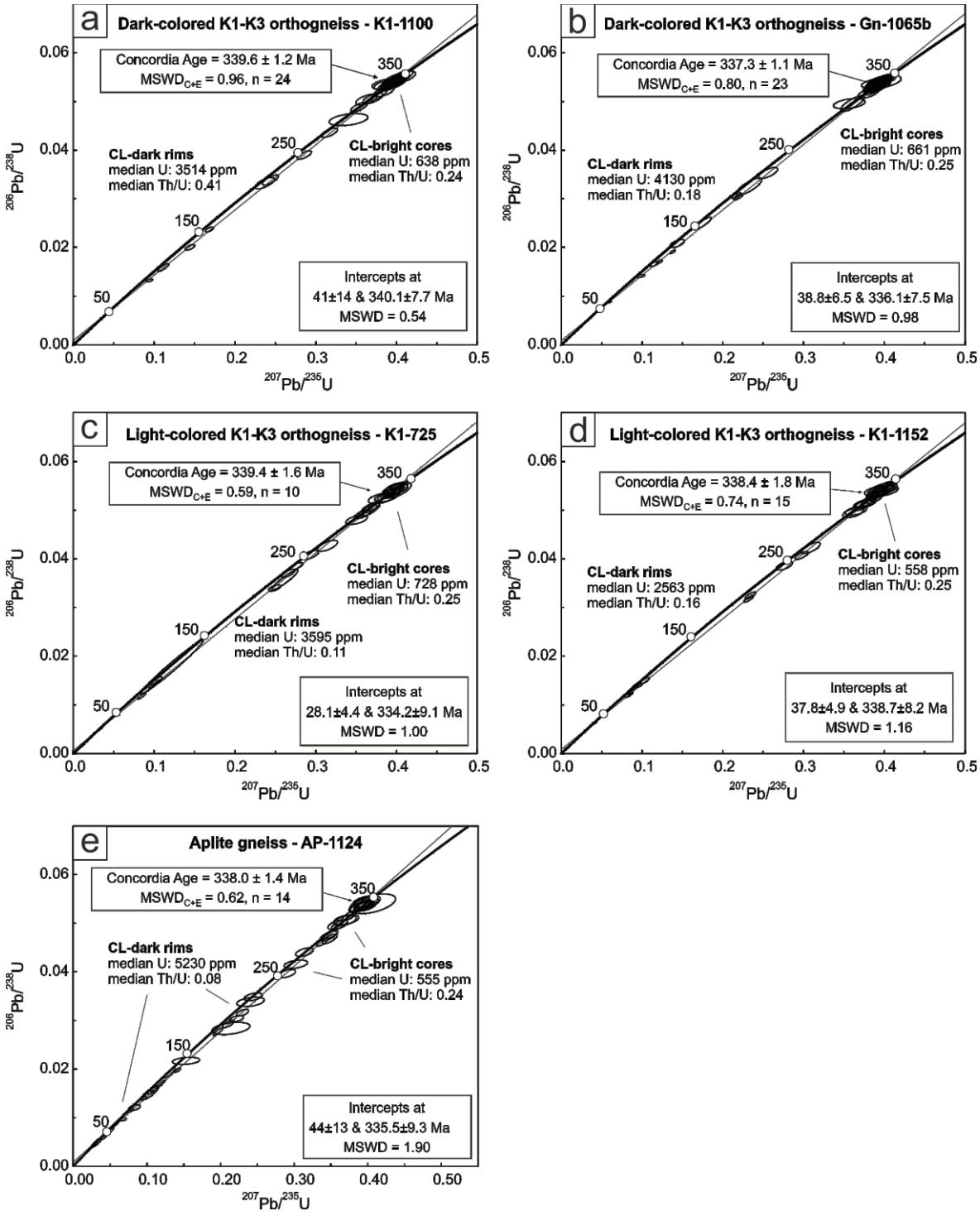

Fig. 5.33 a-e) Results of LA-SF-ICP-MS U-Pb dating of zircon from the dark-colored and light-colored K1-K3 orthogneiss and the aplite gneiss shown in concordia diagrams. Uncertainties for upper and lower intercept ages and concordia ages are 2σ. MSWD$_{C+E}$ represents the mean square of weighted deviations for the aggregated concordance and equivalence of used U-Pb data. Additionally, median U concentrations and Th/U ratios of respective zircon groups are shown. Results are reported in Appendix G.

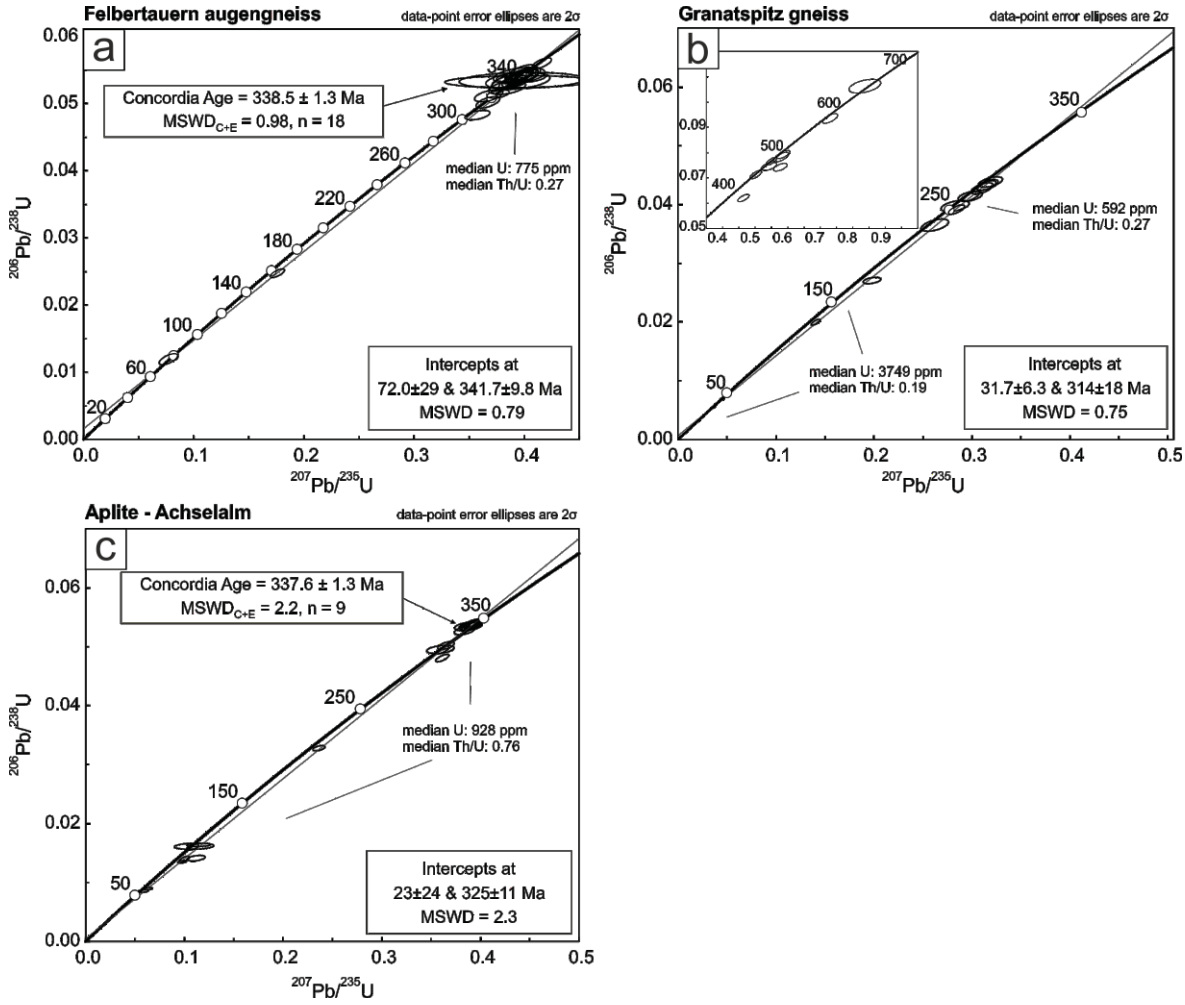

Fig. 5.34 Results of LA-SF-ICP-MS dating of zircons from the Zentralgneise shown in concordia diagrams. For further explanations see Fig. 5.33. **a)** Felbertauern augengneiss. **b)** Granatspitz gneiss; inherited zircons are shown as inset diagram. **c)** Aplite from Achselalm. Results are reported in Appendix G.

Aplite Achselalm (sample AA-49/39)

Twenty-nine analyses of 28 zircons from the aplite dike sample AA-49/39 from Achselalm (Fig. 5.25c) define a discordia with an upper intercept age of 325 ± 11 Ma (MSWD = 2.3) and an imprecise lower intercept age of 23 ± 24 Ma. The U-Pb concordia age of 337.6 ± 1.3 Ma for 8 concordant analyses (101-105 % concordance) is well comparable to the Felbertauern augengneiss and the K1-K3 orthogneiss. The median U concentration of 928 ppm is slightly higher compared to other orthogneisses; the Th/U ratios are significantly higher scattering between 0.07 and 1.46 (median Th/U = 0.76).

5.3.3 Lu-Hf analyses of zircon

K1-K3 orthogneiss and aplite gneiss

Results of Lu-Hf isotope analyses are reported in Appendix H. Lu-Hf analyses of 25 discordant CL-dark rims and 53 concordant CL-bright zircon cores reveal that the apparent $^{176}Hf/^{177}Hf$ ratios of both growth stages are identical within error (overall median $^{176}Hf/^{177}Hf$= 0.282404 ± 0.000022; Fig. 5.35a). The CL-bright cores give apparent εHf_t values between -7.6 and -4.9. The discordant CL-dark domains yield more variable apparent εHf_t values ranging from -11.9 to -6.11, corresponding to re-calculated initial εHf_{338} values from -6.7 to -4.3. The depleted mantle (T_{DM}) ages scatter for both growth zones between 1.25 and 1.40 Ga.

Felbertauern augengneiss, Granatspitz gneiss, Achselalm aplite

Nineteen Lu-Hf analyses of concordant zircon domains from the Felbertauern augengneiss yield apparent $^{176}Hf/^{177}Hf$ ratios similar to those observed in zircons from the K1-K3 orthogneiss (median $^{176}Hf/^{177}Hf$= 0.282396 ± 0.000023; Fig. 5.35b). Additionally, apparent εHf_t values between -6.8 and -5.3 and depleted mantle ages ranging from 1.27 to 1.35 Ga are well comparable to those of K1-K3 orthogneiss zircons.

On the contrary, the 18 Lu-Hf analyses of zircons from the Granatspitz gneiss reveal generally higher apparent $^{176}Hf/^{177}Hf$ ratios (Fig. 5.35b). The zircons used for U-Pb analyses yield elevated apparent $^{176}Hf/^{177}Hf$ ratios between 0.282632 and 0.282727 and scattering apparent εHf_t values ranging from -3.1 to +2.5. The depleted mantle ages range from 764 Ma to 919 Ma suggesting contribution of Neoproterozoic crustal material during partial melting. A second zircon group is characterized by lower apparent $^{176}Hf/^{177}Hf$ (0.282397-0.282623) with εHf_t values ranging between -2.2 and +4.9 and T_{DM} ranging between 0.83 and 1.18 Ga.

Zircons from the Achselalm aplite show similar apparent $^{176}Hf/^{177}Hf$ ratios as those from the Granatspitz gneiss, ranging between 0.28528 and 0.28271 (Fig. 5.35b). Apparent εHf_t values are also highly variable and scatter between -3.65 and +4.72. The depleted mantle ages range from 714 to 991 Ma.

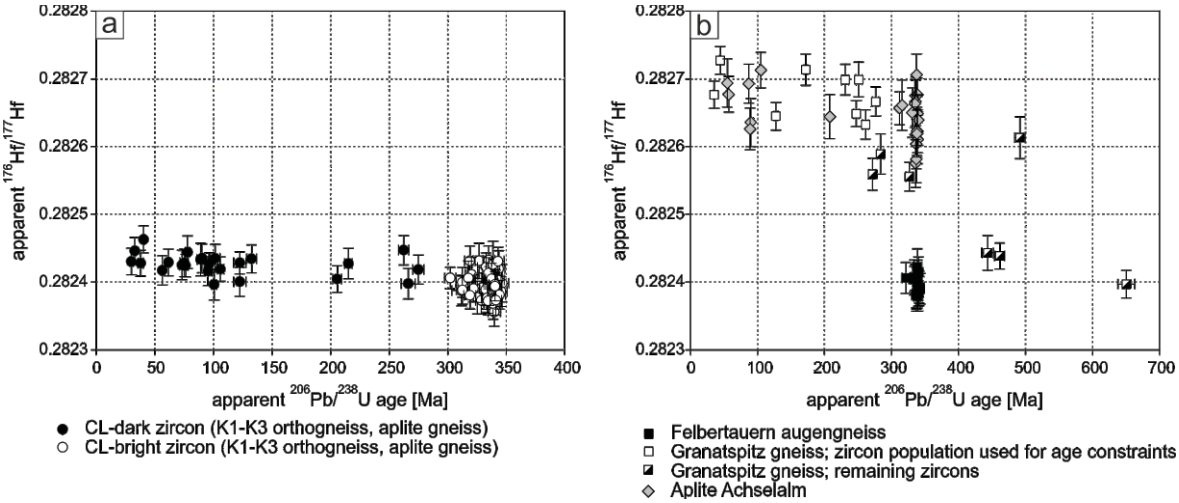

Fig. 5.35 Results of Lu-Hf LA-MC-ICP-MS isotope analyses obtained from different zircon domains and samples. The error bars correspond to 2σ. Analyses are reported in Appendix H. **a)** Apparent $^{176}Hf/^{177}Hf$ of the concordant CL-bright and discordant CL-dark rims from the K1-K3 orthogneiss and the aplite gneiss are identical within analytical uncertainty. **b)** Apparent $^{176}Hf/^{177}Hf$ of zircons from Zentralgneise. Zircons from the Felbertauern augengneiss are indistinguishable from the K1-K3 orthogneiss, whereas those from Granatspitz gneiss and the aplite from Achselalm are clearly different showing higher $^{176}Hf/^{177}Hf$.

5.4 Gamma-ray spectrometry

The results of the gamma-ray spectrometric field measurements in the underground mine on level 1152 (K1-K3 orthogneiss varieties, hornblendite), level 800 (younger K2 orthogneiss) and level 700 (light-colored K1-K3 orthogneiss) are summarized in Table 5.5. For description of the method refer to chapter 3.4.

Lithology	Mine level	K	U	Th	Total
Dark-colored K1-K3 orthogneiss	1152 m	13886	8084	1484	audl
Light-colored K1-K3 orthogneiss	1152 m	9422	7441	981	audl
Light-colored K1-K3 orthogneiss	1152 m	13987	9277	1123	audl
Light-colored K1-K3 orthogneiss	700 m	8005	4138	475	52907
Hornblendite	1152 m	2503	492	66	11284
Younger K2 orthogneiss	800 m	1742	580	115	10272

Tab. 5.5 Total counts/analysis for K, U, Th, and total of gamma-rays measured in various lithologies in the underground mine; audl = above upper detection limit. Measurement time was 300 s.

The results show that the K1-K3 orthogneiss significantly differs from the metabasic host rocks (e.g. hornblendite) and pre-Variscan orthogneisses (e.g. younger K2 orthogneiss) with respect to higher total counts/analysis on each channel. The field measurements on site in the underground mine indicate that the total concentrations of K, U and Th in the K1-K3 orthogneiss exceed the upper detection limit of the used gamma-ray spectrometer. The total counts/analysis for K are similar in both K1-K3 orthogneiss varieties, while the highest value for U was detected in the light-colored variety. The highest amount of Th-counts was detected in the dark-colored variety. The measurements of the light-colored K1-K3 orthogneiss reveal considerable scatter in the counts measured.

The results of gamma-ray spectrometric analyses under laboratory conditions and the concentrations calculated for K, U, Th from these measurements are presented in Table 5.6 and Table 5.7, respectively. In addition, the total counts/analysis of the field measurements of the respective samples are shown for comparison in Table 5.6. Total counts/analysis of the K1-K3 orthogneiss samples 3 and 4 are higher compared to the hornblendite (sample 2) in both the field and the laboratory measurements. Sample 1 of the light-colored K1-K3 orthogneiss yielded relative lower total counts/measurement compared to samples 3 and 4.